1-1-2017

Chalcogenide Nanocrystal Assembly: Controlling Heterogeneity And Modulating Heterointerfaces

Jessica Davis Davis
Wayne State University,

CHALCOGENIDE NANOCRYSTAL ASSEMBLY: CONTROLLING HETEROGENEITY AND MODULATING HETEROINTERFACES

by

JESSICA DAVIS

DISSERTATION

Submitted to the Graduate School

of Wayne State University,

Detroit, Michigan

in partial fulfillment of the requirements

for the degree of

DOCTOR OF PHILOSOPHY

2017

MAJOR: CHEMISTRY

Approved By:

Advisor	Date

DEDICATION

For RH and Fia: Let’s pretend this whole thing never happened, ok?

ACKNOWLEDGEMENTS

First I would like to thank my advisor Prof. Stephanie Brock for her support and professional development throughout my career at Wayne State University, also for making me a cake every year for my birthday. I would like to thank my dissertation committee members, Prof. Stanislav Groysman, Prof. Wen Li and Prof. Mark Cheng, for their valuable advice throughout my PhD work, also for not getting mad at me for sending so many emails without the attachment attached, sorry about that.

None of this thesis research would be possible without collaborations with other scientists and research facilities. The Lumigen Instrument Center has been vital to my research and I would like to thank Bashar Ksebati, for all the assistance and information on NMR spectroscopy. I would like to thank Dr. Zhi Mei for all his work in the microscopy laboratory, without him many of these electron microscope images would look terrible. I would also like to mention Dr. Judy Westrick, Dr. Yuriy Danylyuk, and Dr. Philip Martin for always providing a collaborative research environment, including advice and knowledge of analytical techniques. Many thanks to Dr. Johnna Birbeck and Dr. Olena Danylyuk amazing people to collaborate with in the LIC, for the knowledge and help with ICP-MS.

I want to thank all the staff members in the Department of Chemistry, especially Melissa Barton (who told me not to plagiarize my dedication), Debbie McCreless, Diane Kudla, Bernie Miesik, Diane Klimas, Kellie Lauder, Lisa G. Smith and Jackie Baldyga. I would like to express my gratitude for the staff members of the Science Stores including, Bonnie Cetlinski, Gregory Kish, Elizabeth Ries, and Jason Parizon, especially for their tireless efforts to find one specific chemical that was discontinued, thank you so much that was amazing.

I will be forever grateful to the researchers from Weinberg Physics, LLC: Dr. Irving Weinberg, Dr. Pavel Stepanov and Dr. Mario Urdaneta, for providing me with financial support and allowing me to work on projects involving device fabrication.

TABLE OF CONTENTS

.

LIST OF TABLES

LIST OF FIGURES

LIST OF SCHEMES

CHAPTER 1: INTRODUCTION

In this dissertation research, the goal is to develop methods to facilitate charge transport in heterostructured materials that comprise a minimum of one nanoparticle component. Multicomponent semiconductor materials will be prepared by (1) spin coating nanoparticles on porous silicon (pSi) or (2) self-assembly of compositionally distinct nanoparticles.

Spin-coating of colloidal quantum dot (QD) solutions will be employed to create prototype PbS QD-based radiation detection devices using porous silicon (pSi) as an n-type support as well as a charge transport material (Approach 1). These devices will first be tested as a photodetector to ascertain the possibility of their use in high energy radiation detection. Sol-gel assembly routes will be employed to fabricate metal chalcogenide nanocrystal (NC) gels of different compositions with control of heterogeneity to create donor-acceptor networks potentially applicable to electronic and optoelectronic devices (Approach 2). In order to control the heterogeneity, the factors that underscore sol-gel oxidative assembly will be elucidated. The aggregation and gelation kinetics of metal chalcogenide QDs will be monitored through time-resolved dynamic light scattering (TR-DLS), and nuclear magnetic resonance spectroscopy (NMR) will be used to study surface speciation of metal chalcogenides during aggregation and gelation. Control over heterogeneity in a dual component CdSe-ZnS system, will be achieved through adjustment of the capping ligand, the native crystal structure, and the chalcogenide, thereby changing the relative rates of assembly for each component independently.

1.1. Colloidal Semiconducting Quantum Dot Nanocrystals (NCs)

Nanocrystals have a ratio of surface atoms to total atoms in the particle that is large relative to bulk phases, which affects the physical properties of the material (i.e. melting temperature, phase transition temperature). Colloidal QDs are nanocrystals made of semiconducting materials that have been suspended in solution. There has been considerable and steady interest in these materials for several decades due to the ease of processability in the solution phase, tunability of the light absorption within

the UV, Visible and near-IR range based on the particle size, shape and composition, and the ability to rationally design QD NCs for many applications.[1] These QD nanocrystals are composed of hundreds to thousands of atoms and are usually sub-10 nm in size.[2] Examples of semiconducting quantum dots include those from Group IV (Si and Ge)[3], Group I-VI (Ag_2S, Ag_2Se and Ag_2Te)[4], Group II-V (Cd_3P_2[5] and Cd_3As_2[6]), Group II-VI (ZnS[7], ZnSe[8], ZnTe[9], CdS[10], CdSe[10] and CdTe[10]), Group III-V (GaAs,[11] GaP,[11] InP,[12] InAs,[12] and InSb[13]) and Group IV-VI (PbS,[14] PbSe,[15] PbTe[16]). QDs have been used to develop new light-emitting diodes (LEDs),[17] photodetectors,[18] photovoltaic devices[19] and radiation detectors.[20] The electronic and optical properties that make QDs of interest for such applications are determined by the density of states (DOS) of the materials at the Fermi level. As the size of the semiconductor NCs get close to, or smaller than, the size of the bound electron–hole pair (exciton), the charge carriers become restricted by the boundaries of the material. This is referred to as the quantum size effect and it leads to atomic-like optical behavior in nanocrystals as the bands are quantized. This confinement regime is based on the Bohr exciton radius of the material (Eq. 1.1), where in the strong confinement regime the nanocrystal radius (a_{nc}) is much smaller than the radius of the exciton (a_{exc}).

$$a_b = \varepsilon \frac{m_e}{m^*} a_o \tag{1.1}$$

In Eq. 1.1 ε is the dielectric constant of the material, m^* is the mass of the particle, m_e is the mass of the electron and a_o is the Bohr radius of the hydrogen atom.

The size dependent optical properties of semiconducting nanocrystals can be explained by the position of the Fermi level (E_f) in the band structure of these materials when compared to metals or even insulating materials. In the bulk, semiconductor materials have a large number of atomic orbitals; and their overlap allows them to form energy bands with continuous energy levels. Since the band levels develop concurrently to the bulk material formation, the center of the band develops before the band edge; so in the nanometer size regime, the energy level spacing is very small in the center of the band and gets larger at the edge of the bands (Figure 1.1).[21] The excitons in a QD NC in the strong confinement

regime are squeezed in 3-D which causes the quantum confinement effects (QCE). QCE are predicted by the particle-in-a-box model where the energies of states depend on the length of the box.[22]

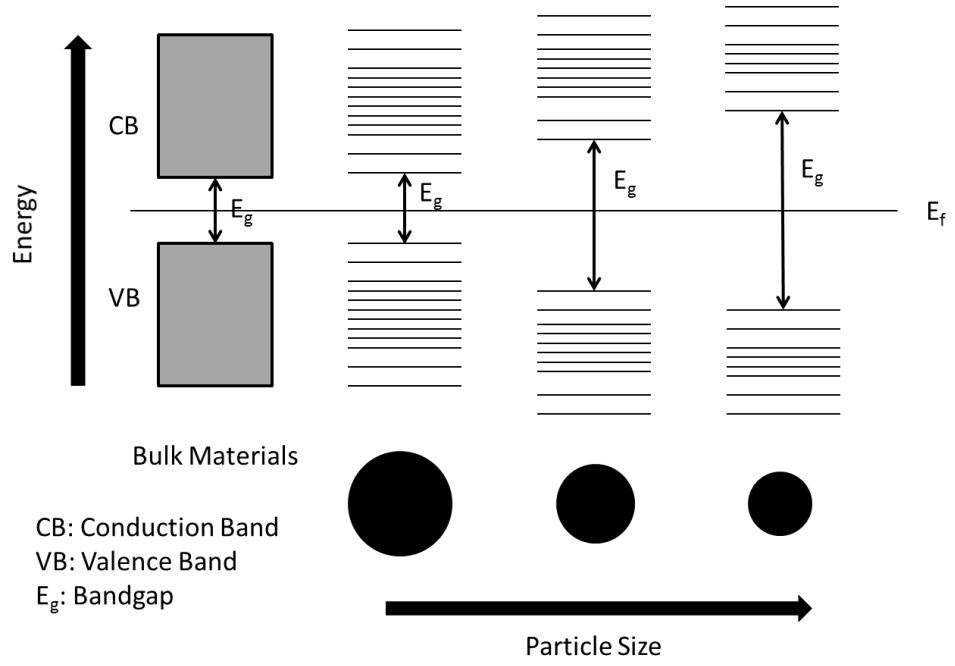

Figure 1.1. Energy-level diagram showing the transition from bulk materials (continuous bands) to quantum dots (discrete states) (adapted from Reimann). [23]

1.2 QD NCs Electronic Structure and Optical Properties

The bandgap (E_g) (Figure 1.1) is the energy difference from the top of the valence band to the bottom of the conduction band. For direct bandgap semiconductors, the absorption of a photon of energy greater than E_g excites an electron from the valence band to the conduction band, which produces a negatively charged electron in the conduction band and a positively charged hole in the valence band. An exciton has an effective reduced mass (μ) as shown in Eq. 1.2, where $m_e^*$the effective is mass of the electron and m_h^* is the effective mass of the hole.

$$\mu = \frac{m_e^* m_h^*}{m_e^* + m_h^*} \tag{1.2}$$

The exciton Bohr radius is defined in Eq. 1.3 where ε_0 is the permittivity of free space and m_e is the mass of the electron.

$$a_{exc} = \frac{4\pi\varepsilon_0\hbar^2}{m_e e^2} \quad (1.3)$$

When the diameter of the spherical QD is below the diameter of the exciton Bohr radius, charge carriers are confined by the boundaries of the material. The quantum size effect results in a quantization of the bulk band as demonstrated in Figure 1.1, unlike in bulk semiconductors, which have a continuous absorption spectrum above the band gap. The reason metal nanoparticles have optical and electrical properties that are analogous to bulk material is due to the valence and conduction band overlap, with the Fermi level in the middle of a band, where the energy levels are closer together.[21]

Since the energy of the electron and hole of the QDs is based on the extent of quantum confinement, related to the size of the QD, there are three regimes of quantum confinement that can be defined based on the QD size: The strong confinement regime ($r<a_e,<a_h<a_{exc}$), the intermediate confinement regime ($a_h<r<a_r<a_{exc}$), and finally the weak confinement regime (a_h, $a_e< r < a_{exc}$), in these comparisons r is the radius of the spherical QD, a_e is the radius of the electron, a_h is the radius of the hole and a_{exc} is the exciton radius.[24]

Direct bandgap semiconducting materials have transitions allowed by the electrical dipole; conversely indirect bandgap materials have electrical dipole forbidden transitions where a photon is required for electrical transition (Figure 1.2).

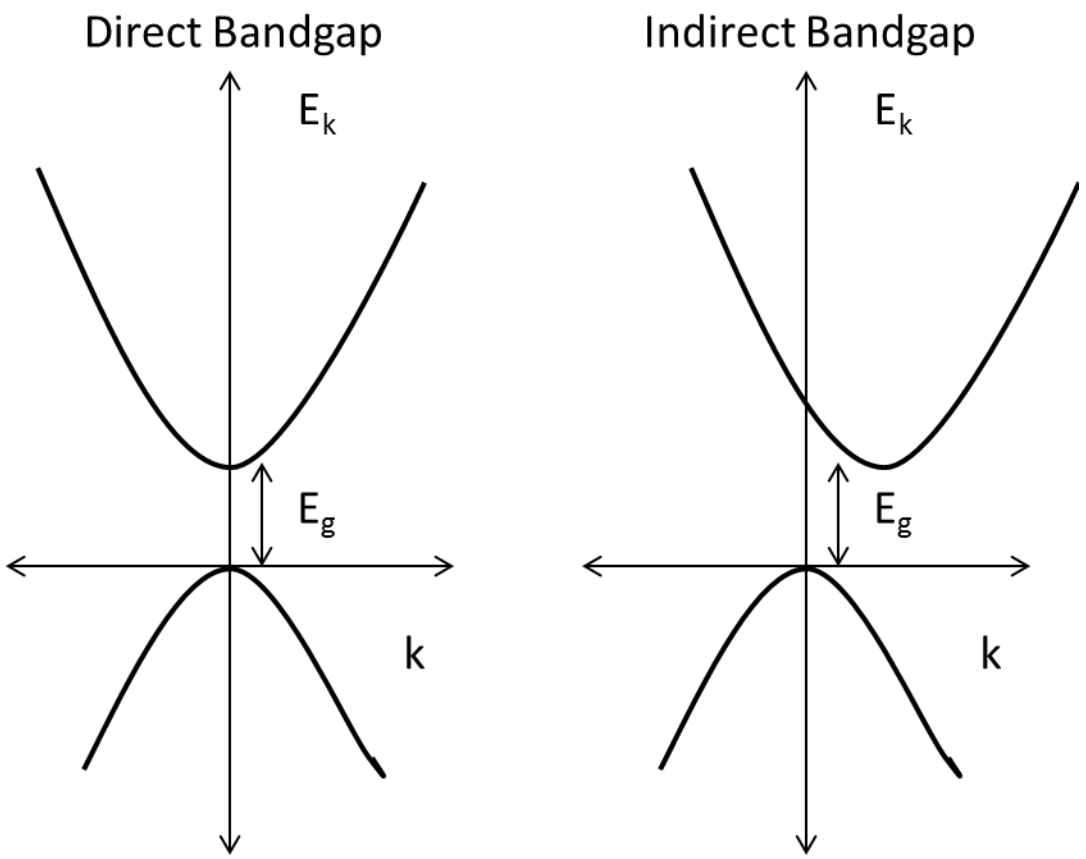

Figure 1.2. Simple two band model for direct and indirect bandgap semiconducting material (adapted from Zhang).[24]

The single-particle wave functions for the electrons and holes are linear combinations of the atomic orbitals (LCAOs) in the unit cell. When the dimensions of the cells enable the LCAOs to be in phase, the wave vector (Eq. 1.4.) is zero, when the LCAOs perfectly out of phase the wave vector is π/a, the highest value.

$$k = \frac{2\pi}{\lambda} \tag{1.4}$$

Thus, in a simple one-dimensional model, the dependence of E on *k* is shown in Eq. 1.5 where α is the energy of the linear combination of atomic orbitals in the unit cell and 2β is the width of the band which is inversely proportional to the effective mass.

$$E = \alpha + 2\beta \cos(ka) \tag{1.5}$$

The quantum size effect can be obtained using the particle-in-a-box model with a series of approximations. The band gap of the QD can be estimated using the effective mass approximation, in which conduction and valence bands are approximated as single parabolic conduction and valence bands (Figure 1.2), and the effective band gap of quantum dots can be approximated as in Eq 1.6, where r is the QD radius.[24]

$$E_g(QD) = E_g + \frac{\hbar^2\pi^2}{2\mu r^2} \tag{1.6}$$

In the strong confinement regime, an additional term has to be used to account for the Coulombic interaction between electrons and holes (Eq. 1.7).

$$E_g(QD) = E_g + \frac{\hbar^2\pi^2}{2\mu r^2} - \frac{1.8e^2}{\varepsilon r} \tag{1.7}$$

Another important factor affecting the electronic and structural properties of QD NCs is the shape effect. The unit of confinement decreases as the number of confined dimensions decreases (three (QD) > two (quantum wires) > one (quantum disks and wells)). Figure 1.3 illustrates the density of electronic states in one band of a 2-dimensional, 1-dimensional and 0-dimensional semiconductor.[21]

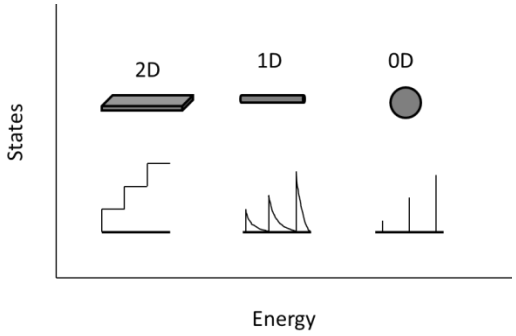

Figure 1.3. Illustration of the density of states for semiconductor materials confined in 2D, 1D and 0D (adapted from Alivisatos).[21]

The density of states is the number of states per unit energy, which is determined by the crystal structure and electronic properties of the material, for example the density of states of an electron N(E) in a parabolic conduction band (Figure 1.3) is given in Eq. 1.8.[25]

$$N(E) = \frac{1}{2\pi^2\hbar^3}(2m_e^*)^{3/2}\left(E - E_g\right)^{1/2} \quad (1.8)$$

Alternatively, the density of states for a hole in the parabolic valence band is Eq. 1.9.

$$N(E) = \frac{1}{2\pi^2\hbar^3}(2m_h^*)^{3/2}E^{1/2} \quad (1.9)$$

A fermion is an elementary particle (an electron in this case), which follows the Fermi-Dirac distribution function (Eq. 1.10) of the electron occupancy in the electronic states.

$$f(E) = \frac{1}{\exp\frac{(E-E_F)}{k_BT}+1} \quad (1.10)$$

In which the E_f value is the Fermi energy (Fermi level), in this case, k_B is the Boltzmann's constant, and T is the absolute temperature. Conversely, the density of holes is based on the density of states, and the probability that the state is empty (Eq. 1.11).

$$1 - f(E) = \frac{1}{\exp\frac{(E_F-E)}{kT}+1} \quad (1.11)$$

The energy level spacing and density of states for nanoscale semiconducting materials varies as a function of the size, based on the quantum confinement effect. As the particle size decreases, the spacing between the energy levels increases quadratically, making the equation for the effective bandgap of specifically a spherical particle with radius r, $(E_{g,eff}(R))$, Eq. 1.12. Since the bandgap is inversely proportional to r^2, the bandgap will increase as the radius of the particle decreases.

$$E_{g,eff}(R) = E_{g,bulk} + \frac{\hbar^2\pi^2}{2r^2}\left(\frac{1}{m_e^*} + \frac{1}{m_h^*}\right) - \frac{1.8e^2}{\varepsilon r} \quad (1.12)$$

The crystal structure or lattice structure, i.e., the long range order of the material, also has an effect on the electronic and optical properties of semiconducting NCs. Phonons are collective excitations that occur in a periodic arrangement of atoms or molecules. Solid lattice structures have two types of phonons; acoustic phonons, which are high frequency vibrations of atoms in the lattice out of their equilibrium positions; and acoustic phonons which are lower frequency vibrations of atoms in phase.

Light absorption is defined as a relative rate of decrease in light intensity along the path of propagation (Eq. 1.13).

$$\alpha(h\upsilon) = \frac{1}{h\upsilon}\frac{dI(h\upsilon)}{dx} \tag{1.13}$$

In Eq. 1.13 the intensity is $I(h\upsilon)$, and the path of propagation is defined as x. For the direct bandgap transitions based on electrical dipole allowed transitions, $\alpha_d(h\upsilon)$, in Eq. 1.14 for direct conversion bandgap materials, the constant A^* is based on the index of refraction and effective mass of the electron and hole.[25]

$$\alpha_d(h\upsilon) = A^*(h\upsilon - E_g)^{1/2} \tag{1.14}$$

For indirect bandgap materials with electric dipole forbidden transitions, where phonon energy is required (E_p), the electron absorption coefficient is shown in Eq. 1.15.[25]

$$\alpha_i(h\upsilon) = \frac{A^*(h\upsilon - E_g + E_p)^2}{exp\frac{E_p}{kT} - 1} \tag{1.15}$$

Eq. 1.15 shows that the absorption coefficient depends on the numerous transitions in the material, so the absorption spectrum is a means used to determine the bandgap energy and also the different types of transitions in the QDs.

1.3 Quantum Dot Synthesis and Passivating Ligands

There are two basic synthetic regimes for nanoparticle synthesis: chemical synthesis and physical synthesis. In the interest of brevity in this dissertation, only chemical synthetic methods, which are relevant to the work performed, will be covered in this thesis. In the category of chemical synthetic techniques there are solution based processes and gas-phase synthetic methods. Solution-based colloidal QD synthesis is commonly used because it allows the QD size to be tuned; this is because of the two main critical steps in solution based synthesis: 1) the initial nucleation step, and 2) the subsequent growth of the nanocrystals.[26] Good quality NCs with a narrow size distribution are usually synthesized by hot-injection techniques in which precursors are rapidly injected into a solution high temperature in the

presence of organic surfactants and stabilizing agents. At high temperature the inorganic salt precursors, (e.g. cadmium oxide, cadmium acetate, lead oxide, cadmium chloride, zinc chloride) chemically transform into reactive atomic or molecular species (monomers) leading to nucleation and growth of NCs.[27-28] The rapid addition of the reagents will increase the precursor concentration above a known nucleation threshold, which starts the nucleation of the nanocrystals. The synthesis of a monodisperse solution of colloidal QDs, has been shown to start with discrete nucleation, which is then followed by a controlled growth cycle using existing nuclei. The la Mer model for the nucleation and growth is shown in Figure 1.4, where the initial concentration rises above the saturation concentration which is followed by short bursts of nucleation and the synthesis of a large number of nuclei in short time intervals. These aggregates grow rapidly and lower the concentration below the nucleation level, which allows for separate nucleation and growth phases.[29-30]

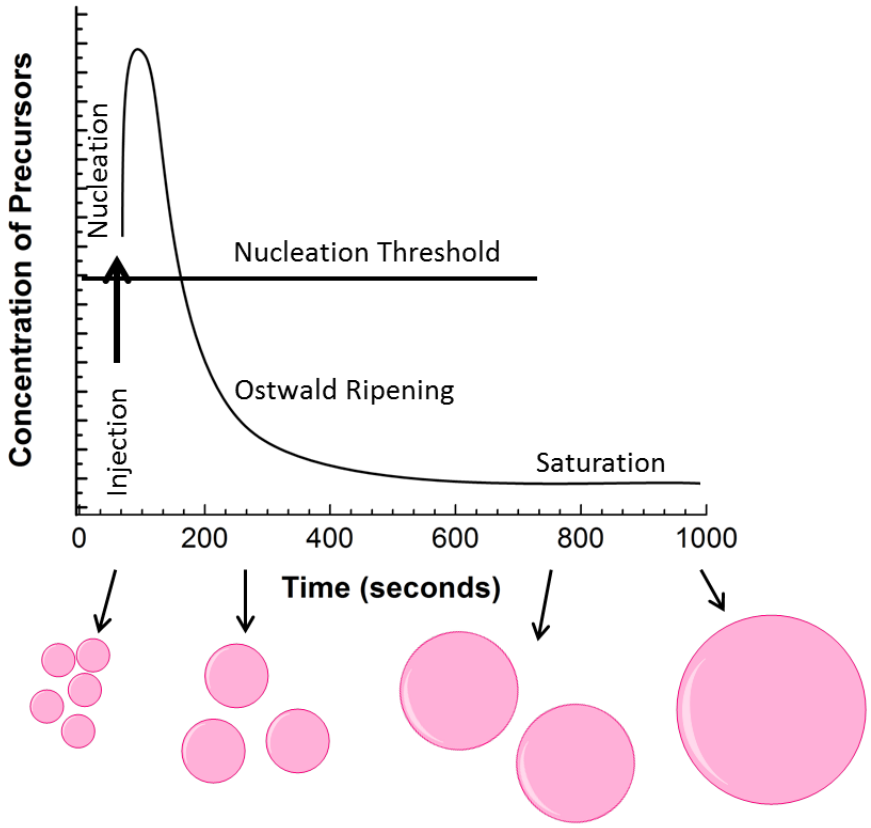

Figure 1.4. Scheme of the La Mer model for the stages of nucleation and growth for monodisperse semiconducting colloidal nanoparticles (adapted from Klimov).[2]

Following this discrete nucleation event, there is rapid growth that is then followed by saturation and the slower Ostwald ripening. Ostwald ripening is due to the higher energy surfaces in the smaller particles, which promote their dissolution into solution. Once dissolved they can add and grow on the larger particles, thus promoting a more polydisperse particle size distribution.[26] Particle size control can be achieved through several routes, including longer reaction times that promote larger particle sizes; higher synthesis temperatures that facilitate Ostwald ripening and produce larger, more polydisperse particles; and higher concentration of monomers that form fewer but larger nuclei and results in larger nanoparticle sizes.[31] Most of these high temperature synthesis techniques involve the use of stabilizing agents to

promote the solvation of one precursor. Thus another synthetic route for increasing particle size is to have a low ratio of stabilizer-to-precursor in solution.[32]

The narrow growth regime that occurs before Ostwald ripening has a significant impact on the particle size distribution. The early stages of the NC growth are described by a "focusing of size distribution" model.[33] The growth process of QD NCs occur in two different modes, 'focusing' and 'defocusing', based on the concentration of the monomer present prior to Ostwald ripening. At higher concentrations of the monomers, the critical size of the NCs will remain small so that all the particles in solution will grow. In this condition, the smaller particles grow faster than the larger ones, which allows for the size distribution to be focused to a nearly monodisperse solution. If the monomer concentration is below the critical threshold, the smaller NCs are solvated and the larger ones grow, thus the size distribution broadens.[28, 34]

Another preparation method that can be performed at moderate temperatures is the inverse-micelle synthetic method. This low-temperature synthetic route suffers from relatively poor size distributions and the QD products often have poor photoluminescence (PL) emission, or trap state emission due to poor crystallinity and surface defects. These lower temperature (sometimes room temperature) synthetic methods have typically been limited in their applicability to more ionic materials. The most commonly used method for inverse micelle synthesis involves the preparation of two separate microemulsions using a surfactant and water-in-oil solution where the separate precursors are in small water droplets (e. g. $CdCl_2$ and Na_2S). The two separate precursor solutions are combined and nucleation occurs on the micelle edges as the water inside is supersaturated with the co-reactants.[35] The growth phase is continued around this nucleation point, with the influx of more co-reactants from intermicellar exchange (Figure 1.5).[36]

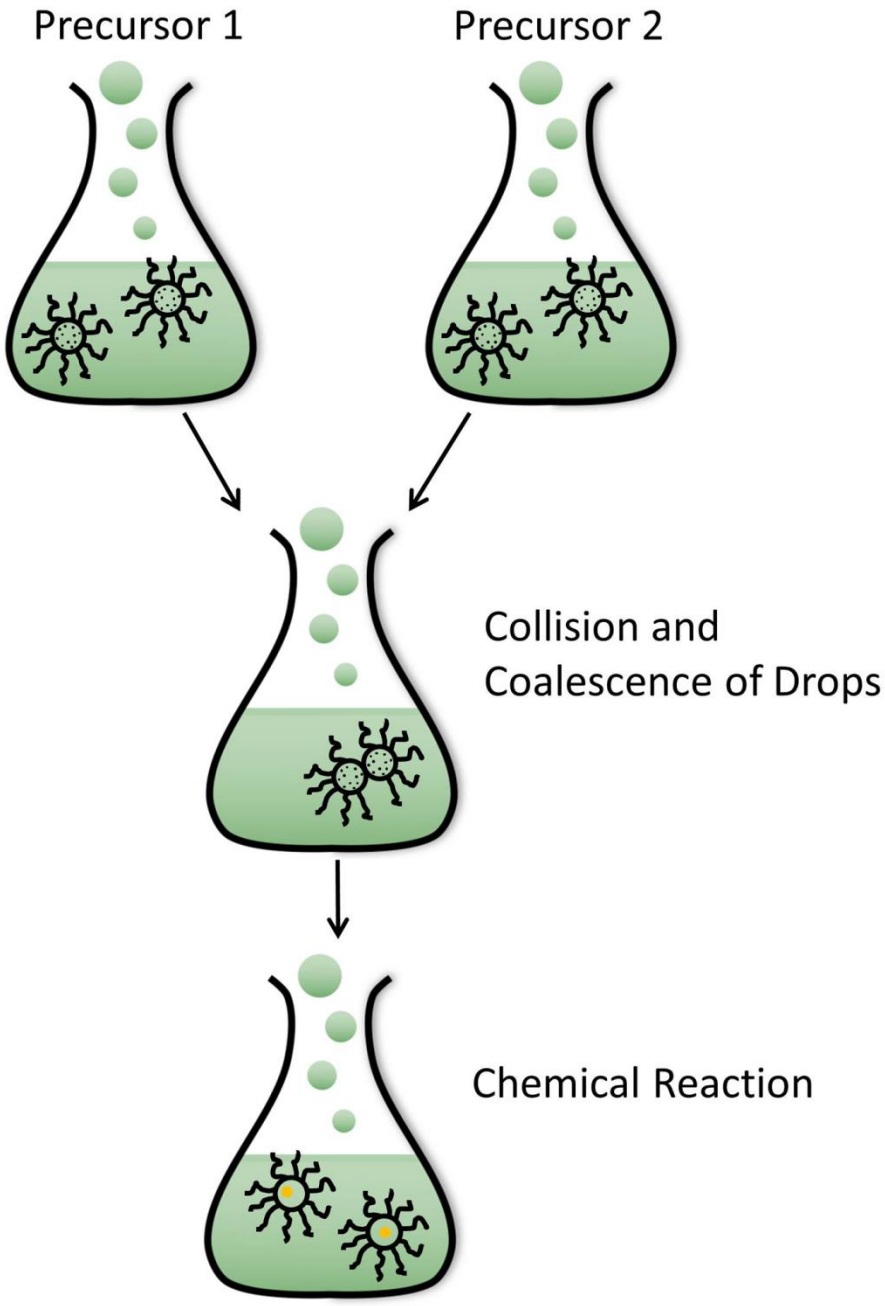

Figure 1.5. Possible mechanism for the formation of nanoparticles by the inverse micelle approach (adapted from Capek).[36]

For inverse micelle synthesis, the final particle size is controlled by the ratio of water to surfactant Eq. 1.16, with a higher ratio of water leading to larger particle sizes in the resultant nanoparticles.

$$Particle\ Size = \frac{[Water]}{[Surfactant]} \tag{1.16}$$

1.4 Colloidal Aggregation and Sol-gel Synthesis

A colloidal solution, or sol, is considered a suspension of materials in the size regime 1-1000 nm, dispersed in a solvent, that are very negligibly affected by the gravitational forces. The interactions between the particles is subjected to different types of short range forces, including van der Waals attractions and charges on the surface of the material. The materials display Brownian motion, which is the random motion of the particles in solution from their collision with other particles and molecules in solution. When a sol aggregates it forms fractal structures. If the mass (m) of the fractal increases with its radius (r) according to Eq. 1.17 it is considered a mass fractal. [37]

$$m \propto r^{d_f} \tag{1.17}$$

In Eq. 1.17, d_f is the mass fractal dimension for the object, which is different than for a Euclidian object where $m \propto r^3$; because $d_f < 3$ for a fractal, the density decreases as the radius increases.

A gel forms when particles assemble to form a macroscopic 3D network that extends throughout the volume of the medium. These linkages between primary particles, enclosing the solvent, make a gel a continuous solid phase enclosing a liquid phase on all sides of the sample. Gels can be formed from a sol when some form of attractive dispersion force acts on the particulates to make them stick together and form a 3D network. The formation of a gel begins with the fractal aggregates, which grow until they intrude into each other, then form a linkage. At the gel point (when the last bond is formed) bonds are formed randomly between clusters that cannot move, finally a single cluster extends through the entire sol.[37] If the dimension of the gel is more than several millimeters the structure is termed a monolith. If the liquid phase of the gel is removed by destructive techniques such as evaporation, where the capillary forces deform the network structure, the resultant material is called a xerogel, as a large degree of porosity is removed. If instead the wet gel is dried using supercritical conditions (supercritical drying), where the boundary between liquid and gas is removed, the gel can be dried with little shrinkage, because

there are no capillary forces to destroy the porosity; the final resultant product is known as an aerogel (Figure 1.6).

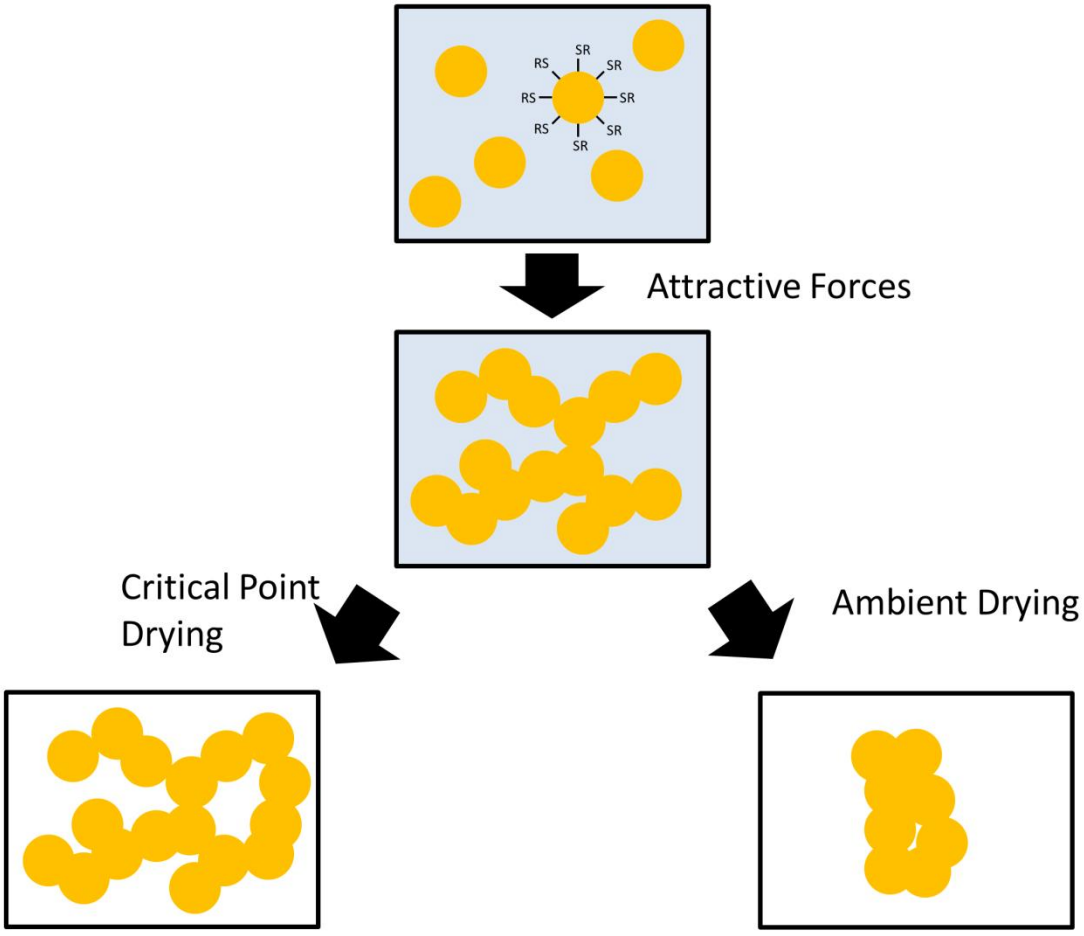

Figure 1.6. Schematic representation of the sol-gel synthesis followed by drying conditions (i.e. critical point or ambient drying) to form either aerogel or xerogel respectively (reproduced from Brock). [38]

In oxide sol-gel assembly, alkoxide precursors in acidic or basic aqueous or alcohol solution undergo a series of hydrolysis and condensation reactions to form a colloidal sol solution. This is followed by the formation of a network of nanoparticles via controlled aggregation. Metal alkoxides hydrolyze following Scheme 1.1.[37]

$$M(OR)_x + mH_2O \longrightarrow M(OR)_{x-m}(OH)_m + mROH \qquad \text{Scheme 1.1}$$

For m = x total hydrolysis occurs, followed by either water condensation (Scheme 1.2) or alcohol condensation (Scheme 1.3) reactions.

$$2M(OR)_{x-m}(OH)_m \longrightarrow (OH)_{m-1}(OR)_{x-m}\text{-M-O-M}(OR)_{x-m}(OH)_{m-1} + H_2O \quad \text{Scheme 1.2}$$

$$2M(OR)_{x-m}(OH)_m \longrightarrow (OH)_{m-1}(OR)_{x-m}\text{-M-O-M}(OR)_{x-m}(OH)_{x-m-1} + ROH \quad \text{Scheme 1.3}$$

It is known that in colloidal aggregation there are two limiting regimes for both the kinetics of assembly of the aggregates and the resultant fractal morphology of the aggregates. This is determined by the sticking probability R between NCs, clusters and aggregates. If R is equal to unity, diffusion limited cluster-cluster aggregation (DLCA) is expected. Values of R below unity will lead to the reaction-limited cluster-cluster (RLCA) aggregation regime.[37] The solution to the Smoluchowski equation shows that in the DLCA regime, the growth of the average radius of gyration (R_g) or the distribution of the material components around an axis for a cluster, obeys a power law behavior as a function of time (Eq. 1.18).[39-46]

$$R_g\,(t) = R_g(0)\left[1 + \alpha\frac{t}{\tau}\right]^{z/d_f} \tag{1.18}$$

In Eq. 1.18, z is a dynamic exponent d_f is the fractal dimension and R is the sticking probability in the collision between clusters and aggregates. The time constant that determines the aggregation reaction, τ, is the reciprocal Smoluchowski rate, which is inversely proportional to the particle concentration, N_0, in Eq. 1.19.

$$\tau = \frac{3\eta}{4k_BT}\frac{1}{N_0} \tag{1.19}$$

In this case, the viscosity, η, of the solvent is important and k_BT is the thermal energy term. Alternatively the RLCA growth regime for the average radius of gyration is an exponential function, Eq. 1.20.

$$R_g(t) = R_g(0)exp\left(2\alpha\frac{t}{\tau}\right) \tag{1.20}$$

1.5 Semiconductor Assemblies

As more elaborate solution-phase synthetic strategies to produce semiconducting monodisperse NCs are developed, it opens the door to a wide variety of applications for these unique materials. As

mentioned previously, the novel size and shape dependent electrical and optical properties of semiconducting NCs make them potentially advantageous in many optoelectronic devices. A current problem with the use of semiconductor NCs for solid state optoelectronics is that the synthetic methods produce NCs with long-chain insulating ligands for surface passivation and solution-phase processing. Integrating NCs together require assembly processes that either exploit the long-chain ligands or remove/replace them.

One of the simplest assembly routes for colloidal QDs is to concentrate to dryness. QDs passivated with a long-chain ligand, which allows them to be stable to aggregation in solution, can be deposited through spin-coating or other printing techniques onto surfaces.[47] With the evaporation of the solvent, the QDs form a thin film. One drawback of this method is the lack of control over the particle ordering. Achieving order depends on the QD size and shape, along with the evaporation rate of the solvent, and after deposition the QDs still remain separated by the long-chain insulating ligands. Similar assembly methods include layer-by-layer deposition and Langmuir-Blodget deposition techniques.[48]

For these common QD solids, the individual QDs are separated by the long-chain insulating ligands. For charge transport between these QDs, the carriers must transport through these interparticle distances with a tunneling rate (Γ) shown in Eq. 1.21.[49]

$$\Gamma \approx exp\left[-(2m^{*}\Delta E/\hbar)^{1/2}\Delta x\right] \qquad \text{(Eq. 1.21)}$$

Where ΔE and Δx are the height and width of the tunneling barrier as determined by the capping ligands. This tunneling rate increases by decreasing the interparticle QD distance. It is important to note that charge transport in these QD solids will also depend on the size, polydispersity, and organization of the QDs in the material.[50]

One method developed by Brock et al. to overcome this separation in QD solids is to combine them into non-ordered three dimensional architectures, i.e. xerogels and aerogels, based on the sol-gel synthetic method, as described in Section 1.4.[38] Gacoin et al. pioneered the original sol-gel process for

the assembly of discrete CdS NCs into wet gels.[51] Brock et al. have extended this technique to assemble several types of metal chalcogenide NCs such as CdSe,[52-53] CdTe,[54] ZnS,[38] PbS,[38] PbSe,[55] PbTe,[56] and Bi_2Te_3.[57] As shown in Figure 1.7, the controlled oxidation of a thiolate-capped metal chalcogenide NC sol, achieved by the use of a non-oxygen transferring oxidant (tetranitromethane), leads to aggregation of NCs. This is considered to occur as a three-step process: 1) surface deprotection through the oxidative removal of the surface thiolate ligands; 2) the removal of some of the surface metal ions into solution; 3) oxidative formation of di- and polychalcogenide linkages ($2Q^{2-} \rightarrow Q_2^{2-} + 2e^-$).[58] These inter-NC networks, formed through this sol-gel synthesis, would predictably provide better electronic communication in these NC assemblies while maintaining the important quantum confinement effects of the original QDs.

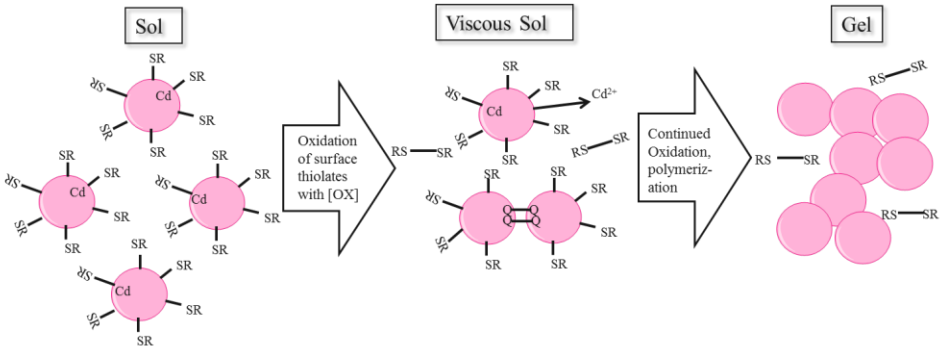

Figure 1.7. Proposed gelation mechanism for cadmium chalcogenide NCs (adapted from Pala et. Al.).[58]

1.6 Heterogeneous Semiconductor QDs

An important development in the field of colloidal nanocrystal synthesis, was the development of effective synthetic routes using strongly coordinating ligands to stabilize QDs in solution.[10] This is well known for II-VI QDs, but has also been used to synthesize IV-VI, III-V, and Group IV QDs. The next logical step to create complex functional materials is to fabricate high-quality heterostructured NCs. Much research has been focused on techniques for NC shape control, but some of these have yielded new levers for controlling the electronic and optical properties, as well as new methods to control their assembly into NC structures.[33, 59]

Initial studies focused on the synthesis of heterostructured QDs, allowing further tailoring of bandgaps, stability, photophysical properties and crystal structures. The early and most commonly studied heterostructured QDs include gradient alloys (Figure 1.8a) such as, $Zn_xCd_{1-x}Se$,[60] $CdS_{1-x}Se_x$ [61] and $InGaP_2$ QDs. [62] These heterostructured QDs can have more complex properties including improvement in photoluminescence (tunable wavelengths) and solution phase stability; conversely the synthetic techniques involved can lead to compositional fluctuations throughout a single particle.[60]

Another type of heterostructured QD type is the core shell structure (Figure 1.8b), starting with a NC core, followed by introduction of the precursors for the shell material, it is important that nucleation of the shell happens separately from the core.[63-65]

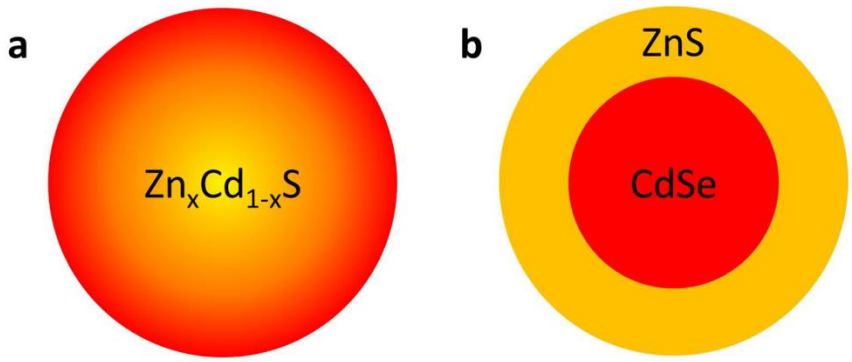

Figure 1.8. Heterogeneous quantum dots a) ternary phase materials and b) core-shell materials.

The respective carrier spatial localization is heavily influenced by the relative positions of the valence and conduction bands of the heterostructured material making up the core@shell QD, these positions are used to categorize the main types of heterojunctions. The Type-I core@shell heterostructures (Figure 1.9a) has two semiconductor materials with bandgaps of different size; the most common example is CdSe@ZnS QDs. One of the component materials has a higher lying valence band and lower lying conduction band than the other; this forces the excited carriers to localize in the narrower bandgap

material. Opposite to most type-I heterostructures, type-II heterostructures tend toward components with bandgaps that are moderately wide (>1.3 eV). These Type-II materials have a staggered band-alignment in which the conduction and valence bands of one material are higher-lying than those of the other component (Figure 1.9b). This band alignment means that excited carriers or the electron will be localized in the material (either core or shell) with the lower-lying conduction band; an example of this is CdS@ZnSe. The drawbacks to these type of structures include mismatched core-shell structures which causes interface strain.[60]

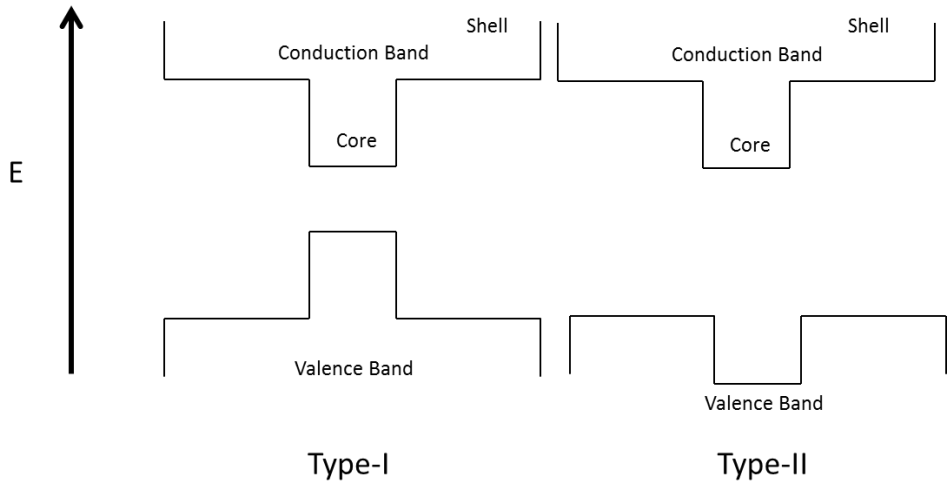

Figure 1.9. Schematic of a) Type-I QDs where the band alignment causes both the electron and hole to reside in either the core or shell and (b) Type-II QDs the band alignment means the electron and hole separate between the core and shell in the QD (adapted from Klimov).[66]

Other types of heterostructured nanocrystals include the combination of two types of nanostructures, such as Type II-VI NCs combined with noble metal nanoparticles grown or deposited on their surface. These hybrid structures are used mainly as photocatalysts, based on the light-harvesting capabilities of the semiconducting NC portion. These semiconducting NCs can be programmed to have long singlet exciton lifetimes, then the free carriers that result from the exciton dissociation are used to catalyze the generation of either H_2 ($2H^+ \rightarrow H_2$) with a reduction catalyst or ($2OH^- \rightarrow O_2$) with an oxidation catalyst, as shown in Figure 1.10.[67-71]

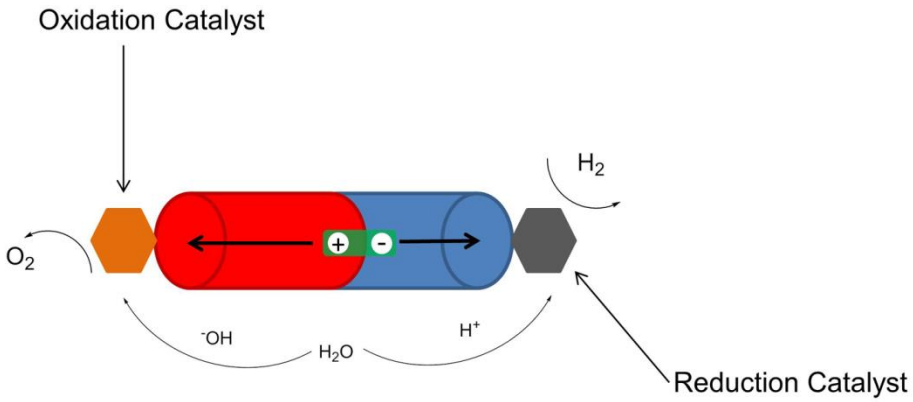

Figure 1.10. Schematic of a metal-semiconductor heteromaterial, showing both reductive and oxidative catalysis (adapted from Zamkov).[72]

1.7 Thesis Statements

The oxidative sol-gel synthesis method described previously in this dissertation work (Section 1.4) is a well-known and robust method for linking semiconductor NCs into a 2- or 3-D architecture (i.e., thin films, gels, xerogels, and aerogels) while conserving the properties of the individual NC QDs.[38, 51, 73] This makes the sol-gel synthesis a unique method for introducing QDs into electronic and optoelectronic devices, such as field-effect transistors (FETs),[74-75] photodetectors,[76-77] light emitting diodes (LEDs),[78-79] photovoltaics[80-81] and radiation detectors.[20, 82] This sol-gel synthesis technique has many built-in synthetic levers that could facilitate the formation of multicomponent materials, with possible synergistic affects. The main focus of this dissertation work is: 1) incorporating these MQ QDs into heterogeneous architectures 2) developing and studying further synthetic levers for control of the kinetics of aggregation of MQ (M=Cd, Zn and Pb, Q=S, Se and Te).

The dissertation research has three specific goals in order to achieve these objectives.

I. Improve interfacial charge transport of a QD/porous Si heterostructured device for radiation detection.

II. Develop synthetic levers for control over kinetics of aggregation in oxidative gelation of MQ (M= Cd, Q= S, Se and Te) QDs.

III. Synthesize multicomponent MQ materials of CdSe/ZnS with controlled phase segregation.

Aim I: Improve interfacial charge transport of a QD/porous Si heterostructured device for radiation detection (presented in Chapter 3)

A combination of porous or micro-machined silicon infused with semiconducting lead sulfide (PbS) quantum dots (QDs) of high electron density has the potential to be used in radiation detection devices due to the high stopping power of PbS QDs combined with a thick Si support. Previous work has shown these heterostructured devices exhibit some charge transport, but are expected to benefit from short-chain passivating thiolate capping ligands and anion passivation.[20, 82] Modification of the surface of the PbS QDs through anion passivation at the interface of the heterostructure where the QDs interact with the Si, is expected to improve the charge transport properties of these devices. Accordingly, in this dissertation research, the combination of PbS QDs and pSi supports were studied as photodetectors, to study the charge transport properties of the device, to determine if they could potentially be used as future generation radiation detection devices. The resultant devices and components were characterized using transmission electron microscopy (TEM), and scanning electron microscopy (SEM), and the I-V response curves were measured to determine if these multicomponent architectures could be used as direct conversion detectors for radiation detection devices.

Aim II: Develop synthetic levers for control over kinetics of aggregation in oxidative gelation of MQ (M= Cd, Q= S, Se and Te) QDs (presented in Chapter 4)

This dissertation work is motivated by the possible synergistic properties that can be achieved in complex materials comprising multicomponent metal chalcogenide nanostructures. There is considerable potential for these materials in optoelectronic and photovoltaic devices that require two types of materials with disparate properties, where a rational method for solution phase deposition would allow for easily tailoring of device components. We have established methods for single component metal chalcogenide (MQ) particle gels and now seek to develop a practical method for co-gelation of different

component particles with complimentary functionalities. This dissertation research seeks to monitor the kinetics of aggregation of single component systems, using time resolved dynamic light scattering (TR-DLS) and nuclear magnetic resonance spectroscopy (NMR) to study the role of the native crystal structure (cubic and hexagonal) of the constituent nanocrystals on the assembly rate as well as the role of ligands. The kinetics of aggregation of the two most common crystal structures for CdQ nanocrystals was studied and it was determined that the hexagonal (wurtzite) crystal structure aggregated faster than the cubic (zinc blende) crystal structure. Once the crystal structure affects are accounted for, the relative redox properties of Q (Q= S, Se and Te) govern the reaction rate. Additionally, the chain length of the capping thiolate also affects the kinetics of aggregation, with longer chains leading to slower assembly rates. The synthetic levers studied in this section will be utilized in subsequent studies to form multicomponent gels, using the well-studied oxidative gelation of MQ NCs (M=Cd and Zn, Q= S, Se and Te).

Aim III: Synthesize multicomponent MQ materials of CdSe/ZnS with controlled phase segregation (presented in Chapter 5)

In this section, known synthetic levers to control kinetics of colloidal aggregation of single component systems, including concentration of NCs and oxidant, particle size, relative redox properties of Q (Q=S, Se and Te), steric bulk of the capping ligand, crystal structure and facet energy will be used to synthesize heterostructured MQ materials with two components (CdSe and ZnS NCs).[54, 83-84] One of the steps in the sol-gel synthesis of these MQ particle gels is the oxidation of the surface thiolate ligand; using a bulkier more sterically hindered ligand allows for more control over the kinetics of aggregation of these MQ NCs in solution. Previous work on the formation of PbTe gels utilized a bulkier 16-mercapothexadecanoic acid and trioctylphosphine oxide capping ligand to control the aggregation kinetics and allow the formation of high-quality PbTe gels.[54] When attempting to incorporate two MQ NCs with differing Q (Q=S and Se), the relative redox properties will control the rate of aggregation in solution, it is important for integrating two MQ components, that these affects be accounted for in the synthesis. In the present work, by adjusting

the steric bulk of the capping ligand, from a shorter-chain 11- carbon ligand, to a longer-chain 16-carbon ligand, the kinetics of colloidal aggregation, as defined by the redox properties of Q, can be modified. This allows for the synthetic tailoring of the resultant 3-D gel from a phase segregated co-gel to an intermingling of the two component materials.

CHAPTER 2: EXPERIMENTAL METHODS

2.1 Experimental Methods

This chapter describes the materials and synthetic methods that were used to synthesize nanocrystals and their heterogeneous assemblies. This chapter will include a discussion on the basic concepts of, and instrumentation for, material characterization. Metal chalcogenide (MQ) NCs were synthesized by several different variations of the solution phase synthesis, and structural, morphological and optical properties were characterized by powder X-ray diffraction (PXRD), transmission electron microscopy (TEM), energy dispersive spectroscopy (EDS), UV visible spectroscopy, photoluminescence (PL) spectroscopy, electron paramagnetic resonance spectroscopy (EPR), Fourier transform infrared spectroscopy (FT-IR) and inductively coupled plasma mass spectroscopy (ICP-MS). NC heterostructures with pSi wafers were characterized with scanning electron microscopy (SEM).

Kinetics of aggregation and gelation of NCs were studied by performing dynamic light scattering (DLS) and ^{1}H and ^{19}F nuclear magnetic resonance (NMR) spectroscopy. Wet gels were dried by supercritical CO_2 extraction to form aerogels and characterized by TEM, Diffuse-reflectance and PL spectroscopy.

2.2 Materials

Selenium powder (99.5%), stearic acid (95%), Bis(trimethylsilyl)sulfide (TMS), trioctylphosphine oxide (TOPO, 90%), tetranitromethane (TNM), 11-mercaptoundecanoic acid 95% (MUA), 1-tetradecylphosphonic acid (TDPA, 98%), tetramethylammonium hydroxide pentahydrate (TMAH, 97%,) 1-octadecene (90%, tech), oleic acid (90%, tech), hexafluorobenzene, 4-fluorothiophenol, triethylamine and 16-mercaptohexadecanoic acid (MHA) were purchased from Sigma-Aldrich. Trioctylphosphine (TOP, 97%), zinc chloride (97%), lead oxide, tellurium powder, cadmium oxide (99.999%) cadmium chloride and sodium sulfide were purchased from Strem Chemicals. Oleylamine (OAm, C18 content (80−90%) was purchased from ACROS. Ethanol (200 proof) was purchased from Decon Laboratories, Inc. Cadmium chloride (99.99%) was purchased from Alfa-Aesar. Toluene, methanol, hexane, acetone and ethyl acetate

were purchased from Mallinckrodt. d_6-acetone was a purchase from Cambridge Isotopes Laboratory Inc. TOPO was distilled before use; all other chemicals were used as received.

2.3 Synthetic Methods

2.3.1 Synthesis of Metal Chalcogenide Nanocrystals (MQ NCs), Ligand Exchange, and Sol-gel Assembly (Gel) Monoliths and Multicomponent Materials

The synthesis procedures for MQ NCs are described in Chapter 3-5 in detail along with purification, ligand exchange, and multicomponent material assembly procedures. Precursor materials were prepared in an inert-atmosphere glove box, and required synthetic steps were performed under inert atmosphere using Schlenk line techniques.

2.3.2 Spin-Coating Deposition

Spin-coating is a deposition technique for uniform thin films on a flat substrate (i.e. silicon wafers). The spin coating process typically begins with a solution of desired concentration, being deposited on the substrate, usually through drop-cast techniques. The rapid acceleration of the substrate allows the solution to flow radially through centrifugal force while the excess solution can be ejected from the substrate.[85] As the spin coating proceeds, the film continues to slowly thin-out due to solvent evaporation until pressure effects causes the film to reach an equilibrium thickness. A simple model of the spin coating process treats the film thinning process as two distinct steps starting with 1) film thinning specific to the solution radial flow which can be described using the equation for a Newtonian liquid on a rotating disk, Eq. 2.1:[86]

$$\frac{dh}{dt} = -\frac{2\rho\omega^2 h^3}{3\eta_0} \tag{2.1}$$

In Eq. 2.1, h is the film thickness, t is the time, ρ is the density of the solvent, ω is the revolution per minute (rpm) of the device, and η_0 is the viscosity of the solution. The next step 2) is following the thinning of the film to a certain level it is considered immobile on the substrate and solvent evaporation rate (E), will control the film thickness. This can be calculated using the mass transfer expression, where k is the

mass transfer coefficient, x_1^0 is the initial solvent mass fraction of the coating solution, and $x_{1\infty}$ is the solvent mass fraction in equilibrium with the solvent mass fraction in the gas phase, in Eq. 2.2.[87]

$$E = k(x_1^0 - x_{1\infty}) \tag{2.2}$$

For this dissertation research, spin coating was performed on a Spin Coater Model P6700 series at 2500 rpm for 15 second intervals.

2.3.3 Physical Deposition Techniques for Thin Films

There are two different types of physical vapor deposition (PVD) techniques for growing thin films, both useful for thin film electrodes in device construction. The first and most common type of PVD for the deposition of metal thin films is evaporation, in which target atoms are removed from the source thermally. The second type is the sputter deposition of thin films, a type of physical vapor deposition method where materials are ejected from a source or target to a substrate by the impact of gaseous ions.[88]

During the thermal evaporation process, the maximum evaporation rate happens when the number of vapor molecules discharged corresponds to the number required to exert the equal vapor pressure with none of them returning to the source. This gives the equation for the rate of evaporation for solid surfaces as Eq. 2.3.[88]

$$\Phi_e = \frac{\alpha_e N_A (P_e - P_h)}{\sqrt{2\pi MRT}} \tag{2.3}$$

In Eq. 2.3, Φ_e, is the evaporation flux in number of atoms per unit area per unit time, and α is the coefficient of evaporation (between 0 and 1). The maximum evaporation rate happens when α=1 and $P_h = 0$, and P_e is the equilibrium pressure at temperature, T, and P_h is the hydrostatic pressure acting on the evaporant. The evaporation process takes place under high vacuum, to give high purity thin films. High energy sources (electron beam, molecular beam epitaxy, resistive evaporation) are used to evaporate the source, which is then deposited on the target Figure 2.1.

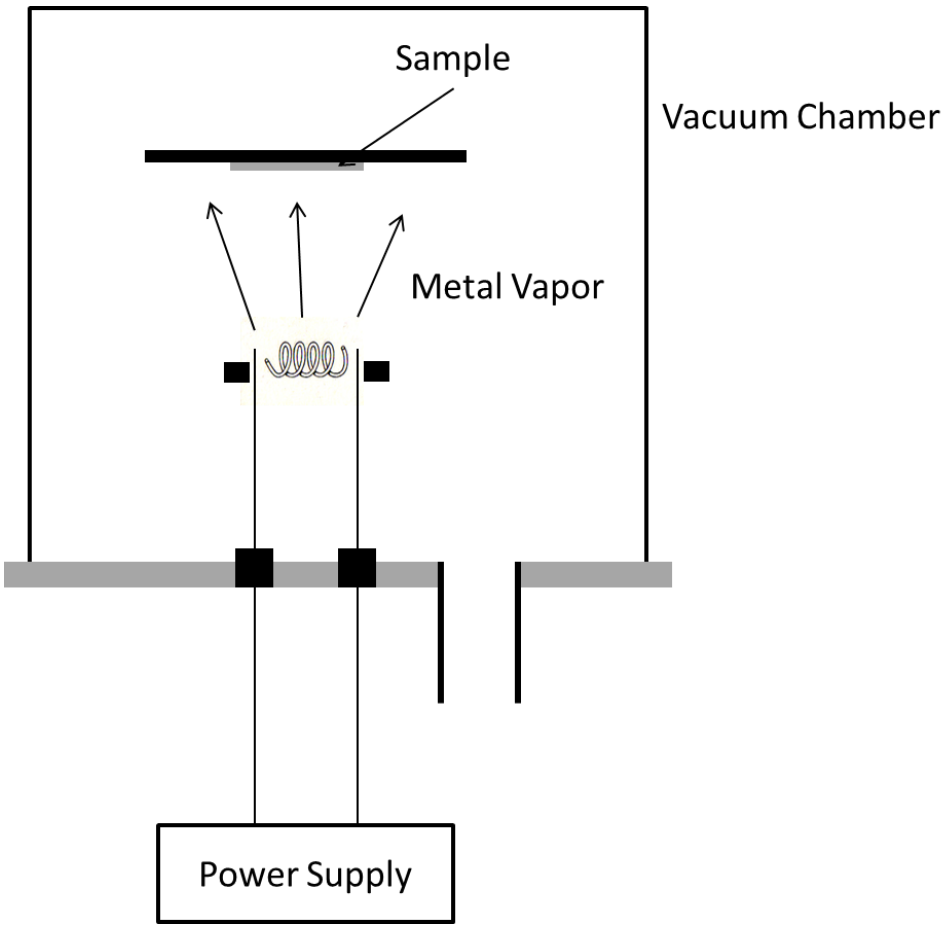

Figure 2.1. Schematic of the evaporative deposition chamber (adapted from Ohring).[88]

For PVD, It is vital to understand the different types of ion collisions with target surfaces, as shown in Figure 2.2. Each type of collision depends on the type of ion (mass, charge) and the energy of that ion. Each of these types of collisions can be used for different analytical and deposition techniques, for example, Rutherford backscattering can be utilized to determine thickness and composition of films.[88]

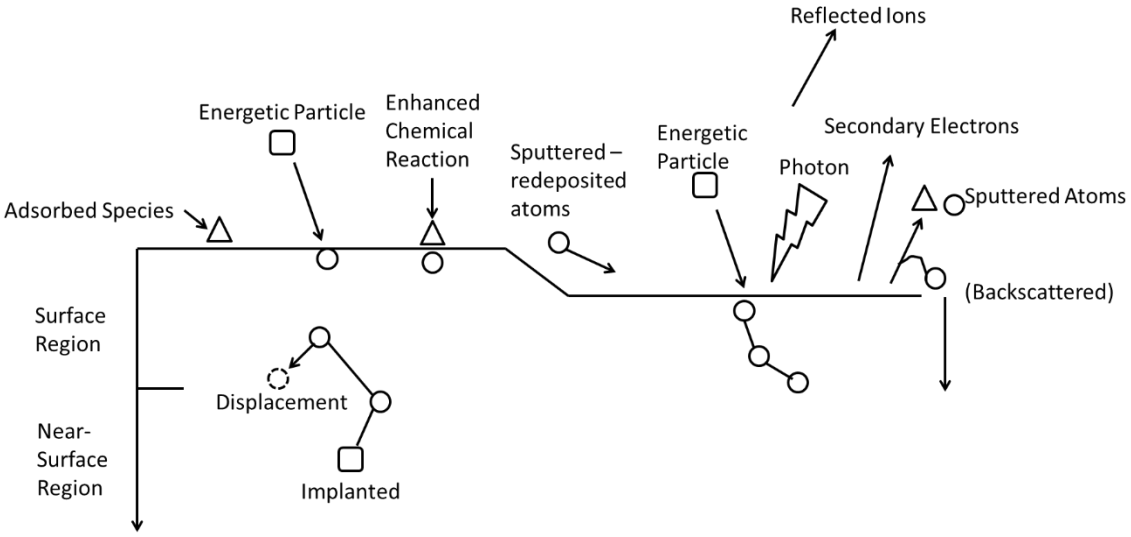

Figure 2.2. Representation of the different types of ion collisions with a surface (adapted from (Ohring).[88]

One collision type that can follow the impact of an ion is a collision event, which results in the ejection of an atom from the source; this is referred to as sputtering. The sputtering event is related to momentum energy transfer from higher energy particles to the surface atoms of the source. To measure the efficiency of the sputter process, the term sputter yield is used and defined as the number of atoms or molecules ejected from the source's surface per incident ion. There are four main types of sputter deposition processes dc, RF, magnetron and reactive sputtering. In a typical sputtering device (Figure 2.3) a target (the cathode) is in a high vacuum chamber (specifically RF sputtering), and high energy is used to generate the ion bombardment that strikes the substrate (the anode); the high energy metals that are released strike the target and coat it with a thin film of the desired metal. [88]

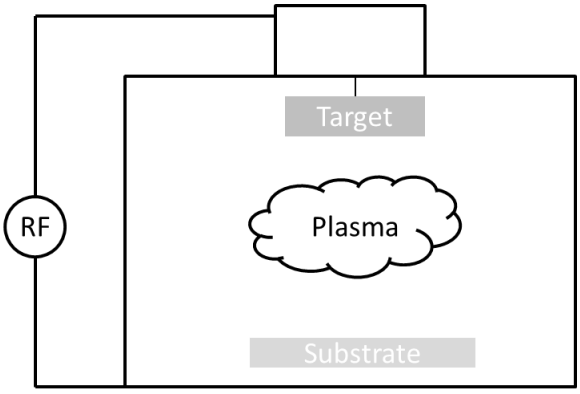

Figure 2.3. Schematic diagram of an RF sputtering device.

For this dissertation research, an Al thin film was deposited using a Temescal BJD 1800 e-beam evaporator with an Al target on the unpolished side of a Si wafer. The programmed rate was 2 Å/sec for a final thickness of 1000 Å at a power of 20.3%. Finally, the ITO layer was deposited over the active layer of the devices, in an RF magnetron system CVC over 30 mins at a power of 200 W under argon gas, for a final thickness of 1500 Å.

2.3.4 Synthesis of Porous Si (pSi)

The porous silicon was produced by anodizing a highly-doped silicon wafer, in this case, n-type, 0.002 Ω-cm, <100> orientated, 375 µm thick, using a 1:3 HF: Ethanol solution. [89-92] Anodically etched porous silicon is a support used in LEDs[93], photodetectors[94] and photonic crystals[95], due to their unique charge transport properties. The anodization of the Si wafer was performed in an open cell with an O-ring seal on a 0.5 cm^2 active area (Figure 2.4a), where the Pt wire is the cathode and the Si wafer is the anode. During the electrochemical reaction there are several factors that influence the pore depth and diameter. The electrolyte is HF dissolved in ethanol, which increases the wettability of the hydrophobic Si allowing the HF solution to more easily infiltrate the pores in Si. The ethanol solution also more easily releases the H_2 bubbles formed in the reaction when compared to an aqueous solution. [92] The second factor that affects the porosity is the constant current which allows for improved control of porosity relative to constant bias, pore thickness and sample reproducibility. Finally the cell where the anodic etching is

performed will affect the final quality of the pSi (smoother pore walls); the basic electrochemical cell uses a Teflon beaker (Figure 2.4b), which is inert to HF acid.

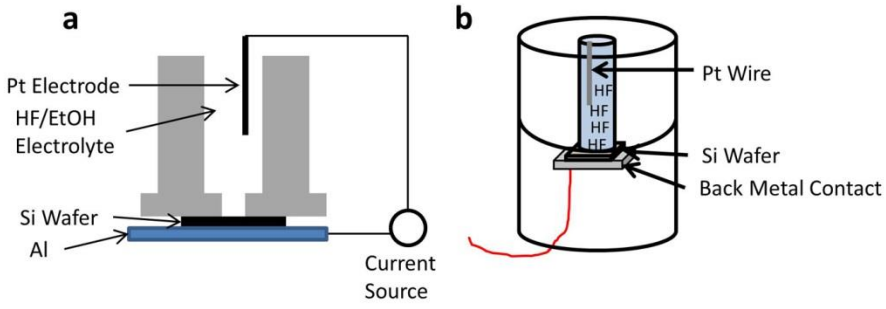

Figure 2.4. a) Schematic of the anodization cell (adapted from Bisi) [92] b) diagram of the actual anodization chamber provided by Weinberg Medical Physics.

The mechanism of pSi formation is still being debated, but it is generally accepted that h^+ are required for pore formation, where hydrogen evolves during the silicon dissolution. The stable product for Si in HF:ethanol solution is in the form H_2SiF_6, or possibly one of its ionized forms. This means that during pore formation, only two of the four available Si electrons participate in the charge transfer process, while the remaining two Si electrons participate in dihydrogen liberation as shown in Scheme 2.1.

$$Si + 6HF \longrightarrow H_2SiF_6 + H_2 + 2H^+ + 2e^- \qquad \text{(Scheme 2.1)}$$

If the sample is not forming pores it has moved into electropolishing, in which current efficiencies are four electrons per dissolved Si atom shown in Scheme 2.2.[96]

$$Si + 6HF \longrightarrow H_2SiF_6 + 4H^+ + 4e^- \qquad \text{(Scheme 2.2)}$$

The most widely accepted dissolution mechanism is based on the surface bound oxidization scheme where hole capture and electron injection leads to the Si^{2+} oxidization state as shown in Figure 2.5. One of the first steps is attack of the Si-H bond by the fluoride ion to produce a bound H_2^- ion, then a second

attack by a fluoride ion, followed by hydrogen gas evolution. Finally, HF attack on the Si-Si bonds produces silicon tetrafluoride.[97]

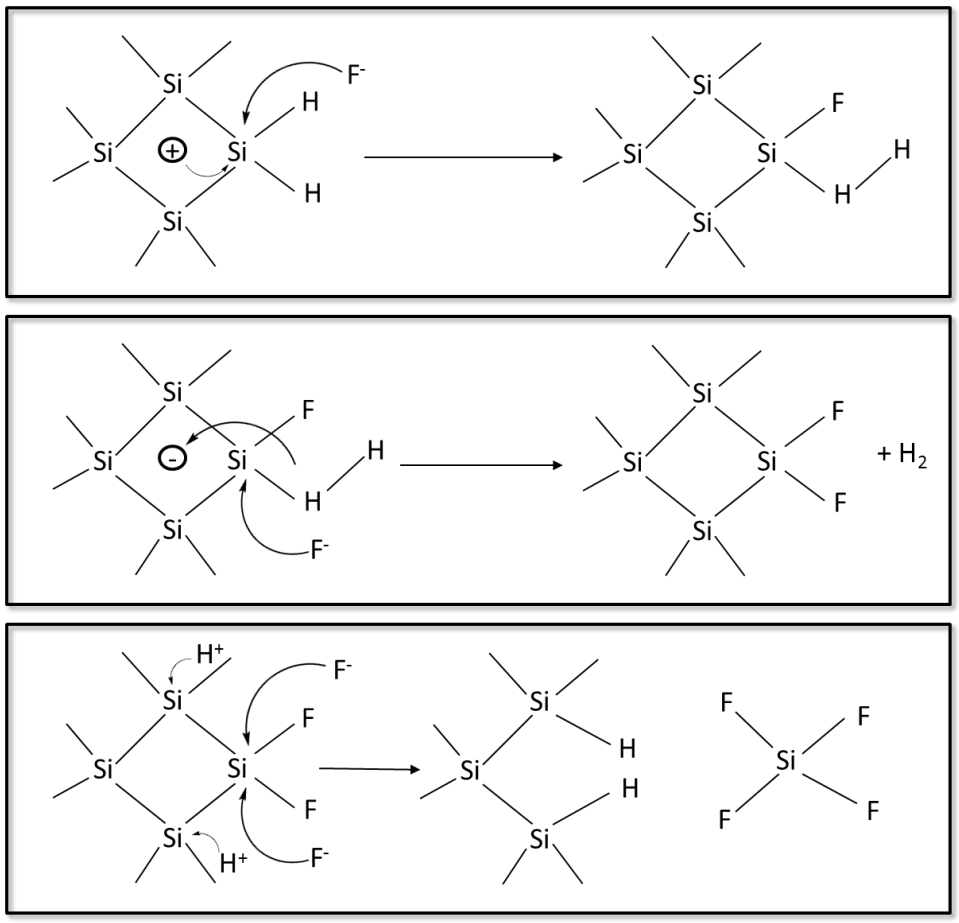

Figure 2.5. Proposed silicon dissolution scheme (adapted from Lehmann).[97]

The anodic etch times were adjusted to produce samples of varying pore depths based on a procedure developed at Weinberg Medical Physics.[20] Due to specific limitations of the etching chamber, no more than 90 seconds at 100 mA/cm^2 was used, which produced pSi samples with pore diameters between 80-100 µm, and pore depths between 10-20 µm.

2.3.5 Oxidative Sol-gel Assembly

The oxidative sol-gel assembly process is useful in producing solid materials from nanomaterials in solution. The technique is common for the polymeric fabrication of metal oxides and involves the conversion of monomers or nanoparticles into a colloidal solution (sol) that acts as the precursor for a network (or gel). Typical precursors used in this synthetic technique are metal alkoxides as shown in the Scheme 1.1-1.3 in Chapter 1. The low dimensionalities of the resulting gels along with interconnected pores are desirable properties for applications, such as thermal/acoustic insulation, catalysis, and sensor devices.[98] We have developed an oxidative sol-gel assembly method for metal chalcogenide nanomaterials. We have shown this technique is applicable a diverse group of metal chalcogenides, such as ZnS, CdS, CdSe, PbS and PbTe.[38, 52-53, 56, 58, 99-104] The initial step is the oxidative ligand loss of surface thiolate groups from the metal chalcogenide nanoparticle by the addition of an appropriate oxidant (i.e. H_2O_2, tetranitromethane, and hv/O_2) resulting in the oxidation of the thiolate (RS^-) to form a disulfide by-product.[51, 105] The next step is the removal of some of the surface metal ions into solution, followed by the oxidative formation of di- and polychalcogenide linkages ($2Q^{2-} \rightarrow Q_2^{2-} + 2e^-$) (Figure 1.7).[58]

2.3.6 Aerogel Formation via Supercritical Drying

Supercritical drying is a process of removing solvents from the monolithic wet gels in a controlled way, without destroying the 3D structure. In supercritical drying, the solvent is exchanged with liquid CO_2 (or another applicable solvent), followed by the gel being heated above the critical temperature of the solvent (T_c), and above the critical pressure (P_c), of the pore liquid. The phase diagram in Figure 2.6 shows that above the T_c and the P_c of the liquid, the liquid-vapor phase boundary of the pore solvent does not exist and liquid and vapor densities are equal. The supercritical solvent is then slowly displaced as a gas without destroying the pore structure. Because of the lack of liquid-vapor interface there is an absence of the capillary forces on the pore walls that lead to the pore collapse during ambient drying. Liquid CO_2 is

commonly used as the solvent for supercritical drying based on its low critical temperature (31 ˚C) and pressure (7.36 MPa).[37]

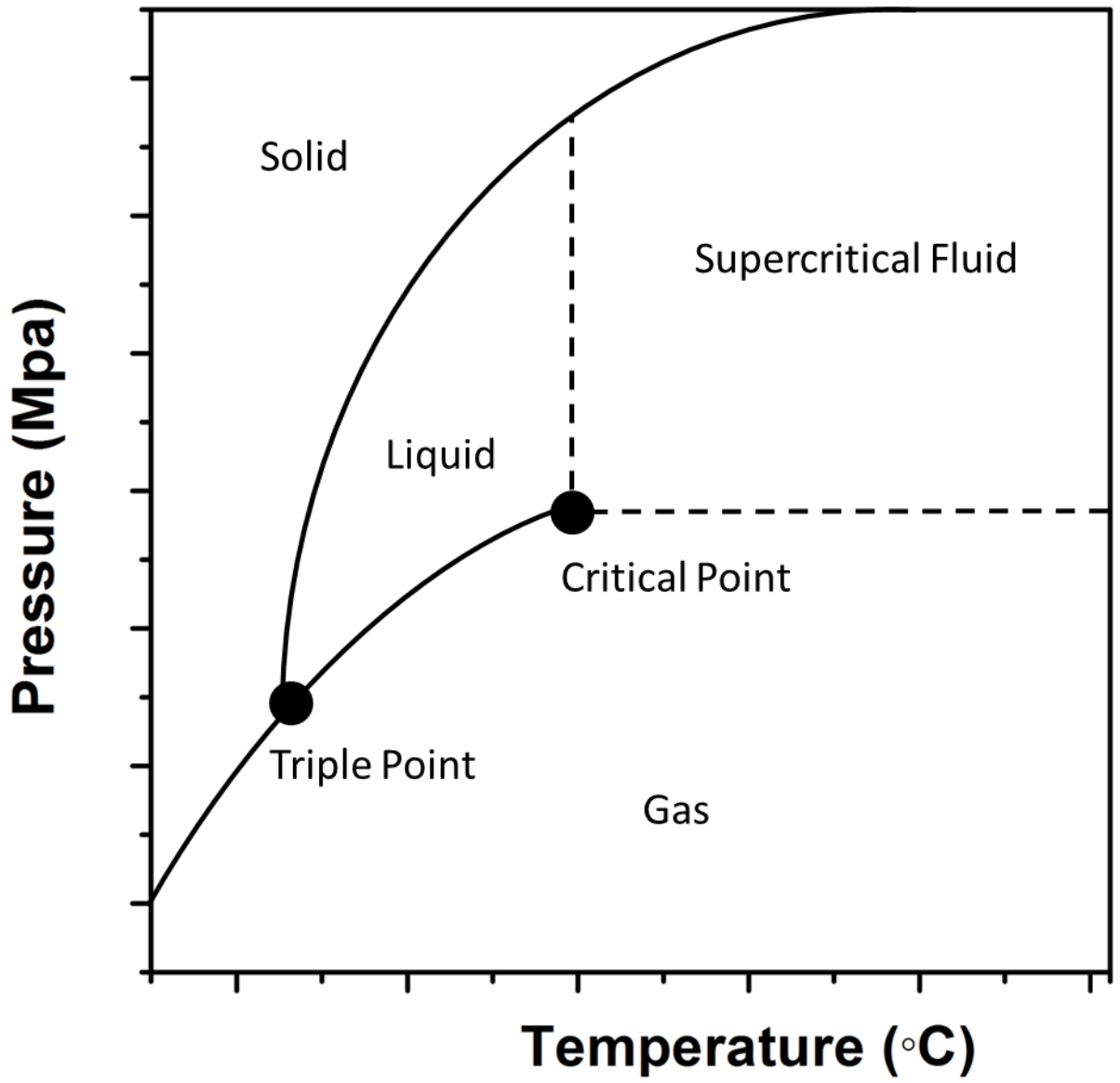

Figure 2.6. A phase diagram for CO_2 showing the liquid-vapor phase boundary and the critical point above which densities of the liquid and vapor are the same (adapted from Brinker).[37]

In this dissertation research, a Tousimis Autosamdri-931 model critical pointer dryer was used to dry solvent-exchanged wet gel monoliths. The wet gel monoliths were placed in the 2.50 in. ID (internal diameter) drying chamber and the solvent (methanol, ethanol or acetone) were exchanged with liquid

CO_2. During this cycle, the chamber was drained twice and refilled with liquid CO_2 for 1 hour hold cycles, and then the temperature of the chamber was increased up to 39 ˚C and the pressure was maintained above the critical pressure of CO_2 for 10 minutes. Finally, the pressure of the chamber was bled slowly while maintaining the temperature at 39 ˚C.

2.4 Materials Characterization

2.4.1 Dynamic Light Scattering

Dynamic light scattering (DLS) is an analytical technique that can be used to determine the size distribution profile of small particles, polymers or proteins in solution. Due to the interaction of electromagnetic radiation with materials, the absorption, scattering, or the combination of the absorption and scattering, depends on the wavelength of the incoming light and properties of the material. This phenomenon is exploited by various analytical techniques including UV-visible spectroscopy, photoluminescence spectroscopy, optical microscopy, etc. Specifically, for light scattering, the emission of light is due to the oscillation or agitation of the electron cloud of the material, which is produced by the electric-field constituent of the incident light. For DLS, as the light passes through the sample of particles suspended in solution there is elastic or quasi-elastic scattering, which means the frequency of emitted light is very similar in energy to the incident light, but propagated in a different direction.[106]

Elastic scattering is based on the particle size, with two types of scattering processes occurring. If the particle diameter (d) is much smaller than the wavelength of the incident light (λ), the light scattering is described by the Rayleigh theory (Figure 2.7) where the scattering intensity, I, is equivalent in the forward and reverse directions, and is dependent on the wavelength of the incident light ($I \propto 1/\lambda^4$). For particles with diameters equal to or greater than the wavelength of the incident light, the Mie scattering is dominant, and more of the light is scattered in the forward direction, with the scattering more independent of incident wavelength.[106]

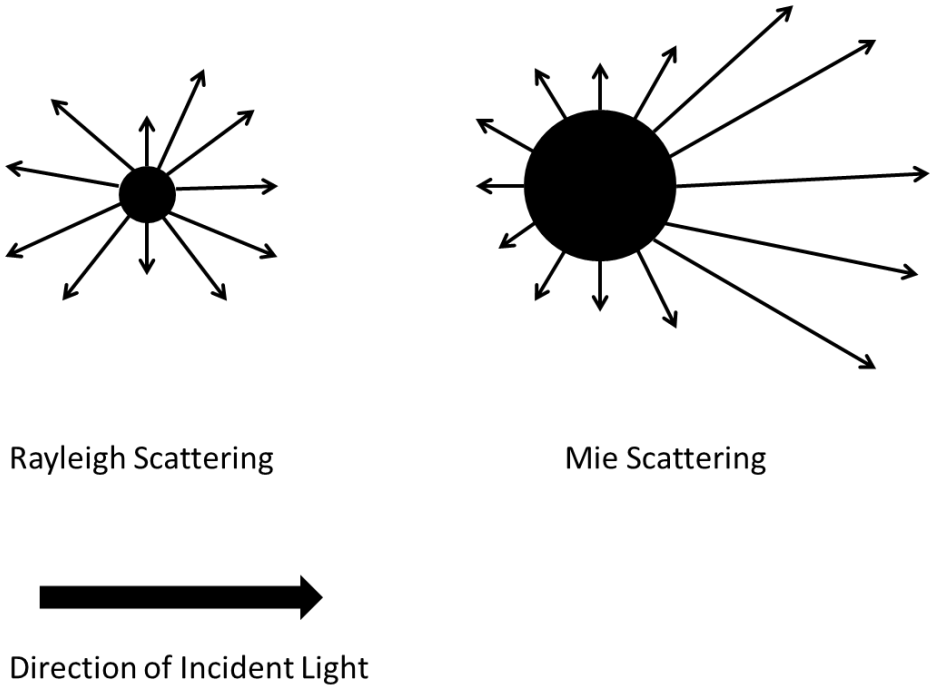

Figure 2.7. The two types of elastic scattering, Rayleigh scattering and Mie scattering.

In a typical DLS instrument setup, a monochromatic light source such as a He-Ne laser is directed through a polarizer and into a sample. The light is scattered and goes through a second polarizer at a specific angle where it is collected by a photomultiplier and the resulting image is collected by the detector (Figure 2.8). Since all of the materials in the solution are being bombarded with the incident light, diffracting the radiation in all directions, there is either constructive interference (light regions) or destructive interference (dark regions). When replicated at short time intervals, the resulting set of speckle patterns are analyzed by an autocorrelator that monitors the intensity of light at each spot over time. The correlator then constructs the autocorrelation function, which is then passed to the computer that performs the data analysis.

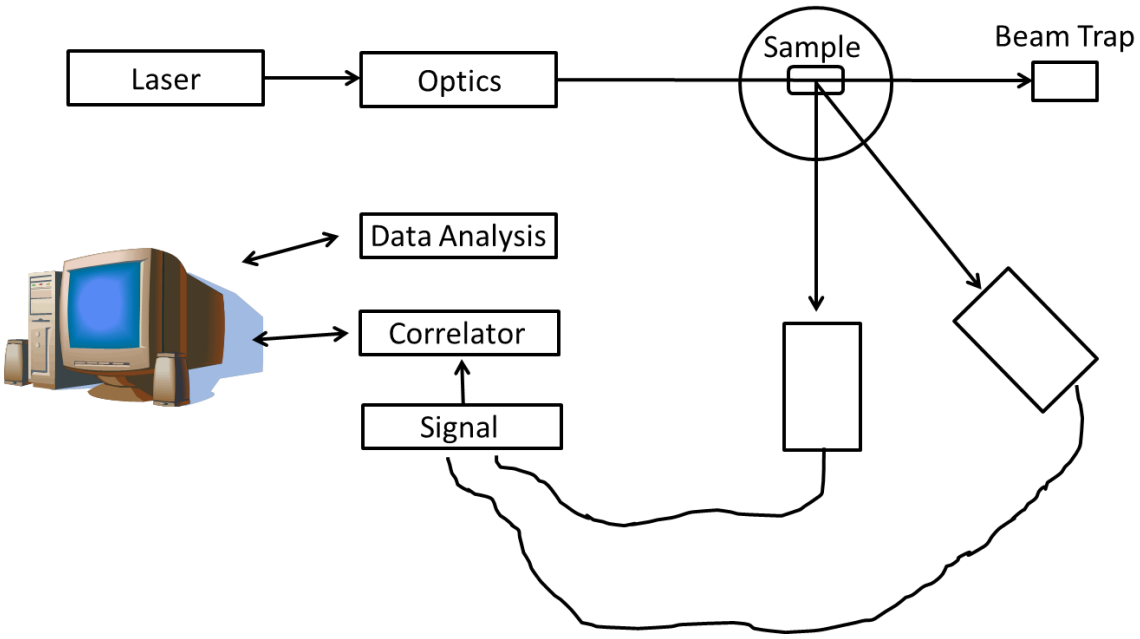

Figure 2.8. Schematic diagram of the dynamic light scattering instrument (adapted from Xu).[107]

The intensity of the scattered light varies with time, based on the Brownian motion of the nanoparticles and nanoparticle aggregates in the solvent. The normalized second-order intensity correlation function $g(2)\ (\tau)$ is attained with the digital correlator in the DLS instrument through auto-correlation of these intensity fluctuations of the scattered light over a short time interval (Eq. 2.4).

$$g^{(2)}(\tau) = \frac{\langle I(0)I(\tau)\rangle}{\langle I(0)\rangle^2} \tag{2.4}$$

In Eq. 2.4, $I(\tau)$ is the scattering intensity over the short decay time interval, τ. To relate the first order electric field function $g^{(1)}\ (\tau)$, to the second-order intensity correlation function $g^2\ (\tau)$ the Siegert relation is used (Eq. 2.5).

$$g^{(2)}(\tau) = B\left(1 + \beta\left|g^{(1)}(\tau)\right|^2\right) \tag{2.5}$$

For Eq. 2.5, B is the baseline of the correlation function and β is the coherence factor. A polydisperse solution is formed during the aggregation and gelation process, so $g^{(1)}$ must be denoted as a sum or distribution of exponentials (Eq. 2.6).

$$g^{(1)}(\tau) = \int G(\Gamma)\exp(-\Gamma\tau)\,d\Gamma,\ where\ \int G(\Gamma)d\Gamma = 1 \tag{2.6}$$

Where $G(\Gamma)$ is the distribution function of Γ.[106, 108-109] The autocorrelation functions utilize the method of cumulants yields for the mean decay rate $\overline{\Gamma}$, which is equal to $\overline{D}q^2$. The value $\overline{D}$ is the average translational diffusion coefficient and q is the scattering vector (Eq. 2.7).

$$q = \frac{4\pi n}{\lambda} \sin \theta/2 \tag{2.7}$$

In Eq. 2.7, for the scattering vector (q), θ is the scattering angle and n is the refractive index of the solvent. The average hydrodynamic radius of the spherical particles ($\overline{R}_h$) is calculated from the Stokes-Einstein relationship, Eq. 2.8.

$$\bar{R}_h = \frac{k_B T}{6\pi\eta\bar{D}} \tag{2.8}$$

Eq. 2.8, is based on the absolute temperature T, and the viscosity of the solution η. The particle radius, as measured by the DLS instrument, is denoted as the hydrodynamic radius ($\bar{R}_h$) because it is calculated based on the diffusion of the particles in a fluid. Therefore, the particle radius measured by DLS corresponds to the diameter of a sphere that has the same translational diffusion coefficient as the particle in the solvent.[110]

For this dissertation research, the time-resolved dynamic light scattering (TR-DLS) measurements were performed using a Zetasizer Nano ZS instrument (Malvern Instruments, Westborough, MA) with a He-Ne laser beam at 633 nm and the detector positioned at 173°. The Z-average hydrodynamic radius (R_h) was determined using the Zetasizer software (version 6.2) provided by Malvern. For the TR-DLS measurements the autocorrelation functions were accumulated for at least 30 s over different time periods after the addition of the oxidizing agent.

2.4.2 Powder X-ray Diffraction

Light waves spread out as a result of passing through a narrow aperture; this is followed by interference between the wave forms produced, either constructive interference or destructive interference. The source for diffraction in a powdered crystalline material is often x-rays, neutrons or electron beams, because these sources have the correct frequency to match with inter-atomic-scale

diffraction. X-ray diffraction, based on the wide-angle elastic scattering of X-rays by the periodic electron densities of a crystal, is one of the most basic and widely used techniques to determine the structures of solids. Powder x-ray diffraction is mainly used for material identification in polycrystalline solids, as well as crystallite size and strain.[111]

When X-rays reach the material, the atoms of the sample react similarly to a diffraction grating, producing bright spots at particular angles based on the d-spacing between lattice planes. The angle where these peaks occur can be used to determine the spacing of the lattice planes of the crystal structure of the material using Bragg's law Eq. 2.9.

$$n\lambda = 2dsin\theta \tag{2.9}$$

The X-rays are incident on an atom and reemitted as Rayleigh scattering (or elastic scattering), where d is the lattice spacing in the Bragg diffraction. The two beams have identical wavelength and phase as they interact with the crystalline solid and are scattered off two different atoms in the material separated by distance d. The beam striking the lower lattice plane travels an extra length of 2dsinθ, to achieve constructive interference; this happens when the length is equal to an integer multiple of the wavelength (Figure 2.9). [111]

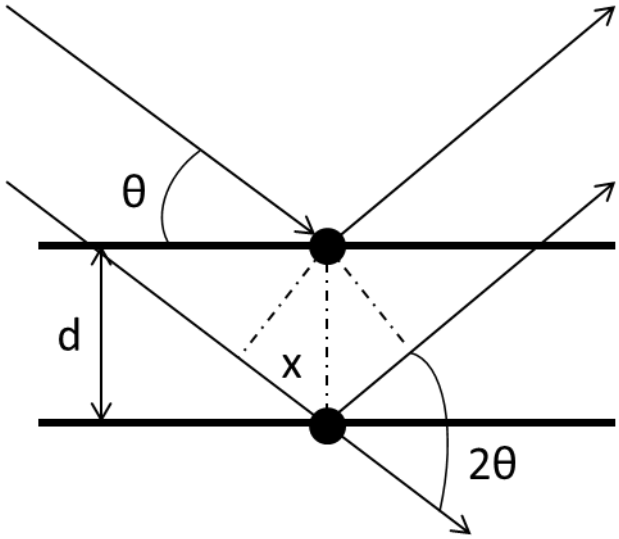

Figure 2.9. Illustration of X-ray diffraction on a set of parallel crystal planes and Bragg's Law (adapted from Pecharsky).[111]

Focusing powder diffractometers operate in the θ - 2θ scanning region where the incident beam forms the 2θ angle with the emission beam (Figure 2.10). The incident x-ray beams are produced in a sealed tube or rotating anode where high energy electrons collide with a metal target (Cu or Mo) that releases electrons from the material's K shell. Electrons from the materials L and M shells transitioning to the K shell generate X-rays. This high energy X-ray spectrum passes through slits that limit the divergence of the beam perpendicular to the plane to increase the resolution (Soller Slits). The diffracted beam is monochromatized using a β-filter, since fluorescent X-rays need to be suppressed to reduce the background noise. The intensity of the diffracted X-rays as a function of angle is measured using a detector such as scintillation detector or position sensitive detector (PSD).[111]

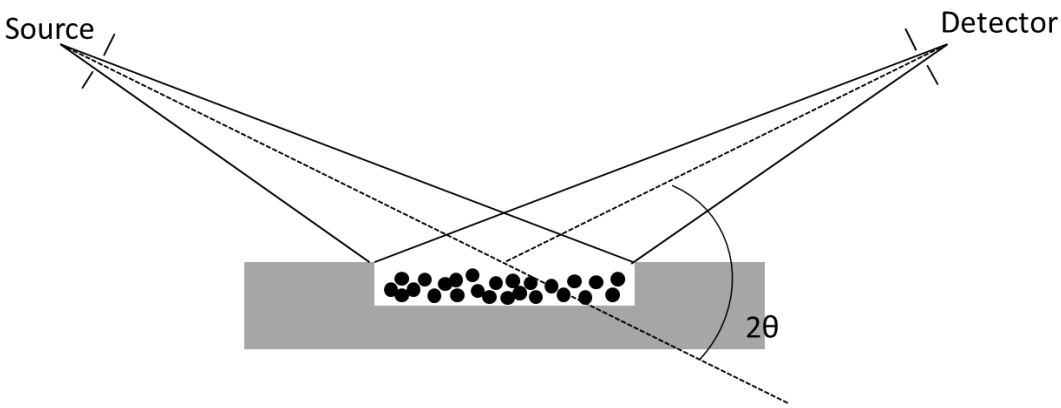

Figure 2.10. Diffraction geometries specifically for reflection mode in PXRD (adapted from Pecharsky).[111]

The reflection mode geometry takes full advantage of the beam focusing on the sample, with the drawback being that the sample may exhibit preferred orientation if crystallites are anisotropic. This geometry is known as the Bragg-Brentano method and is used for high resolution and high diffraction intensity spectra, along with also enabling an easy and straight forward method for sample preparation.

In a typical XRD experiment, the solid sample is placed on a zero background holder and the intensity of the diffracted X-rays is measured as a function of the Bragg angle, 2θ. Multiple Bragg reflections occur from the different sets of crystal planes in the powdered material, which leads to the formation of multiple peaks in the XRD pattern. The peak shape, position and intensity are affected by the structure and constituents of the powdered sample. The unit cell proportions determines the peak positions and the peak intensity depends on the atomic form factors and structure including the spatial distribution of atoms in the unit cell.[111] This lets the phase of the powdered crystalline sample be assigned using a diffraction pattern database.

For nanoparticles, the smaller crystallite size results in peak broadening in the XRD pattern, this is because of a reduction in the amount of crystal planes, which means that there is incomplete destructive interference because of the short coherence lengths. The average nanocrystal size (D) can be determined using the Scherrer equation Eq. 2.10.

$$D = \frac{k\lambda}{\beta \cos\theta} \quad (2.10)$$

In Eq. 2.10, β is the full width at half maximum of the angle θ, and the k value is a shape factor that approaches unity; for spherical particles a value of 0.9 is typically used in the Scherrer equation.[112]

For this dissertation research, PXRD was performed on a Bruker D2 Phaser using the Kα line of a Cu anode source (30 kV, 10 mA). Samples were deposited on a zero background quartz holder, and data was collected over the 2θ range 20-60°.

2.4.3 Nuclear Magnetic Resonance Spectroscopy

A common analytical technique to identify organic compounds, nuclear magnetic resonance spectroscopy (NMR) exploits the magnetic properties of certain atomic nuclei. It is used mostly for the determination of the physical and chemical properties of atoms, including structure, reaction states and chemical environment. The principle behind NMR spectroscopy is based on the nuclear spin (I) of each atom, which causes a small magnetic dipole moment. The gyromagnetic ratio (γ) gives the correlation between the magnetic moment and the nuclear spin, which is a constant for every different nucleus. The spins are in multiples of 1/2 (I = 1/2, 1, 3/2 ……), but the most common is I = ½ (Figure 2.11). For the spin to be zero, (S= 0) the atomic number and the atomic mass are both even numbers, and then the nucleus has no magnetic moment (it is NMR silent). For S=1/2, the nuclei is spherical in shape, and for higher spin quantum numbers the nuclei is quadrupolar.[113]

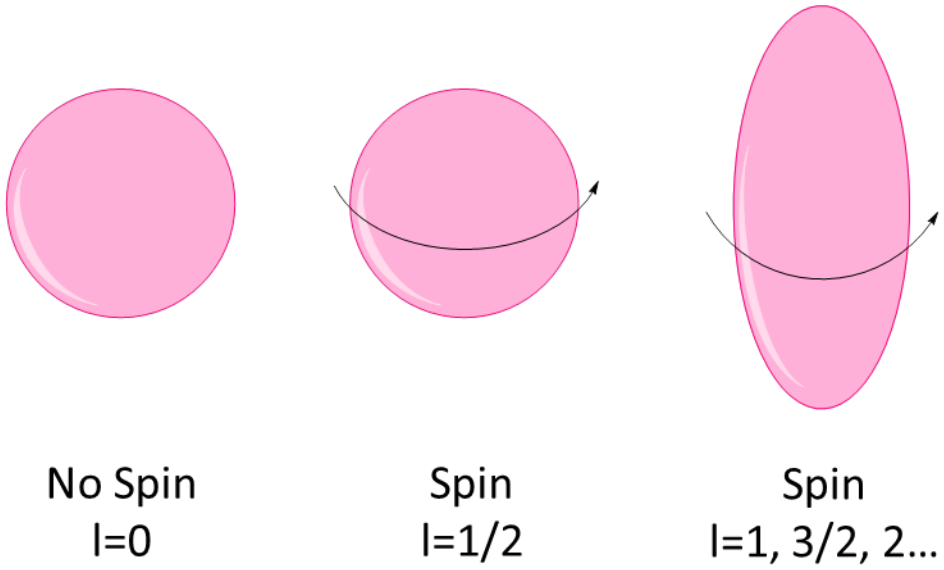

Figure 2.11. The three types of nuclei spin quantum number (adapted from Lambert).[113]

The dipole moment of the nuclei can orient itself in a magnetic field (B_0). For $I = 1/2$, the spin has two orientations, with or against the magnetic field (Figure 2.12).[114]

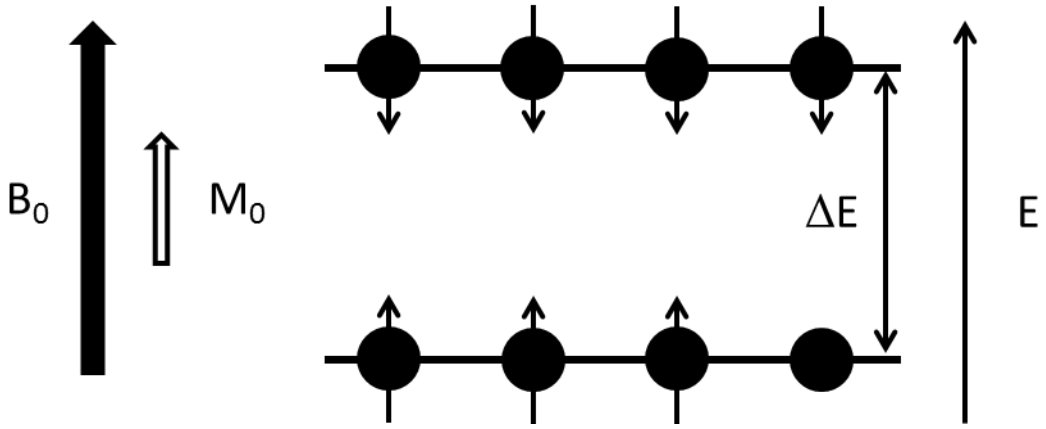

Figure 2.12. Spin alignment in the external magnetic field for I=1/2 spin nuclei (adapted from Zerbe).[115]

As seen in Figure 2.12, the alignment in the magnetic field, gives rise to two separate energy levels, the nuclei with parallel alignment are slightly lower in energy. The two spin states, α and β are eigenstates, being either positively or negatively oriented to the magnetic field. The α and β spin states are filled

following the Boltzmann distribution in Eq. 2.11 which means that there is a slight excess of population in the lower energy α states.

$$\frac{N(\beta)}{N(\alpha)} = \exp\left(\frac{-\Delta E}{kT}\right) \tag{2.11}$$

This excess of the lower energy states causes a macroscopic magnetic moment that is aligned with the external magnetic field at thermal equilibrium. When a radio frequency (RF) field is applied to this system, at 90° the magnetization is rotated into the xy plane, as the external magnetic field is considered the z direction (Figure 2.13).

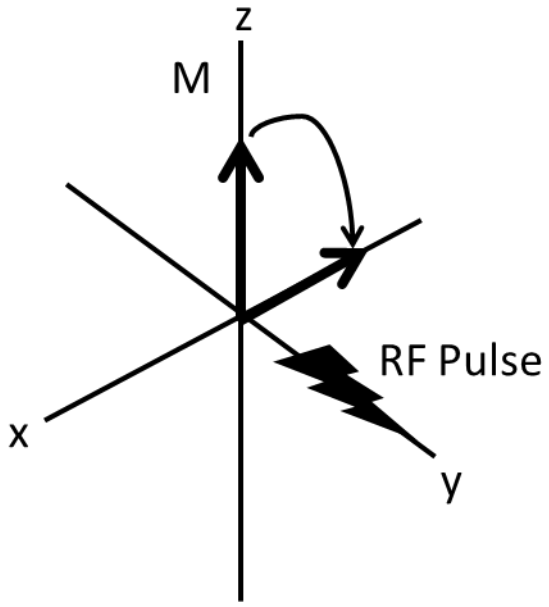

Figure 2.13. Image of the application of an RF pulse that rotates the magnetization in the xy plane (adapted from Simon).[115]

Precession is the magnetic moment rotating around its axis, because it is not coaligned with the external magnetic field. The frequency of the procession is the Larmor frequency ($\omega_0\, rad/s$) which is what NMR spectroscopy measures as described in Eq. 2. 12.

$$\omega_0 = -\gamma B_0 \tag{2.12}$$

The precession of the magnetization in the xy plane due to the application of the RF pulse at 90° (Figure 2.14), makes an oscillating signal in the detection coil called the free induction decay (FID), so signal frequency is proportional to the spin precession frequency.

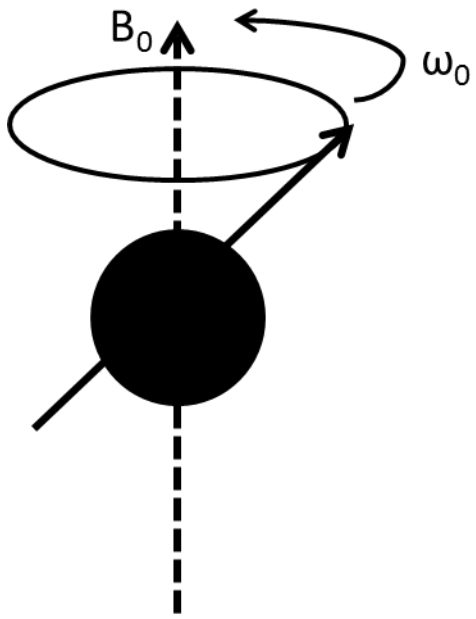

Figure 2.14. Image of the magnetic moment of an individual spin precessing around the external magnetic field (adapted from Zerbe).[115]

For solution phase NMR spectroscopy, a glass tube with deuterated solvent along with the sample being measured, is placed into the instrument, between the RF coils as they are used for both pulsing the RF field and receiving the signal. The current collected by the coil is next sent to the receiver and converted by the analog-to-digital converter to give the FID signal. The FID signal, which corresponds to the intensity/time pairs, is converted through Fourier transform into an intensity/frequency signal (Figure 2.15). When the sample is placed in the magnetic field of the instrument, NMR active nuclei will absorb the electromagnetic radiation at a frequency distinctive to each isotope.[114] The magnetic field strength directs the resonant frequency and strength of the signal.

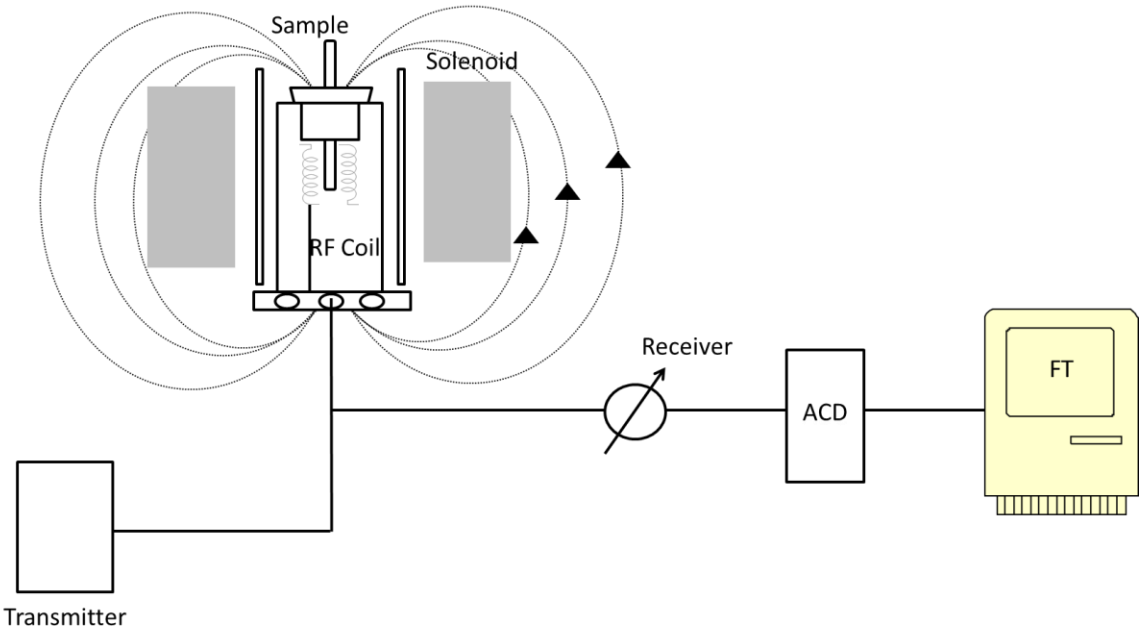

Figure 2.15. Schematic design of the NMR spectroscopy instrument (adapted by Zerbe).[115]

Chemical shifts are related to the electron density around the nucleus, these shifts in the NMR spectrum are used for chemical identification. Application of RF frequency to the sample with energy corresponding to the energy spin state separation of specific nuclei will cause excitation of those set of nuclei from the lower energy spin state to the higher energy spin state. Even if all the nuclei in the material have the same magnetic moments, they do not give resonant signals of the same frequency, due to the different electronic environments of the nucleus of interest. Since each atom electron cloud will also generate a local magnetic field, the protons can be shifted, affecting the resonant frequency. Different functional groups will affect the resonant frequency of the nucleus. For example, electron-withdrawing groups which can deshield the protons in a molecule by reducing the local electron density. Since the frequency of a specific nucleus is proportional to magnetic field, it is common to report chemical shift relative to a known standard. The chemical shift of a nucleus (x) is described by Eq. 2.13, where ω_{ref}, is the frequency of a standard, usually tetramethylsilane (TMS), and the values are given in parts-per-million (ppm).

$$\delta(x) = \frac{\omega_x - \omega_{ref}}{\omega_{ref}} \times 10^6 \quad (2.13)$$

To describe whether a certain shielding effect will shift the frequency to a lower or higher ppm value, an upfield shift describes a move to lower ppm, and a downfield shift is a move to higher ppm.

For this dissertation research, the ^{1}H and ^{19}F NMR spectroscopy measurements were performed on a Varian Mercury 400 NMR spectrometer in d_6-acetone at room temperature. Chemical shifts were reported in parts per million. The solvent volume in the NMR tubes was held constant (750 µl) for each sample, and solid NCs were dispersed in the solvent.

2.4.4 Electron Paramagnetic Resonance Spectroscopy

Electron paramagnetic resonance spectroscopy is similar to NMR spectroscopy, and is used to study unpaired electrons in a material. Electrons have a spin quantum number ($S = 1/2$), with the two magnetic constituents $m_s = +\frac{1}{2} and\ m_s = -\frac{1}{2}$, for the antiparallel and parallel electron alignment with an external magnetic field (B_0) respectively, as shown in Figure 2.16.

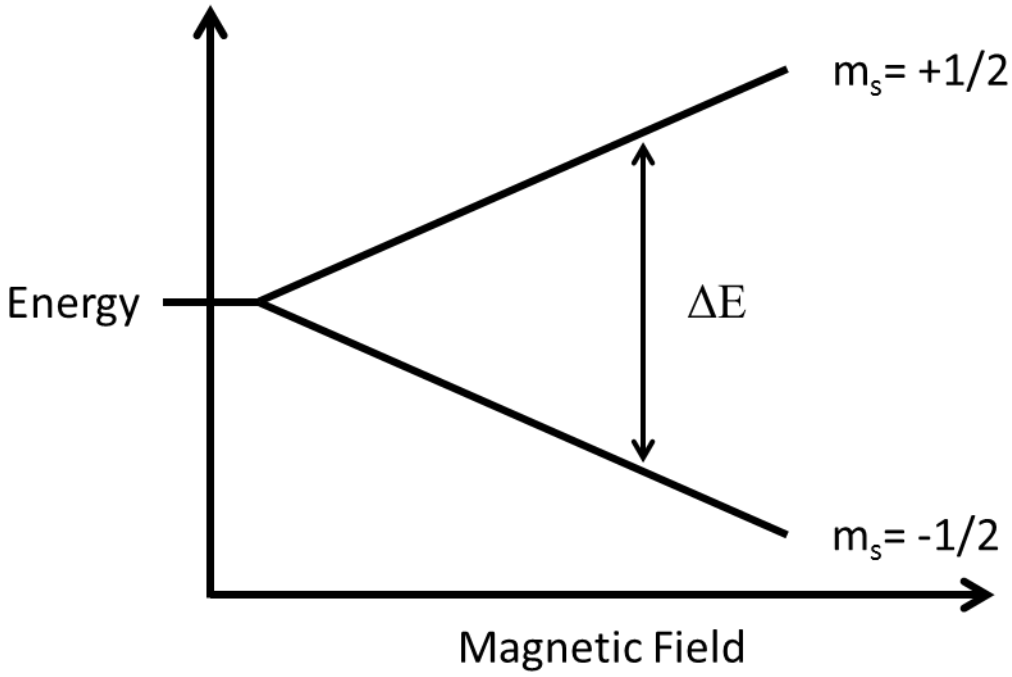

Figure 2.16. Energy level diagram of an electron placed in an external magnetic field (adapted from Reiger).[116]

An electron in an external magnetic field has the degeneracy of the spin energy levels shifted as shown in the spin Hamiltonian in Eq. 2.14.

$$\hat{\mathrm{H}}_g = g\mu_B B\hat{\mathrm{S}}_z \tag{2.14}$$

In this equation, g is the g-value (free electron = 2.0023), μ_B is the Bohr magneton and B is the magnetic field strength (Gauss). The z-component of the spin angular momentum ($\hat{\mathrm{S}}_z$) defined by the magnetic field is also used to determine the spin Hamiltonian. To determine the specific electron spin energy levels, a spin Hamiltonian ($\hat{\mathrm{H}}_g$) is determined for the electron spin eigenfunctions for both $m_s = \pm\frac{1}{2}$, as shown in Eq. 2.15.

$$E_{\pm} = \pm\left(\frac{1}{2}\right) g\mu_B B \tag{2.15}$$

The difference between the two energy levels (ΔE) is described in Eq. 2.16.[116]

$$E = E_+ - E_- = g\mu_B B = h\nu \tag{2.16}$$

The energy differences between these two energy levels in a typical magnetic field are in the range of microwave frequencies (9-10 GHz). Normal EPR spectra are determined by varying the microwave frequency and holding the magnetic field constant. Once again, since there are more electrons in the lower energy state, there will be a net energy absorption, which is monitored.

In this dissertation research, EPR spectroscopy was performed in a Bruker EMX X-band spectrometer with an Oxford variable-temperature cryostat. The acquisition temperature was 110 K, with a microwave frequency of 9.4 GHz, and a microwave power of 1.99 mW. Data was acquired at a modulation frequency of 100 kHz, receiver gain of 30 dB, and modulation amplitude of 1.0 G (with 10 points per modulation amplitude). The sample was prepared by dispersing NCs or aerogels in acetone in a suprasil quartz capillary tube with 4 mm outer diameter and frozen in liquid nitrogen prior to being placed in the instrument.

2.4.5 Electron Microscopy

Electron microscopy is the most common analytical tool for characterizing nanoscale materials and specifically quantum dots. Electron microscopy uses the unique interaction of high energy electrons to give comprehensive information about the nanoscale material. The energy of electrons is based on the principle of conservation of energy from a region where the potential varies from 0 to V_0 is defined by Eq. 2.17.

$$eV_0 = \frac{p^2}{2m} = \frac{h^2}{2m\lambda^2} \tag{2.17}$$

Here p is the electron momentum, which, if the de Broglie relation is used ($p = mv = h/\lambda$) then the equation can be simplified to Eq. 2.18 for the λ of the electron.

$$\lambda = \frac{h}{\sqrt{2meV_0}} \tag{2.18}$$

Due to the high energy relativistic variation for electron mass, a correction is applied using Eq. 2.19.

$$m = m_0/(1 - \frac{v^2}{c^2})^{1/2} \quad (2.19)$$

By plugging this correction into the original Eq. 2.17, the equation for the corrected electron wavelength is given in Eq. 2.20.

$$\lambda = \frac{h}{\sqrt{2m_0 eV_r}} \quad (2.20)$$

The relativistic accelerating voltage, V_r, is based on the microscope accelerating voltage (V_0), Eq. 2.21.

$$V_r = V_0 + \left(\frac{e}{2m_0 c^2}\right) V_0^2 \quad (2.21)$$

These high energy electrons can interact with the specimen in several different ways; the electrons are scattered elastically or inelastically. Rutherford scattering is elastic scattering where the direction of the primary electron beam changes due to the Coulombic interactions between the imposing electrons and the atoms in the specimen, with no energy change of the primary electrons; this can give structural analysis and high resolution images. There are several types of inelastic scattering where the energy of the primary electron beam is lost to the electrons and atoms in the sample. This includes phonon scattering, plasmon scattering or the excitation of a valence electron or inner shell electron in the sample. This excitation in the sample can result in emission of a photon for the outer shell electron called cathodoluminescence. When the electron beam excites an inner shell electron in the sample, the relaxation can emit an X-ray of a characteristic energy. Instead of X-ray emission, an outer shell electron can be ejected which is known as Auger emission. The primary electron beam can also cause the sample to emit X-rays without electron ejection from the inner shell, called Bremsstrahlung. The primary electron beam interacting with the sample also causes the emission of secondary and backscattered electrons (Figure 2.17).

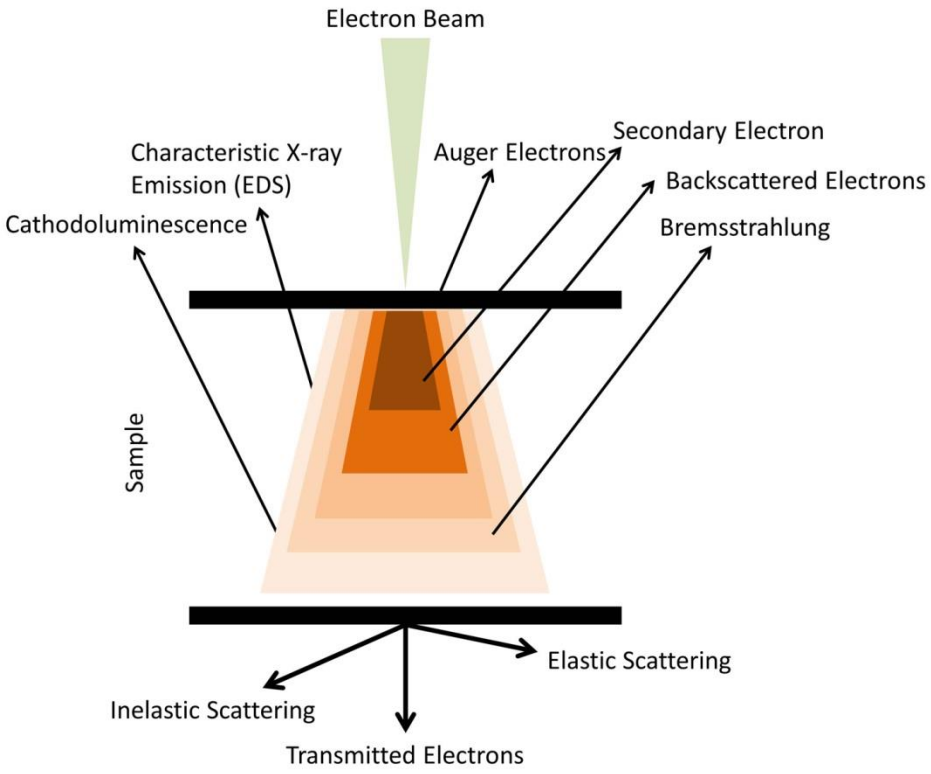

Figure 2.17. Consequences from the interaction of primary electron beam with the specimen (adapted from Goodhew).[117]

2.4.5.1 Transmission Electron Microscopy

A common analytical technique to obtain structure and particle size of nanocrystals, is transmission electron microscopy (TEM), used because of the ability to directly image at high magnifications (50 to 10^6).[117] For TEM instruments, a high energy electron beam is formed in the electron gun (usually either a thermionic gun or field emission gun). The electron gun generates electrons either through thermionic emission or a high electric field (either LaB_6 or W filament). The electrons are accelerated from 40-400 KeV to the anode with a higher potential. [117] The high energy electrons emitted by the electron gun are focused on the sample by the electromagnetic condenser lens system. A side entry double tilt sample holder is used to support a thin grid where the sample has been deposited, into the TEM chamber, which is normally under high vacuum. The electrons transmitted and diffracted from the sample enter the

objective system, and form the first image and the diffraction pattern. Image resolution is determined by the diameter of the objective aperture, with most common TEMs having resolution on the order of nanometer length scale (Figure 2.18).

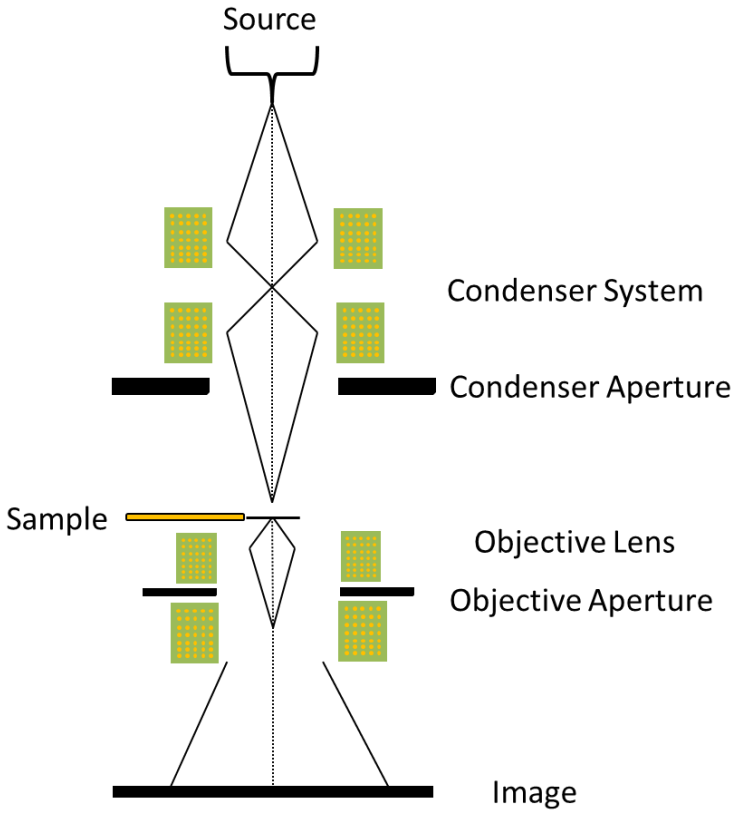

Figure 2.18. Schematic of a conventional TEM instrument (adapted from Goodhew).[117]

The TEM instrument can be operated under two modes. The bright field imaging mode is where the objective aperture allows the transmitted electrons to the detector. The bright field mode is typically used for particle size analysis and shape determination; the projector lenses magnify this image, while a final copy is projected onto a fluorescent screen. In dark field imaging, the objective aperture allows diffracted electrons to pass through, which gives information on the samples lattice parameters and crystallinity.[117]

In this dissertation research the TEM images and measurements were carried out on a JEOL 2010 transmission electron microscope operated at an accelerating voltage of 200 kV using carbon coated Cu

TEM grids as sample supports. Samples were first dispersed in solvent and drops containing the nanoparticles or aerogels dispersed, were placed onto the grids and dried in air.

2.4.5.2 Scanning Electron Microscopy

Scanning electron microscopy (SEM) is normally used to obtain surface and near surface structural information of a sample. Figure 2.19 shows the schematic diagram for a typical SEM instrument. As in the TEM instrument, electrons are generated by an electron gun (most commonly a thermionic gun or field emission gun (FE-SEM)) and are accelerated at lower voltages (1-30 keV).[117] Besides the lower accelerating voltage, the difference between SEM and TEM are the two sets of coils that are used to deflect the beam in order to raster across the surface of the sample in SEM. The image obtained by the rastering in SEM maps the varying intensity of signals as a function of position and acquires the signal gradually to build the image pixel by pixel. Condenser and objective lenses focuses the electron beam into a fine beam onto the sample. The electron beam interacts with the sample, as discussed in section 2.3.5.1. The commercial SEMs utilize both secondary electrons (for surface analysis) detected by an Everhart-Thornley detector, and back scattered electrons (for surface and compositional analysis) detected with either a scintillation detector, a solid-state detector, or a through-the-lens detector in imaging the sample.[117]

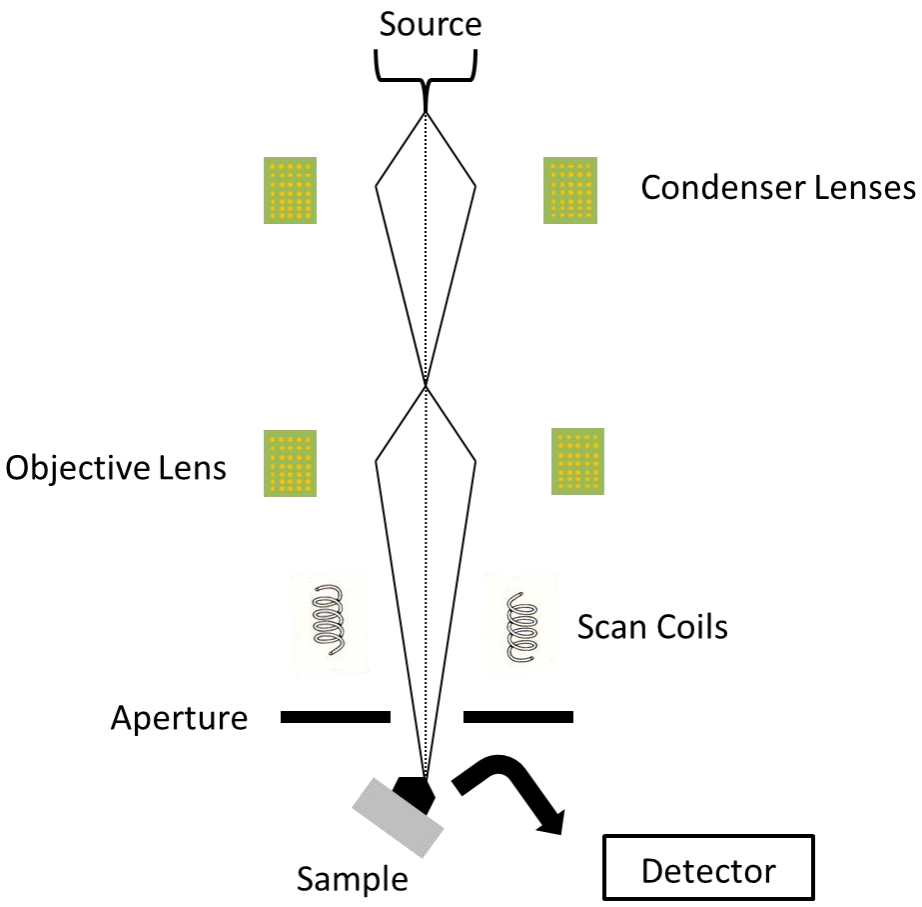

Figure 2.19. Schematic diagram for scanning electron microscopy (adapted from Goodhew).[117]

For this dissertation research the SEM images and lattice planes were obtained using a JEOL JSM-7600F field emission scanning electron microscope. The microscope was operated at an accelerating voltage of 15 kV in the high-vacuum mode.

2.4.5.3 Energy Dispersive X-ray Spectroscopy

As mentioned in section 2.4.5, the collision of high energy electrons with sample atoms will result in the emission of X-ray radiation of characteristic wavelengths for each material. These X-rays can be used to identify the component atoms in a sample and determine their concentration semi-quantitatively. In the ground state, an atom in the sample has electrons in discrete energy levels around the nucleus. When the electron beam excites an inner shell electron, an electron can be ejected from the sample, leaving a

hole; this hole is filled by an outer shell electron while at the same time releasing a characteristic X-ray energy. The transitions that give rise to the X-ray emission are shown in Figure 2.20. The EDS detection system usually has detector crystals such as lithium doped with Si, or germanium, with the detector positioned very close to the sample.[117] One of the drawbacks to this analytical technique is that the lighter elements such as O, C and H, have very low energy peaks that are difficult to detect.

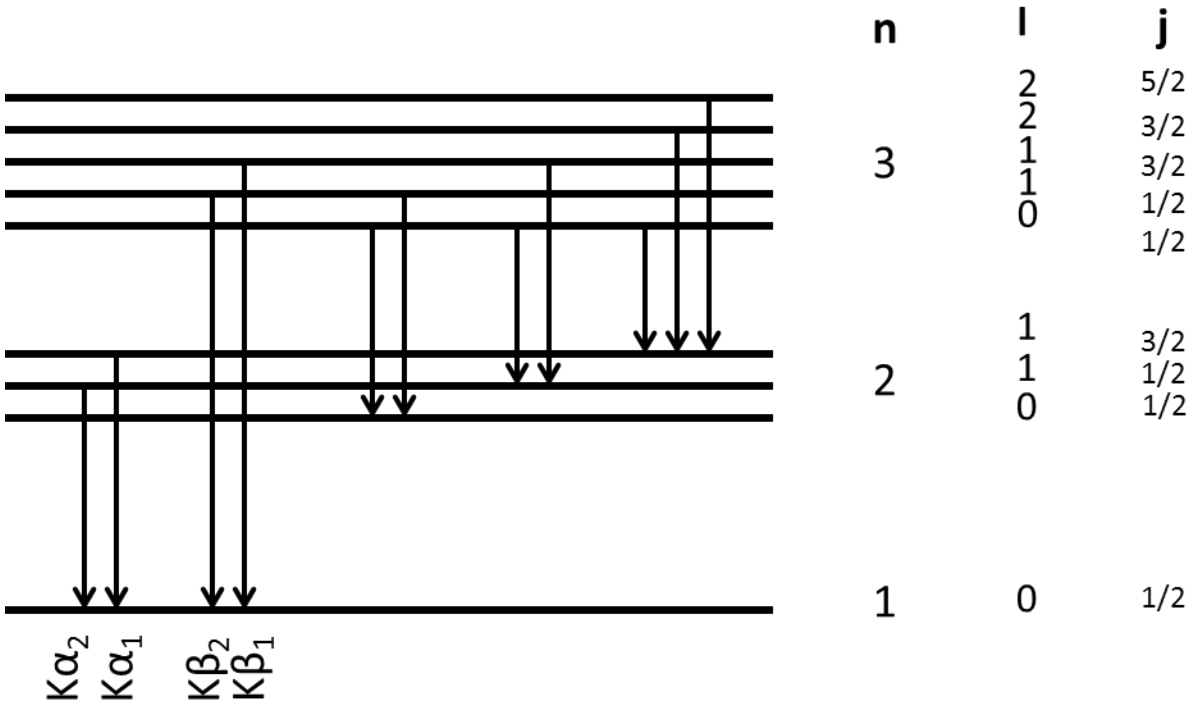

Figure 2.20. Some of the most common X-ray transitions that produce lines in an EDS spectrum.

This dissertation research utilized EDS analysis with EDS detectors (EDAX inc.) coupled to both TEM (JEOL 2010 transmission electron microscope) and FESEM (JEOL JSM-600F field emission scanning electron microscope) instruments.

2.4.6 Optical Spectroscopy

Optical spectroscopy is defined as the study of the interaction of light (ultra-violet, visible and infrared) with matter, this interaction results in absorption and emission of light. This can provide important structural, bandgap and concentration information for a nanomaterial.

2.4.6.1 UV-Visible Absorption Spectroscopy

The bandgap of many common semiconducting quantum dots falls within the energy range of ultra-violet/visible light (300-800 nm). This makes UV-visible absorption spectroscopy an ideal tool for characterizing these materials. UV-vis spectroscopy is based on the principle that visible and/or ultraviolet light is absorbed by the sample causing electronic transitions due to the absorption of these photons. The absorbance of a material (A) is shown in Eq. 2.22.

$$A = \log\left(\frac{I_0}{I}\right) = -\log T \tag{2.22}$$

This equation compares the intensity of the incident light (I_0) to the intensity of the light that is transmitted (I) through the sample, which can be compared to the total transmittance (T) of the light through the material. The detector collects the light that is transmitted through the sample, and it is digitized to give an absorption spectrum. The absorption spectrum can be used to determine the concentration of a material with a known extinction coefficient, ε, through the Beer-Lambert law in Eq. 2.23.

$$A = \varepsilon l c \tag{2.23}$$

In this equation, ε is the extinction coefficient of the material, which is a parameter to define how much light a material absorbs on a per mole basis at the wavelength of maximum intensity, l is the path length of the solution and c is the molar sample concentration. For semiconducting quantum dots, the electronic transition seen in UV-Vis spectroscopy occurs from the valence band to the conduction band, corresponding to the bandgap, as discussed in Chapter 1 Section 1.2. Accordingly, UV-visible absorption spectroscopy is useful for determining the NC size based on the bandgap (E^*) using the effective mass approximation model Eq. (2.24).

$$E^* \cong E_g + \frac{\hbar^2\pi^2}{2r^2}\left(\frac{1}{m_e} + \frac{1}{m_h}\right) - \frac{1.8e^2}{\epsilon r} \tag{2.24}$$

In Eq. 2.24, $E_g$is the bandgap for the bulk material, and r is the radius of the semiconductor NCs, m_e is the effective mass of the electron, m_h is the effective mass of the hole and ϵ is the dielectric constant of the semiconductor.[118]

In this dissertation research the UV-visible spectroscopic measurements were performed on a Shimadzu UV-1800 spectrometer in a quartz cuvette.

2.4.6.2 Diffuse-Reflectance Spectroscopy

One method used to determine the bandgap of solids and powders is by diffuse reflectance spectroscopy. Due to the fact that light cannot penetrate opaque samples, it is reflected from the surface of the powder sample. When light hits the powder sample, it is reflected in all directions as shown in Figure 2.21. A portion of the light is refracted as it enters the powder, and is scattered due to internal reflection. Diffuse reflection is the reflection of light from the sample surface at all angles from the incident light ray, and is therefore unlike specular reflection, where reflection occurs at one angle from the incident light angle. An ideal diffuse reflection surface will have equal reflected luminance in all directions. The principle of this analytical technique is that as the diffuse reflected light is reflected from the solid powder sample, some of the reflected light will be weaker as the powder sample absorbs the incident light at a characteristic wavelength. In the energy range that the powder sample strongly absorbs the incident light, only the diffuse reflected light from short light paths is emitted. This causes the main difference between the relative intensity of the peaks in the transmission spectrum and the diffuse-reflectance spectrum, where peaks that are weak in the transmission spectrum are stronger in the diffuse-reflectance spectrum.[119]

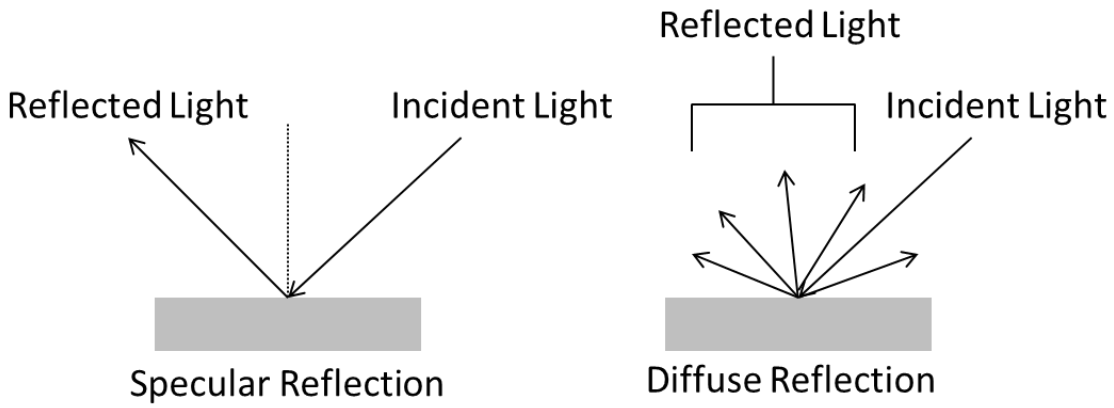

Figure 2.21. Comparison of specular reflection and diffuse reflection.

The Kubelka-Munk theory is used to model the reflected and transmitted spectrum of a colored solid material based on the scattering and absorption function.[119] The Kubelka-Munk theory started as a model to explain light propagation in parallel colorant layers.[120] Starting with a horizontal colorant layer, any incident light traveling parallel to the boundaries of this layer are only considered if they are at the edge of that layer. The flux of light traveling in any direction is separated into its vertical and horizontal component and only the vertical component is considered in the calculation.[121] A thin section of the sample with a thickness dx is considered at a distance x from the illuminated surface of the material, where the total sample thickness is d (Figure 2.22). After scattering and absorption, only two intensities of light, I and J, travel upwards and downwards through the thickness dx. The limiting factor of the light absorption per unit of thickness is defined as the value K, and S is the scattering coefficient equal to the limiting fraction of light energy scattered backwards per unit thickness which tends towards zero.[121]

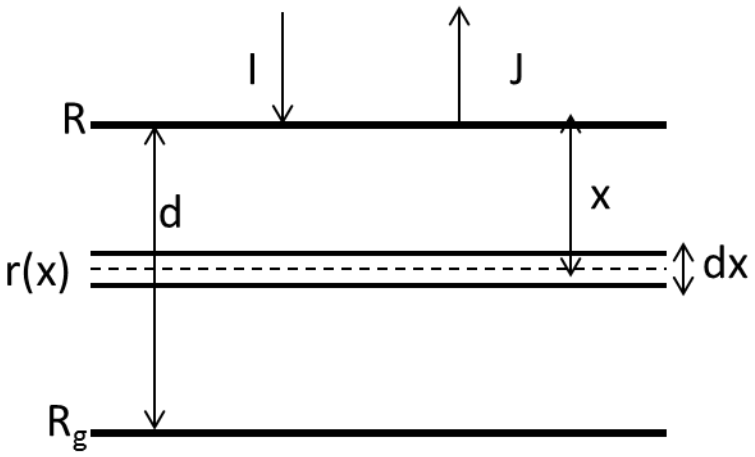

Figure 2.22. Schematic of the reflectance and transmittance of a solid layer (adapted from Nobbs).[122]

The downward flux intensity is decreased by $J\ (S\ +\ K)dx$ (absorption and scattering) and increased by $I\ Sdx$, whereas in the reverse the upward flux is decreased by $I\ (S\ +\ K)dx$ and increased by $J\ Sdx$. The total net change in each flux component can be obtained by adding the energy lost and gained as the flux goes through the thin section dx which can be conveyed in Eq. 2.25 and 2.26.

$$dI = -(S + K)Idx + JSdx \tag{2.25}$$

$$-dJ = -(S + K)Jdx + ISdx \tag{2.26}$$

In Eq. 2.26, the negative sign in front of the equation indicates that the direction of the J flux is opposite to that of x. The two differential equations obtained when each of these equations is divided by dx are shown in Eq. 2.27 and Eq. 2.28.

$$\frac{dI}{dx} = -(S + K)I + JS \tag{2.27}$$

$$\frac{dJ}{dx} = -SI + (S + K)J \tag{2.28}$$

The reflectance ratio (r_x) in Eq. 2.29 is the ratio of the upward to the downward flux at the point x from the top of the surface layer.

$$r_x = \frac{J}{I} \tag{2.29}$$

Taking the differential of Eq. 2.26 with respect to x, gives the change in r_x with the position in the layer, Eq. 2.30.

$$\frac{dr_x}{dx} = \frac{\left(I\left(\frac{dJ}{dx}\right) - J\left(\frac{dI}{dx}\right)\right)}{I^2} \tag{2.30}$$

By plugging in the equation for $\frac{dJ}{dx}$ and $\frac{dI}{dx}$ (Eq. 2.27 and 2.28) into Eq. 2.30, Eq. 2.31 is obtained.

$$\frac{dr_x}{dx} = -Sr_x^2 + 2(K+S)r_x - S \tag{2.31}$$

As the thickness of the sample becomes infinitely thicker, there is no appreciable increase in the reflectance, so there will be no change in the reflectance ratio (r_x) with x, where now r_x would be R_∞ in Eq. 2.32.

$$\frac{dr_x}{dx} = 0 = -SR_\infty^2 + 2(K+S)R_\infty - S \tag{2.32}$$

The quadratic equation in Eq. 2.29 can be rearranged and solved to give Eq. 2.33.

$$R_\infty = 1 + \frac{K}{S} - \left[\left(1 + \frac{K}{S}\right)^2 - 1\right]^{1/2} \tag{2.33}$$

Finally, the equation can be reduced to the more common Kubelka-munk approximation Eq. 2.34.

$$\frac{K}{S} = \frac{(1-R_\infty)^2}{2R_\infty} \tag{2.34}$$

This shows that the reflectance of an opaque layer depends on the ratio of K (absorption coefficient) to S (scattering coefficient) and not the individual values.[121]

For this dissertation research, diffuse-reflectance measurements were performed on a JASCO V-570 UV/VIS/NIR Spectrometer with integrating sphere. The solid samples were mixed with barium sulfate before being placed in the JASCO powder sample holder.

2.4.6.3 Fourier Transform Infrared Spectroscopy

Fourier transform infrared spectroscopy (FTIR) is used to probe vibrational excitations of molecules, and specifically functional groups in the molecules. In FTIR spectroscopy, infrared radiation is transmitted

through a sample and radiation of a specific wavelength (for the vibrational energy) is absorbed, and the resulting transmittance is measured.

The basic components of an FTIR instrument are pictured in Figure 2.23, where a source generates the infrared radiation that is passed through an interferometer and then the sample. The transmitted signal is captured, amplified and then converted to a digital signal by the detector, amplifier, and analog-to-digital converter. The data is Fourier transformed to give the final infrared spectrum that shows the transmitted intensities for each frequency. [123]

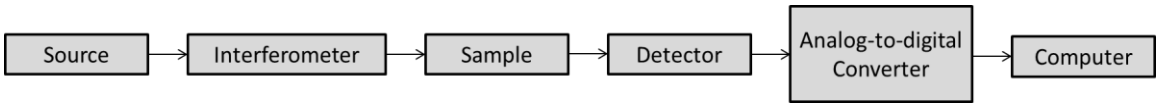

Figure 2.23. Schematic of an FTIR spectrometer (adapted from Stuart). [123]

For this dissertation research, powdered samples were measured using a Shimadzu IR Affinity-1 FT-IR spectrometer with a MIRacle10 attenuated total reflectance accessory with a monolithic diamond stage and pressure clamp, using the IRsolution software.

2.4.6.4 Photoluminescence Spectroscopy

In photoluminescence (PL) spectroscopy, electromagnetic radiation is used to irradiate a sample to excite an electron to higher electronic states. The emission released during the relaxation of excited states is measured as shown in Figure 2.24. The light generated by the excitation source passes through the sample, where light at a specific wavelength is absorbed by the sample, and light is emitted into a detector at 90° from the source. This is then converted into an electric signal by the detector and processed by the electronic devices. Finally a plot of intensity as a function of wavelength of the light is produced.

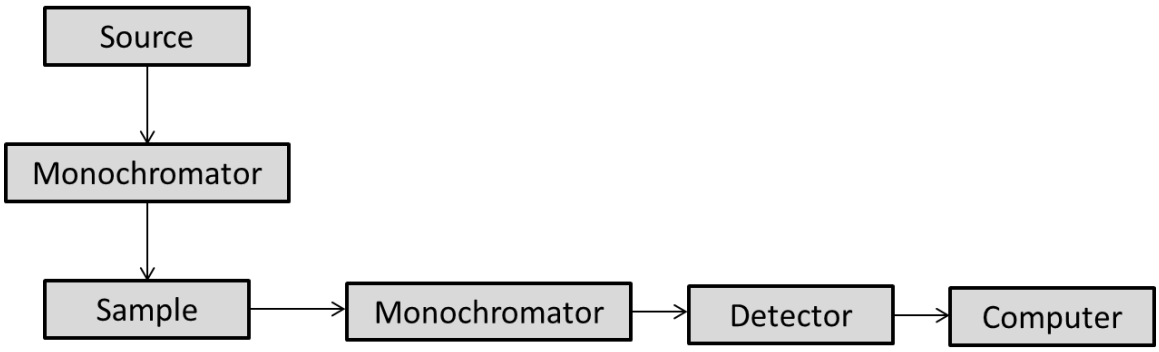

Figure 2.24. Schematic diagram of a photoluminescence spectroscopy instrument (adapted from Lakowicz).[124]

The typical molecular emissions measured in photoluminescence spectroscopy are shown in the Jablonski diagram in Figure 2.25. Once the sample absorbs a photon and excites an electron from singlet ground state, S_0, to a higher molecular vibrational level such as the singlet first, S_1, or second, S_2, state there are several paths for the electron. Available paths include relaxing back to a lower vibrational energy level, S_1, which is called internal conversion. Another path is the fluorescence emission, which happens upon the relaxation of the electron from the lowest vibrational level in the S_1 state to a vibrational level of the S_0 vibrational energy state. A third option for an excited electron is undergoing a spin conversion to the triplet state, T_1, called intersystem crossing. This is called phosphorescence and it is a transition from the T_1 state to the lower S_0 state, with slow emission since it is a spin-forbidden transition.[124]

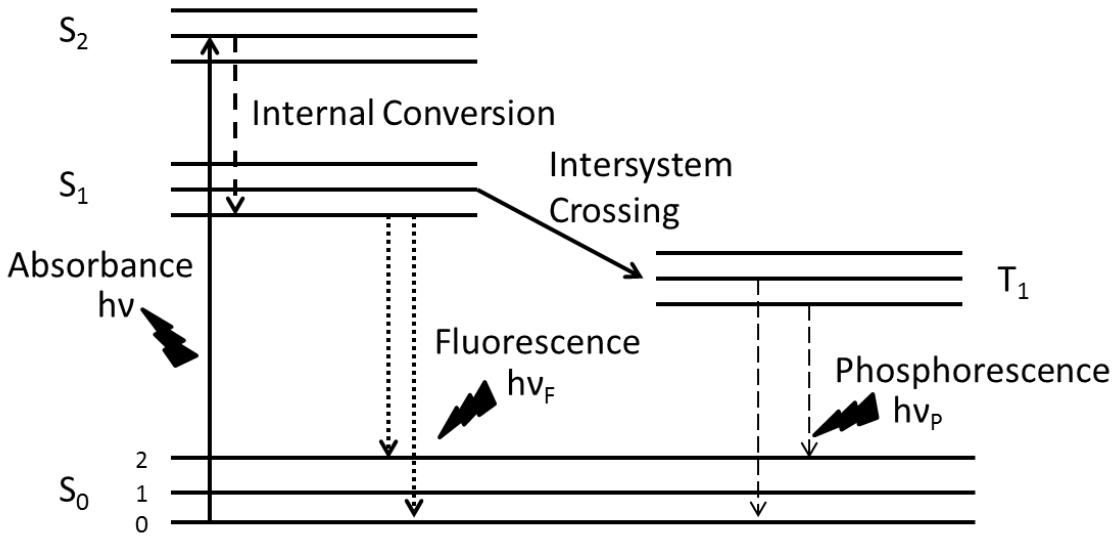

Figure 2.25. The Jablonski diagram highlighting the absorption and emission of light from a molecule (adapted from Lakowicz). [124]

Alternatively, for PL emission in QDs, the sample absorbs light leading to an electron being excited from the valence to the conduction band. When the electron resumes its ground state, energy can be emitted as light, or fluorescence. In a perfect QD model the energy of photon emission would be equal to the band gap energy (E_g) from the valence band and the conduction band. However sometimes anomalous features in PL spectra of colloidal QDs can be observed. Figure 2.26 shows the PL emission from a bare-QD and a QD with surface passivation. These surface trap states can cause broadening in the PL emission or surface state emission. These trap states can lower the quantum yield of the QD samples.[125]

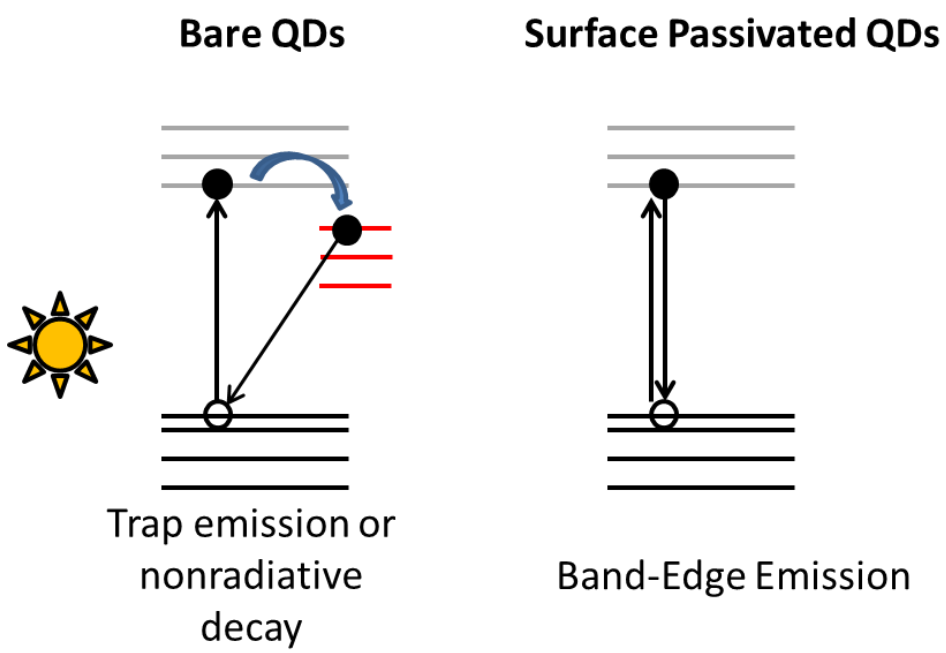

Figure 2.26. Schematics on the effect of surface states on the PL emission recombination process (reproduced from Char).[125]

For this dissertation research the photoluminescence spectra of specimen dispersed in solution was determined using a Cary Eclipse (Varian, Inc.) fluorescence spectrometer using a quartz cuvette. Solid samples were dispersed in solvent and sonicated prior to being placed in the instrument.

2.4.7 X-ray Photoelectron Spectroscopy

A surface specific analytical technique, X-ray photoelectron spectroscopy (XPS) is used to measure the elemental composition (even at low concentrations), the empirical formula, and the chemical and electronic state of the elements in the sample. XPS is performed by irradiation of the sample with monoenergetic soft X-rays and recording the kinetic energy and number of electrons emitted from the sample, Figure 2.27. The sample chamber is under ultra-high vacuum (10^{-9} millibar) for the data collection. The source X-rays only penetrate 1-10 μm into the sample depth, and emitted electrons have kinetic energy according to Eq. 2.35.[126]

$$KE = h\nu - BE - \phi_s \tag{2.35}$$

For Eq. 2.35, the binding energy of the electron in the atomic orbital (BE) and the spectrometer work function (ϕ_s) are subtracted from the energy of the photon to give the kinetic energy (KE). The Fermi level is considered the zero binding energy level. Each element in a sample has a unique set of binding energies in XPS spectra that can identify the chemical shifts, which give information on the chemical state, chemical potential and polarizability.[126]

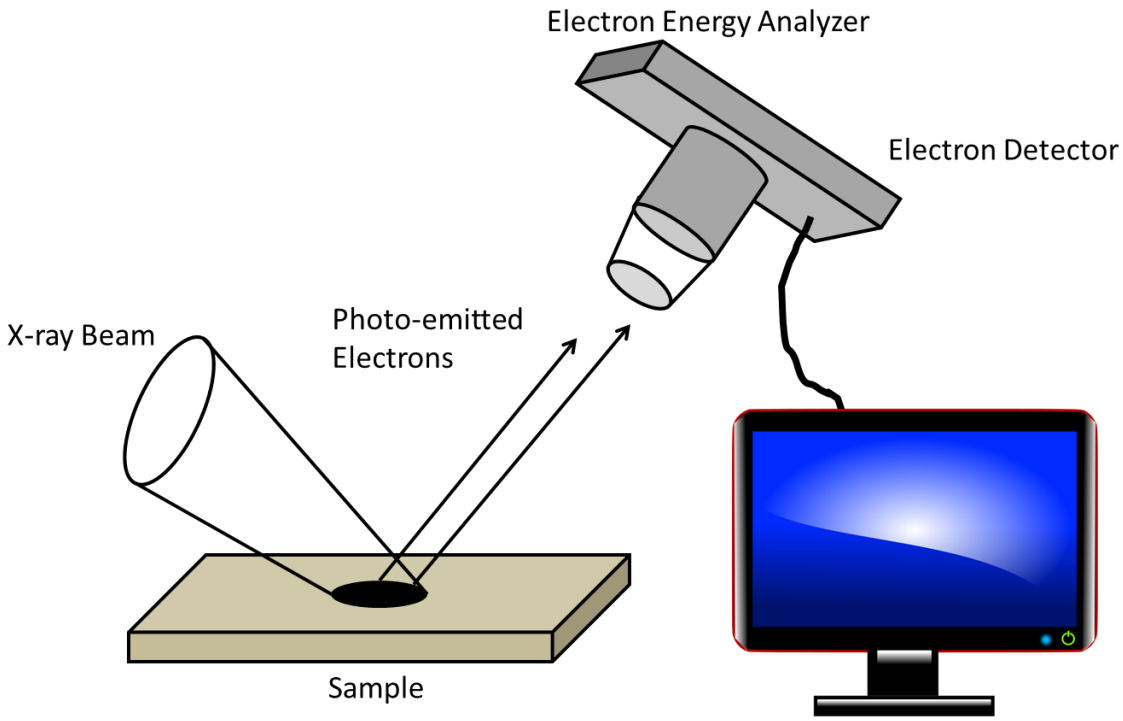

Figure 2.27. Schematic diagram for an X-Ray Photoelectron Spectroscopy instrument (adapted from Walls).[126]

The main components of an XPS instrument include an X-ray source, extraction optics and a detector. It is important that the X-ray source emit x-rays that are monochromatic; the most common source for XPS is achieved by using a high energy electron beam directed at a metal, commonly Al, which is called the X-ray anode. The high energy electron beam ejects an Al 1s electron, the hole is filled by a 2p electron, and an X-ray is released.[127]

For this dissertation, XPS measurements were performed with a Kratos Axis Ultra XPS with a monochromatic Al Kα X-ray source in spectrum mode at 10 mA and 15 kV. A low energy electron flood gun was used for charge neutralization of nonconducting samples. The pressure in the analytical chamber during spectral acquisition was approximately 1×10^{-9} Torr. The pass energy for survey spectra was 160 eV, and the pass energy for high-resolution scans was 20 eV. The binding energy scales were calibrated based on the most intense C 1s high-resolution peak binding energy. The solid powder sample was put on tape before being introduced into the instrument.

CHAPTER 3: POROUS SILICON BASED DEVICES WITH ANION PASSIVATED LEAD SULFIDE QUANTUM DOTS (QD) FOR RADIATION DETECTION

3.1 Introduction

Direct conversion radiation detectors produce an electrical signal through the direct interaction with incoming radiation. Once an electrical bias is applied to the detector, the photon interacts with the semiconducting device to produce an electron-hole pair. Direct conversion radiation detectors are capable of improved energy and spatial resolution, but the trade-off is reduced detection efficiency.[128] For direct conversion devices, detection efficiency is proportional to the fifth power of the effective atomic number. So, a device based on a semiconducting material with a high effective atomic number $Z_{eff,}$ (Eq. 3.1) would have potential as efficient direct-conversion radiation detectors.

$$Z_{eff} = \sqrt[2.94]{f_{n_1} \times \left(Z_{n_1}\right)^{2.94} + f_{n_2} \times \left(Z_{n_2}\right)^{2.94}} \tag{3.1}$$

In Eq. 3.1, f_n is the fraction of the total number of electrons from each element in the material, and Z_n is the atomic number of each element in the material.[129] Examples of semiconductors with high effective atomic number, and the relative dose requirements (normalizing to $LaBr_3$= 100%) are shown in Table 3.1. The use of materials such as lead sulfide quantum dots with an effective atomic number of Z=77, would, as seen in Table 3.1, decrease the dosage required to collect a proper image using radiologic diagnostic equipment.[130]

Table 3.1. Effective atomic number and relative dose requirements for materials used in direct conversion X-ray detection devices.

Material	Effective Atomic Number	Relative Dose Requirement
Lanthanum Bromide	47	100%
Cadmium zinc telluride	48	95%
Cadmium telluride	50	86%
Lutetium yttrium orthosilicate	66	43%
Lead sulfide	77	29%

To make devices useful for direct radiation detection, a thick active layer will be needed to stop the high energy radiation in medical devices. Therefore, a novel approach was proposed using a thick (10-12 µm) porous silicon matrix as the n-type material and support for the p-type lead sulfide quantum dots, which should be able to stop higher energy radiation (e.g., 4.4 MeV) due to the total thickness of the Si wafer being 375 µm, as well as improve charge transport properties, which can be an issue with these passivated quantum dots. The combination of lead sulfide quantum dots and machined porous silicon resulted in devices as shown schematically in Figure 3.1. The final constructed device contains electrodes at the top and the bottom faces, and a reverse bias is applied to the electrodes. This will cause depletion in the semiconductor material as electrons and holes are collected at the electrodes.[89]

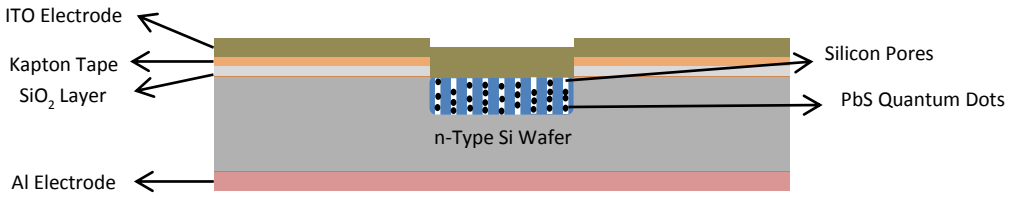

Figure 3.1. Final device showing the machined pores in the n-type silicon support.

Solution-phase lead sulfide (PbS) colloidal quantum dots are passivated with a long chain organic ligand such as oleic acid. These long chain passivating ligands make an insulating layer between nanocrystals that inhibits charge transport.[26] Colloidal quantum dot films have been synthesized using a variety of short chain mono- and bidentate organic ligand capping agents, including short alkylthiols, aromatic thiols, alkylamines, and mercaptopropionic acid, which have all shown promise in achieving effective passivation while reducing interparticle spacing, thus promoting charge transport in the system.[14-15, 131-135] Previous work in our group focused on machining pores in the silicon support and drop-casting oleate-capped PbS quantum dots for X-ray detection device preparation.[20, 77] The focus of the present work is to utilize anion-passivated PbS quantum dots with shorter chain thiolate ligands to increase charge transport in our devices.

3.2 Experimental Methods

All the chemicals used in the syntheses described in this chapter are listed in Chapter 2. Transmission electron microscopy (TEM), UV vis spectroscopy, powder X-ray diffraction (PXRD), scanning electron microscopy (SEM) and energy dispersive X-ray spectroscopy, as described in Chapter 2, were utilized for characterization of the constituent materials and I-V curves were performed as described in Chapter 2.

3.2.1 Synthesis of Anion-Passivated PbS Quantum Dots and Ligand Exchange with 4-fluorothiophenolate

The PbS quantum dots employed in the experiment were synthesized following solution-phase methods under inert atmosphere conditions using Schlenk line techniques.[26, 131] In a typical synthesis, 2 mmol of Pb(II)O is combined with 18.25 ml octadecene and 1.75 ml oleic acid and the sample is stirred under Ar at 110° C until a clear Pb-oleate solution forms. This is followed by an injection of 1 mmol of hexamethyldisilathiane in 10 ml octadecene to form the PbS QDs. A solution of 1.6 mM $CdCl_2$/tetradecylphosphonic acid solution in oleylamine was injected into the oleate capped PbS QDs and stirred over-night to make anion-passivated QDs. Oleate-capped PbS QDs were isolated by precipitation with acetone and centrifugation. Oleate-capped PbS QDs were redissolved in hexane to 50 mg/ml. The ligand exchange was performed by adding a 10 ml solution of acetone, 20 mmol 4-fluorothiophenol and 20 mmol trimethylamine. The sample was precipitated with n-pentane and redissolved in acetone to 50 mg/ml.

3.2.2 Deposition of Anion-Passivated Oleate-Capped and 4-fluorothiophenolate-Capped PbS QDs

The PbS QDs were spin-coated onto the pSi surface starting with a solution of oleate-capped (4-fluorothiophenolate-capped) anion-passivated PbS QDs in hexane (acetone) at 50 mg/ml using a Spin Coater Model P6700 series at 2500 rpm for 15 second intervals. Each device was supplied with 20 layers of 1 ml/layer PbS quantum dots. Between layers of PbS quantum dots, the samples were washed with methanol (n-pentane).

3.2.3 Mercaptopropionoic Acid Ligand Exchange on PbS

The porous silicon sample was initially spin coated with 20 layers of a 50 mg/ml oleate-capped PbS QD solution, followed by a 1% mercaptopropionic acid (MPA) solution. The sample was then washed with methanol to remove excess ligands. This was repeated until a desired thickness of QDs was achieved.

3.2.4 Device Fabrication

Following the addition of PbS quantum dots into the pores of the pSi sample, each sample was coated with Kapton tape; the Kapton tape was used in an attempt to decrease the dark current, caused by shorts in the device. Shorts were likely produced during the anodic etching of the silicon wafer. The tape is to replace the SiO_2 passivation layer that could have been destroyed in the anodic etch process.

Al and ITO thin films were deposited as described in Section 2.3.2, by evaporative deposition or RF sputtering, respectively, to form the electrodes on either side of the devices.

3.3 Results and Discussions

Near-IR-absorbing anion-passivated PbS QDs were synthesized according to literature methods with slight modifications.[14] As-prepared anion-passivated PbS QDs were purified by two cycles of dispersion in hexane and precipitation with acetone and then exchanged in the solution phase with 4-fluorothiophenol or after film-deposition with mercaptopropionic acid. Figure 3.2 shows a high-resolution TEM image of the oleate-capped anion-passivated PbS QDs, with the insert showing the particle size analysis. According to the TEM images, the particle size for the anion passivated PbS quantum dots was 5.0±0.4 nm (N=90).

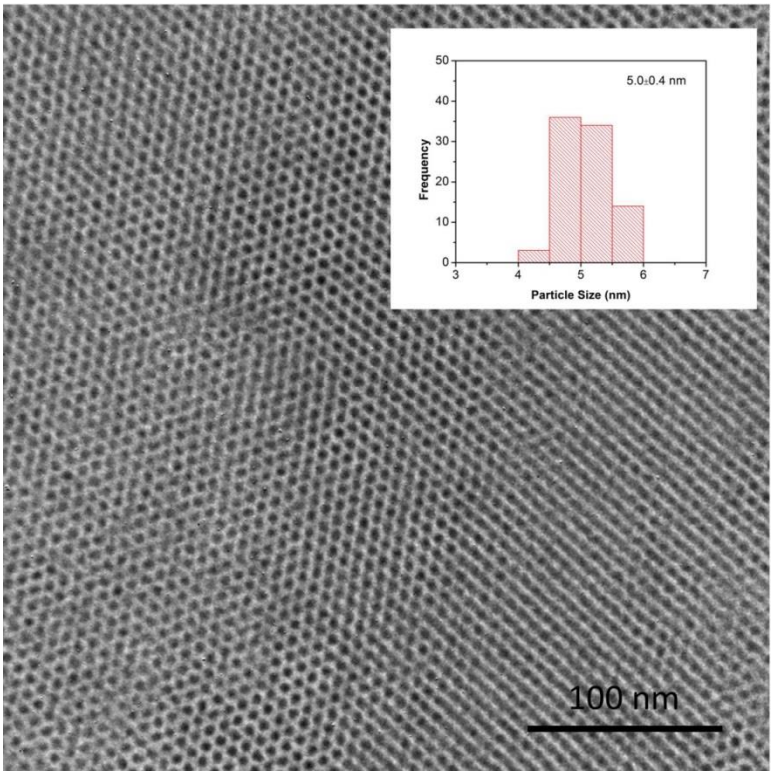

Figure 3.2. TEM images for the PbS quantum dots: the inset is the particle size analysis.

The EDS spectrum in Figure 3.3 shows the presence of Cd in the sample, with the unlabeled peaks correlating to Cu in the TEM grid. This Cd is presumed to form a surface passivating layer for the dangling anions on the particle surface to improve charge transport in the lead sulfide quantum dots, as previously reported.[131]

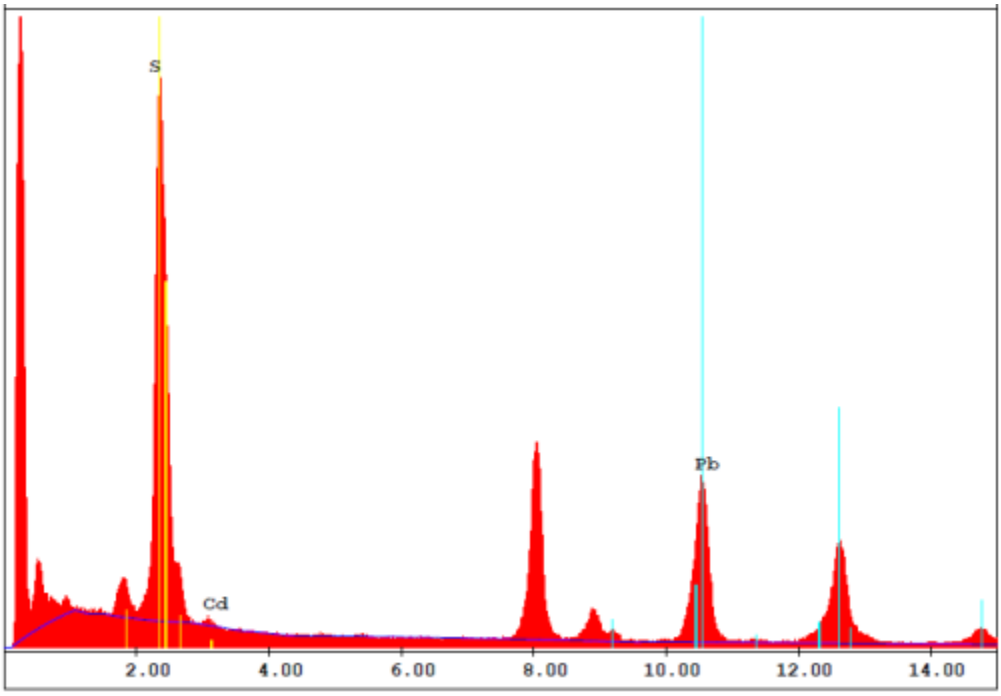

Figure 3.3. The EDS spectra for the anion-passivated PbS QDs showing the presence of Cd.

The structural characteristics of lead sulfide quantum dots were determined by powder X-ray diffraction (PXRD) performed on a Bruker D2 Phaser using the Kα line of a Cu anode source with 30 kV and 10 mA. Figure 3.4 shows the PXRD pattern for the anion-passivated lead sulfide quantum dots, showing they crystallize in the cubic phase, with an absence of peaks for any other material.

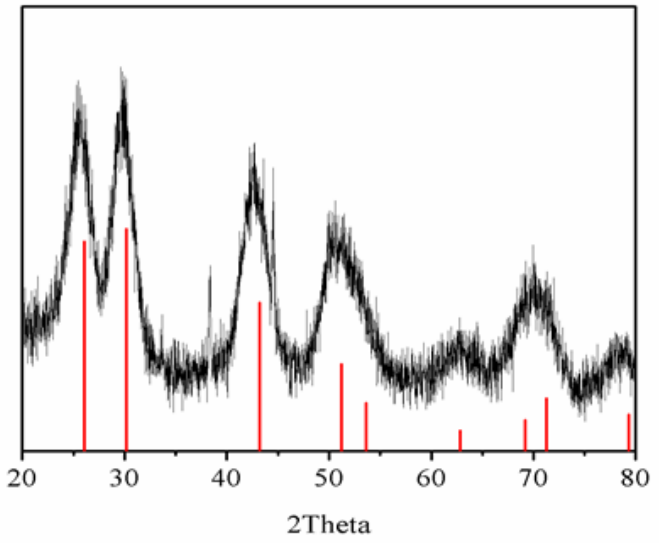

Figure 3.4. The PXRD pattern for anion-passivated cubic lead sulfide quantum dots, with the red lines corresponding to the powder diffraction file pdf #005-0592 for cubic lead sulfide.

The UV-Visible spectrum of the PbS samples show an absorption peak, as expected, at 825 nm in the near-IR region, and PL emission at 915 nm for the PbS quantum dots dispersed in hexane (Figure 3.5).

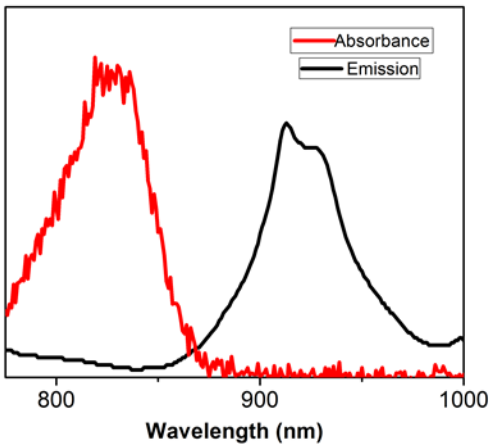

Figure 3.5. UV-visible absorbance spectra and PL emissions, for anion-passivated PbS QDs.

Scanning electron microscopy (SEM) of the pSi supports indicates pore depths of 10-15 µm, and pore diameters between 80-100 nm were achieved with the as-developed anodic etching process, as shown in Figure 3.6.

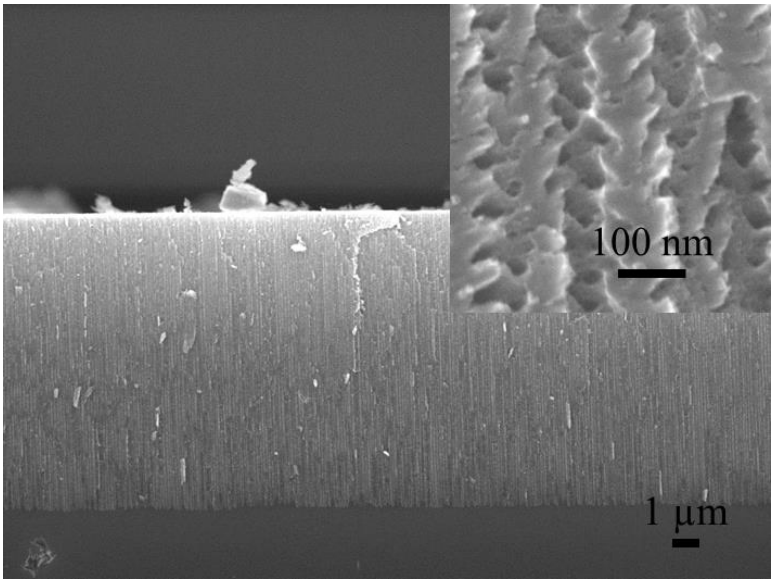

Figure 3.6. SEM images of the anodized n-type silicon wafer prior to addition of PbS QDs.

Following the spin-coating of the oleate-capped PbS QDs onto the pSi support, the SEM image (Figure 3.7a) along with EDS mapping of Pb (green line) and Si (red line) (Figure 3.7b) show Pb throughout the pores of the sample. Unfortunately they also show a gradient of Pb from the top to the bottom of the pores in the Si wafer, which indicates that although there was some infiltration of PbS QDs into the pores there is also clearly a thick layer of PbS on top of the device, which could have detrimental effects on device performance.

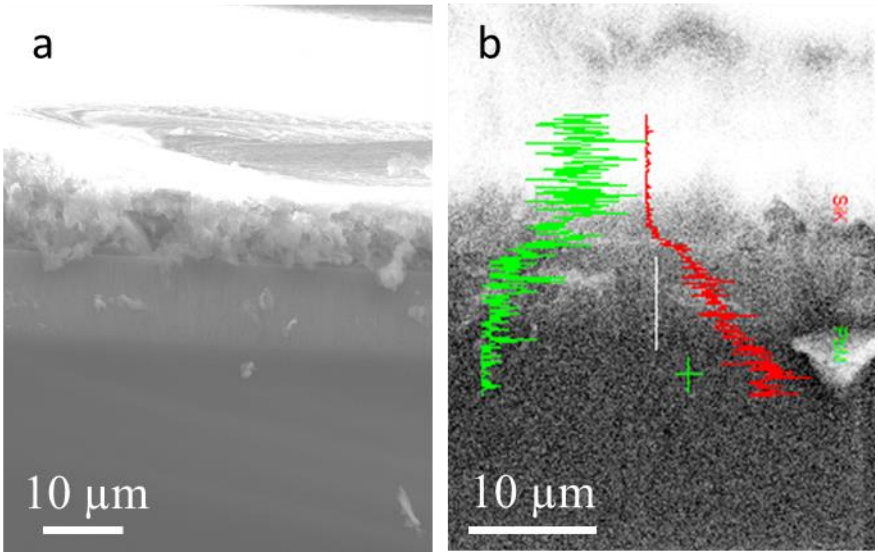

Figure 3.7. The a) SEM micrograph and b) EDS Mapping for pSi after addition of oleate-capped PbS QDs.

3.3.1 Probing the Effect of the Anion-Passivated PbS QDs on the Standard I-V Curves for Completed Devices

To verify the charge transport properties of these devices a response to visible radiation (in addition to infrared), is expected based on the band gap of the PbS quantum dots employed. This photodetector response is the initial test to determine if the devices would be suitable for radiation detection. The first step in testing these devices was to measure the detector response to white light (white-LED flashlight) as a function of bias, and look for a strong dependence on the illumination, especially in the forward bias condition.

The I-V curves for the completed devices were determined using a Keithley 236 Source Measurement unit. Samples were measured under dark conditions and visible radiation as a measure to determine initial device performance prior to testing with high energy radiation. Each sample was measured with a forward and reverse applied bias. Figure 3.8 shows the standard curve of a device without the addition of PbS quantum dots. This standard graph of the detector current versus applied voltage for the device devoid

of quantum dots shows a resistor-like response, with a straight line in the measured current density as the applied bias is adjusted.

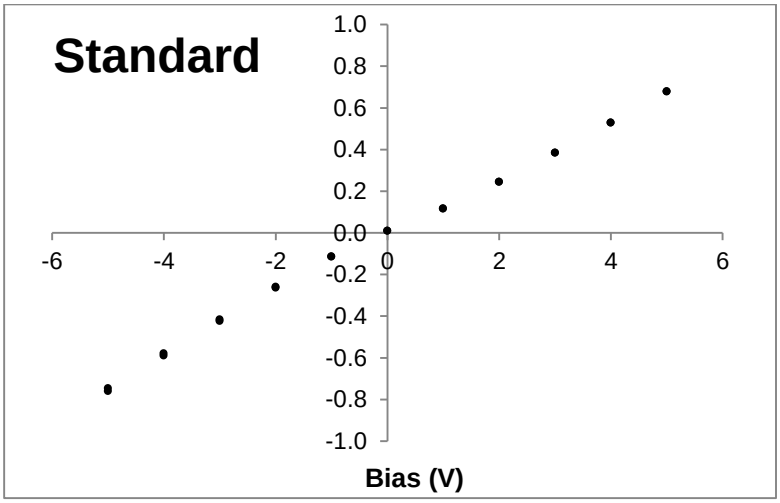

Figure 3.8. Detector current vs. applied voltage under illumination for a device containing no lead sulfide quantum dots.

The samples with the long chain insulating oleate ligand which were spin-coated showed similar graphs of detector current versus applied voltage as the standard upon irradiation with the white LED light source, suggesting that these devices are also resistor-like (Figure 3.9). This means that these devices have poor charge transport properties, and would not be suitable for radiation detection devices.

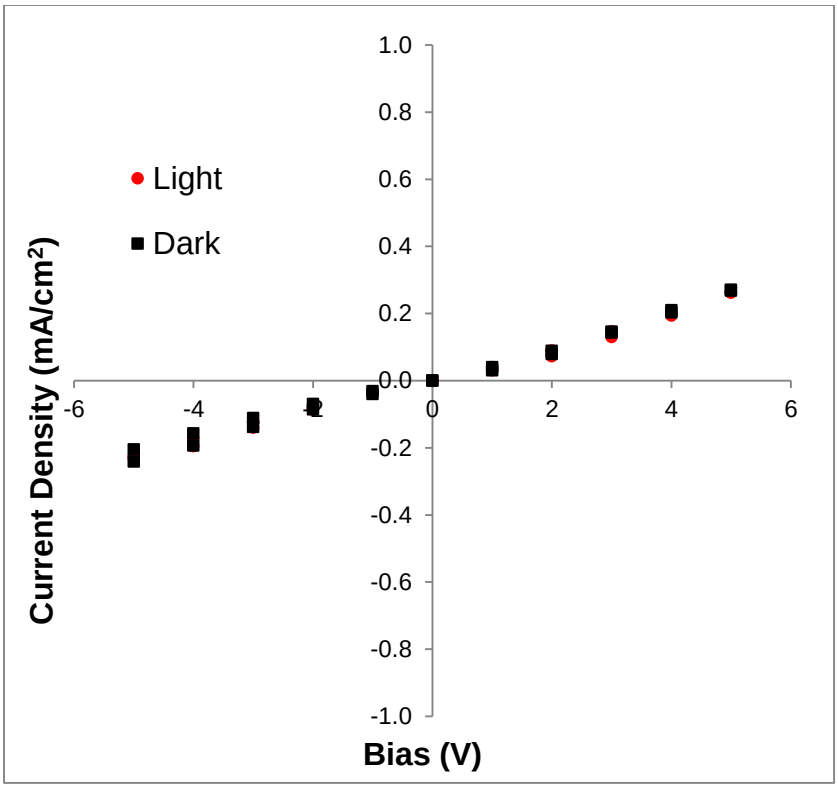

Figure 3.9. Detector current vs. applied voltage in the dark and under illumination for a device with oleate-capped anion-passivated PbS QDs.

The device samples where the long chain insulating oleate ligand were exchanged with mercaptopropionic acid post-deposition, measuring the current output with a change in applied voltage, revealed non-linear I-V curves. This would make the devices closer to a photodetector (Figure 3.10). These devices also highlight the lack of reproducibility seen in the samples, where upon illumination (forward and reverse bias) the sample shows a decrease in the current density with an increase in the applied bias. This could be due to a change over-time in the sample with the applied bias; it is impossible to tell if this is a light-effect or a current affect in the device.

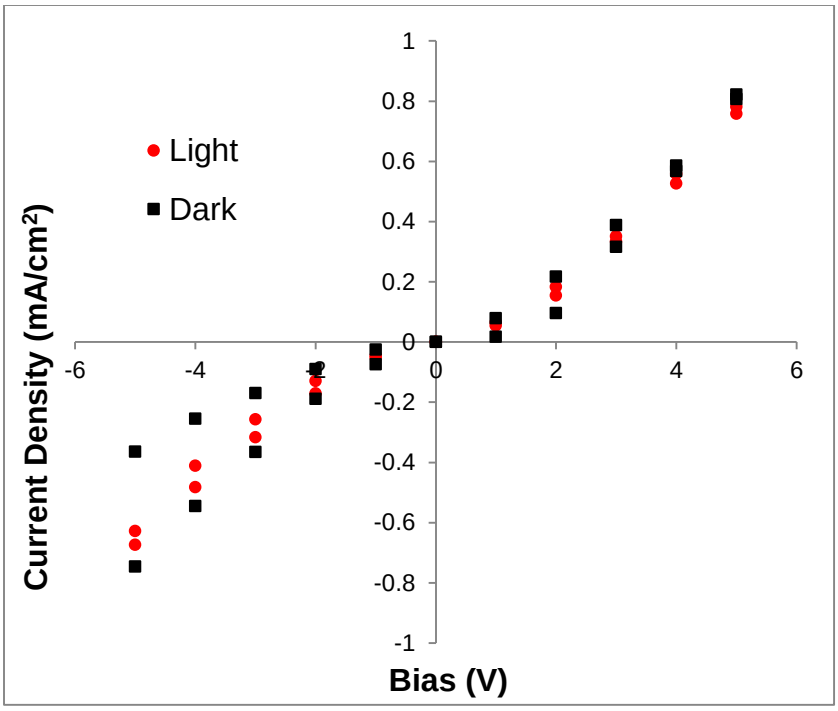

Figure 3.10. Detector current vs. applied voltage for a device with anion-passivated MPA capped (post-deposition) PbS QDs.

The device samples with anion passivated surface and 4-fluorothiophenolate-capped PbS quantum dots in the pores of the silicon showed non-linear I-V curves and also had a very slight interaction with the incoming light (Figure 3.11). This indicates that the device is a photodetector, and implies that these devices could possibly be used for X-ray detection.

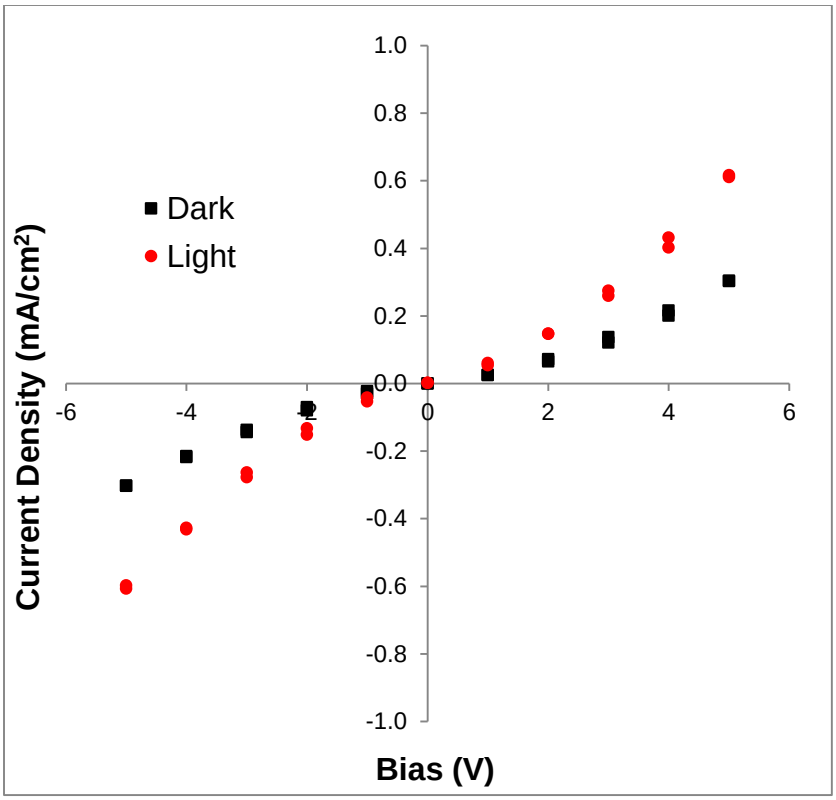

Figure 3.11. Detector current vs. applied voltage in the dark and under illumination for a device with anion-passivated 4-fluorothiophenolate-capped PbS QDs.

With the addition of the anion passivated 4-fluorothiophenolate capped PbS quantum dots to the devices, the samples show clear differences from the straight line or the more resistor-like devices, indicative of a photo-response. Short chain thiolate ligands (4-fluorothiophenolate) and anion passivation at the particle interface show promise as the semiconducting material for our devices, being the only samples that show any appreciable interaction with our light source. The standard sample shows an improved dark current relative to samples manufactured previously for Weinberg Medical Physics. Unfortunately, it is still an order of magnitude larger when compared to the early positive results seen by Weinberg Medical Physics.[20]

3.4 Conclusion

Functional devices using PbS quantum dots as detection for visible light have been previously demonstrated, indicating promise for radiation detectors.[77] It was important for these devices to focus on

using short-chain ligands passivating the PbS QD surface, for improvement in charge transport among the NCs. Improvement in the anodic etching process of the Si wafer, will allow for pore depths closer to 100 μm, as well as smoother pore walls; these device improvements will be the focus for future generations of these X-Ray radiation detection devices. Future work should focus on improvement in the charge transport of the PbS QDs, including different passivating ligand systems allowing for concentrated nanoparticle inks to be deposited into the devices. Most importantly, for this system it is important to have synthetic techniques that afford reproducibility between samples, including the formation of porous silicon, which will allow improvement in device tailoring and sample comparisons.

CHAPTER 4: TOWARDS PROGRAMMABLE ASSEMBLY OF QUANTUM DOTS: ROLE OF CRYSTAL STRUCTURE AND CHALCOGENIDE REDOX PROPERTIES ON THE SOL-GEL ASSEMBLY OF CADMIUM CHALCOGENIDE QUANTUM DOTS

4.1 Introduction

As mentioned in Chapter 1 Section 1, semiconducting nanocrystals (NC) based on metal chalcogenides demonstrate considerable promise for the optoelectronic device industry, due to their easily tunable band gap throughout the visible spectrum, modulated by the size and shape of the nanocrystals. This class of semiconducting quantum dots (QDs) is of considerable interest for optoelectronic device applications such as field-effect transistors (FETs),[15, 75, 136] photodetectors,[76-77] light emitting diodes (LEDs),[78, 137-138] solar cells[80-81] and radiation detectors.[20, 82, 139]

The cadmium chalcogenide NCs, CdS, CdSe and CdTe (CdQ), are expected to benefit from 3D assembly, which would allow for their use in NC based devices, specifically where electron or hole transport is needed. Accordingly, considerable work has been done on exchanging the long-chain insulating ligands typically employed in NC synthesis, with shorter and more labile passivating ligands for the improvement of charge transport in devices.[140-142] Other passivation techniques have been studied to improve the properties of these NCs, such as the use of molecular metal chalcogenide complexes as ligands for colloidal NCs, or halide passivation on the NC surface for solution based passivation.[30, 143-144]

As discussed in Chapter 1, heterostructured devices are a useful way to incorporate two materials with complimentary functionalities into one device. These heterostructured materials have previously been shown to improve photoluminescence yields, such as a shell surrounding NC QD particles being used to reduce trap states.[145-148] Heterostructured materials, including the CdS/CdSe and CdSe/CdTe system, have also been used to improve stability and charge separation, including improvement in the emissive properties of the materials.[149-150] Strong electronic coupling is achieved in carbon nanotube/Au nanoparticle composites; MoS_2 grown on graphene has demonstrated an improvement in the catalytic hydrogen evolution reaction relative to the common MoS_2 catalysts.[30, 151]

The sol−gel assembly method discussed in Chapter 1, can provide a reproducible and robust approach for linking NCs into three-dimensional architectures (i.e., gels, xerogels, and aerogels). The absences of intervening ligands in the macrostructure promotes facile charge extraction while maintaining the quantum confinement effects of the individual NCs.[38, 152] Gelation is achieved by a two-step sol-gel process: 1) irreversible ligand removal (deprotection) by the oxidation of surface thiolate ligands ($2RS^- \rightarrow RS\text{-}SR + 2\ e^-$) and 2) oxidative assembly by formation of di- or polychalcogenide cross-linkages between NCs.[58] To assemble multiple components together in such a way as to control the extent of phase segregation we need to understand the kinetic factors that govern assembly in single component systems.

Previous work has shown that the kinetics of aggregation of CdSe NCs are directly affected by the NC concentration, NC size, and oxidant concentration.[73, 83] Qualitatively, we noted that the rates of CdQ gelation also depend on Q, with tellurides gelling rapidly relative to sulfides.[54] For this dissertation research it was hypothesized that differences in the rate of aggregation and gelation would be directed by the redox characteristics of Q (S = 0.48 V, Se = 0.92 V, and Te = 1.14 V), leading to heterogeneity in multicomponent systems comprising different chalcogenides.[84] In the dissertation study a new and unexpected contributor to the kinetics of assembly was found: the crystal structure adopted by CdQ (cubic zinc blende vs. hexagonal wurtzite) has a profound effect on the rate of gelation. Additionally, it is possible to tune the kinetics in a single metal chalcogenide system by altering steric bulk of the ligand, thus enabling independent variation of kinetic factors for control of heterogeneity in multicomponent assemblies.

4.2 Experimental Section

All the chemicals used in the synthetic methods in this chapter are listed in Chapter 2. Transmission electron microscopy (TEM), UV vis spectroscopy and powder X-ray diffraction (PXRD) were employed for characterization of the NCs, and time resolved-dynamic light scattering (TR-DLS), nuclear magnetic

spectroscopy (NMR), electron paramagnetic resonance spectroscopy (EPR) and Fourier transform infrared spectroscopy (FTIR) were carried out as described in Chapter 2.

4.2.1 Synthesis of CdQ NCs

***zb*-CdS NC Synthesis**. The *zb*-CdS NCs were synthesized following a literature procedure, with slight modification.[153] In a common procedure, 0.086 g $CdCl_2$ (0.5 mmol) was stirred in methanol under Ar gas flow until a clear solution was formed. A solution of 0.125 g Na_2S (0.5 mmol) in methanol was injected, followed by a solution of 4-fluorothiophenolate and triethylamine (Cd:S molar ratio 1:10, based on starting Cd concentration). NCs were dispersed in acetone and isolated by precipitation with n-heptane and centrifugation, this process was repeated one time.

***w*-CdS NC Synthesis**. The *w*-CdS NCs were synthesized by modification of literature procedures.[10, 33, 154] 0.060 g CdO (0.47 mmol), 0.23 g TDPA, and 3.0 g TOPO were heated to 320 °C (with the thermocouple placed in the heating mantle adjacent to the flask exterior) under argon flow. Once a clear and colorless solution was produced, the sample was injected with 2 ml TOP, the temperature was increased to 370 °C, and a solution containing 86 µl (0.41 mmol) of TMS in 2.4 ml TOP was injected. The temperature was held at 370 °C for 10 minutes before being cooled to 75 °C and annealing for 24 hrs. 4 ml of toluene was injected, followed by two cycles of dispersion in toluene and precipitation with ethanol.[38]

CdSe NC Synthesis. CdSe NCs were synthesized by a modified literature preparation.[27, 33, 53, 154-156] In this NC synthetic procedure 0.05 g (0.4 mmol) of CdO was combined with 0.200 g TDPA and 4.0 g TOPO in a round-bottom flask under Ar. The mixture was heated to 320° C until a clear solution was produced, and then the temperature was reduced to 150 °C. A solution containing 0.032 g (0.4 mmol) Se in 2.4 ml TOP was injected to the Cd solution, and the temperature was slowly increased to 220-260 °C depending on desired crystal structure (lower temperature for zinc blende and higher temperature for wurtzite). Finally the solution temperature was reduced to 75 °C and 4 ml of toluene was injected. CdSe NCs were isolated as described for *w*-CdS NCs.

CdTe NC Synthesis. CdTe NCs were synthesized following a literature procedure with slight modification.[54] 0.050 g (0.4 mmol) of CdO was combined with 0.200 g TDPA and 3.75 g TOPO in a round-bottom flask under Ar. The mixture was heated to 320° C until a clear solution was produced and then the temperature of the solution was reduced to 150 °C. A solution containing 0.060 g (0.4 mmol) Te in 2.4 ml TOP was injected to the Cd solution, and the temperature was slowly increased to 270 °C and then quickly cooled. Finally the solution temperature was reduced to 75 °C. CdTe NCs were isolated as described for *w*-CdS NCs.

4.2.2 MHA (MUA) Ligand Exchange for CdQ NCs

For all the CdQ NCs used in the DLS studies a solution of MHA (MUA) and tetramethylammonium hydroxide in methanol was added to solid CdQ NCs (Cd:thiol ratio 1:4, based on original moles of Cd employed in the synthesis) and shaken vigorously. The resulting MHA (MUA)-capped CdQ NCs were precipitated with ethyl acetate and finally dispersed in methanol to form the nanocrystalline sol.

4.2.3 4-fluorothiophenolate Ligand Exchange

A solution of 4-fluorothiophenolate and triethylamine in acetone was added to solid *w*-CdS NCs (Cd:S ratio 1:10, based on original moles of Cd employed in the synthesis) and sonicated. The resulting 4-fluorothiophenolate capped CdS NCs were precipitated with n-heptane and dispersed in acetone to form the nanocrystalline sol.[38]

4.3 Results and Discussion

Previous work in our group verified that, for a constant NC and oxidant concentration, smaller NCs aggregate faster than the larger NCs (CdSe and CdSe@ZnS). Likewise, increasing oxidant concentration decreases the time required to achieve a gel, while resulting in larger aggregate sizes at the gel point, thus decreasing the transparency of the final macroscopic gel.[83] Thus, in order to evaluate the effect of Q, CdQ NCs of similar size were generated from literature preparations and a constant volume of oxidant was employed. NC size was determined by high resolution TEM imaging (Figure 4.1). The average particle size

of CdQ NCs was found to be 4.5 ± 0.6 nm (CdS), 4.7 ± 0.5 nm (CdSe) and 4.6 ± 0.8 nm (CdTe). The kinetics of aggregation of sols of CdS, CdSe and CdTe capped with 16-mercaptohexadecanoic acid (MHA) at a NC concentration of 3 x 10^{-7} M were studied using TR-DLS. The NC concentration was calculated using the first absorption peak in the UV-Visible spectrum to determine the size dependent extinction coefficients, as published by Yu et al.[157]

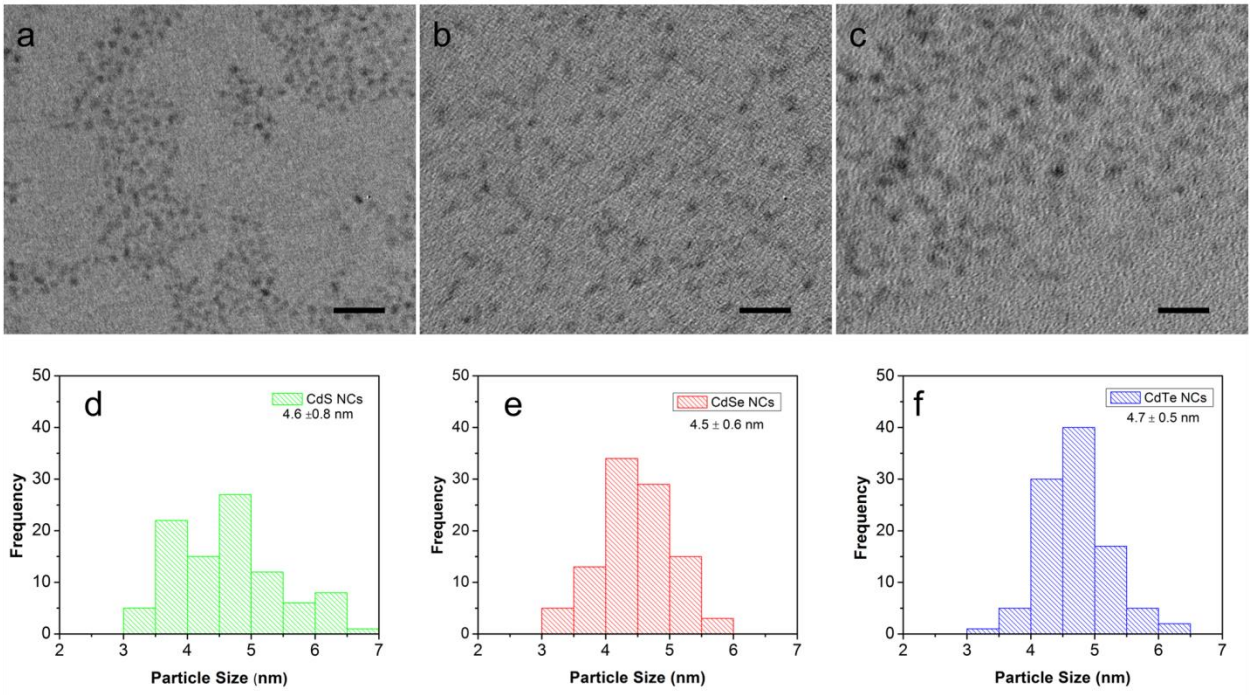

Figure 4.1. The TEM micrographs for 4-fluorothiophenolate-capped a) CdS NCs b) CdSe NCs c) CdTe NCs and the corresponding particle size analysis. The scale bar corresponds to 20 nm.

4.3.1 Initial Time Resolved-Dynamic Light Scattering Studies

For all the TR-DLS measurements, the CdQ sol volumes were held constant (3 mL) and the sol was pipetted into a disposable cuvette. After adding TNM, the disposable cuvette was vigorously shaken and immediately placed in the DLS instrument. The average hydrodynamic radius (R_h) was calculated as described previously.[83]

The TR-DLS graph of the hydrodynamic radius, $\overline{R}_h$ as a function of time after the addition of the oxidizing agent is shown in Figure 4.2. The initial hypothesis was that the kinetics of aggregation would

follow the redox characteristics of Q^{2-}, with Te>Se>S. As expected, the $\overline{R}_h$ for CdTe NCs grows rapidly, achieving a value of ca 1µm by 10 min, indicative of rapid aggregation (the DLCA regime), whereas CdS NCs are slower, taking nearly 20 min to achieve a similar aggregate size (the RLCA regime). However, instead of the CdSe demonstrating intermediate kinetics, these NCs were found to react much slower than CdS, with little upturn prior to 20 min.

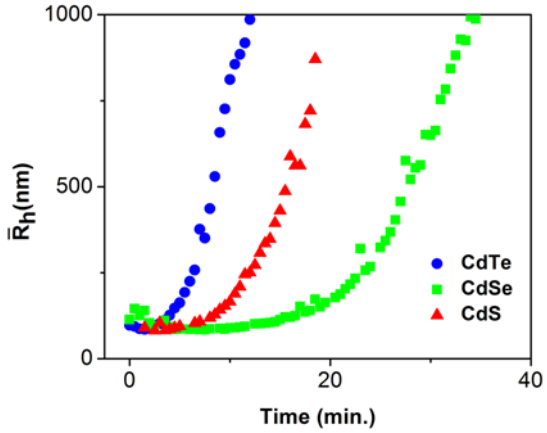

Figure 4.2. Time evolution for $\overline{R}_h$ of CdQ nanocrystals as a function of Q.

Evaluation of PXRD patterns for the three samples reveals a possible explanation (Figure 4.3). The CdSe pattern is indicative of cubic (*zb*) as the major structure type, whereas CdS and CdTe are distinctively hexagonal (*w*). CdSe is known to suffer from polytypism between the *zb* and *w* crystal structures, which differ only by the close-packed layer stacking patterns (ABCABC for *zb* and ABAB for *w*).

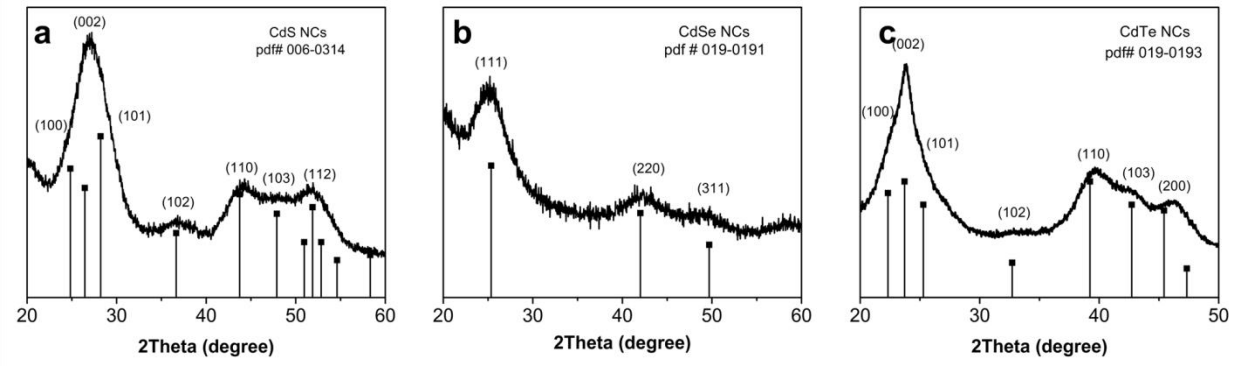

Figure 4.3. PXRD patterns for CdQ NCs a) CdS NCs and corresponding pdf for *w*-CdS b) CdSe NCs with corresponding pdf for *zb*-CdSe and c) CdTe NCs with corresponding pdf for *w*-CdTe.

There is a very low energy difference between the two crystal structure types, within a few millielectronvolts per atom, making interconversion and intergrowth between the two crystals a common occurrence.[158-159] To test the hypothesis that kinetic differences are driven by structure, we chose to compare *w*-CdS to *zb*-CdS because the energy difference between cubic and hexagonal CdS is greater, which could reduce the occurrence of the secondary phase at synthesis temperatures chosen to target the primary phase.[160]

4.3.2 Effect of Structure on Kinetics

Cubic (*zb*-CdS) and hexagonal (*w*-CdS) NCs were prepared following literature procedures and capped with 4-fluorothiophenolate in acetone.[38] Figure 4.4 a-b shows the HRTEM image of the 4-fluorothiophenolate capped *zb*-CdS and *w*-CdS NCs. NC sizes were determined through HRTEM.

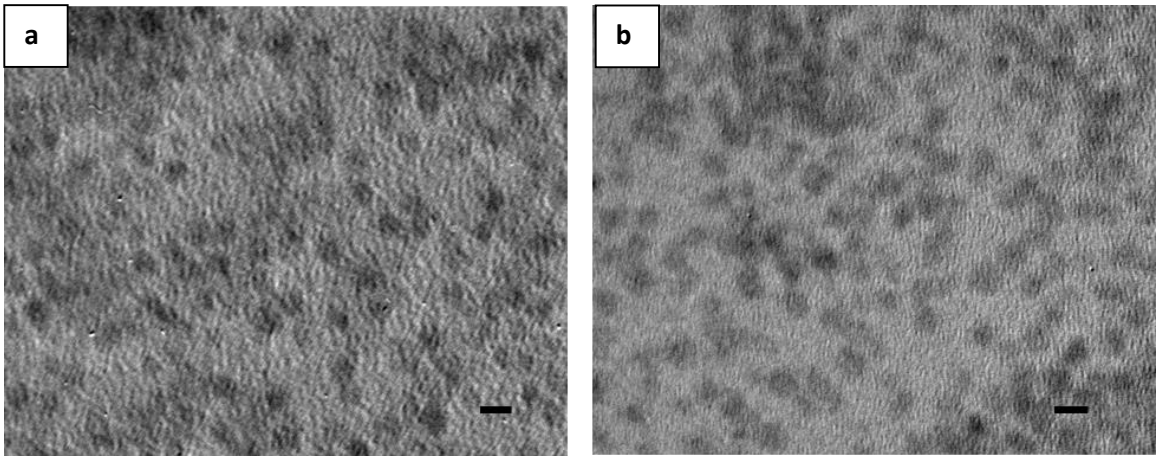

Figure 4.4. The TEM micrographs for a) 4-fluorothiophenolate-capped *zb*-CdS NCs and b) 4-fluorothiophenolate-capped *w*-CdS NCs, scale bar corresponds to 5 nm.

The NC size was 4.1±0.4 nm for *zb*-CdS and 4.5±0.6 nm for *w*-CdS NCs, the histograms and size analyses for both *zb*- and *w*-CdS are shown in Figure 4.5 a-b.

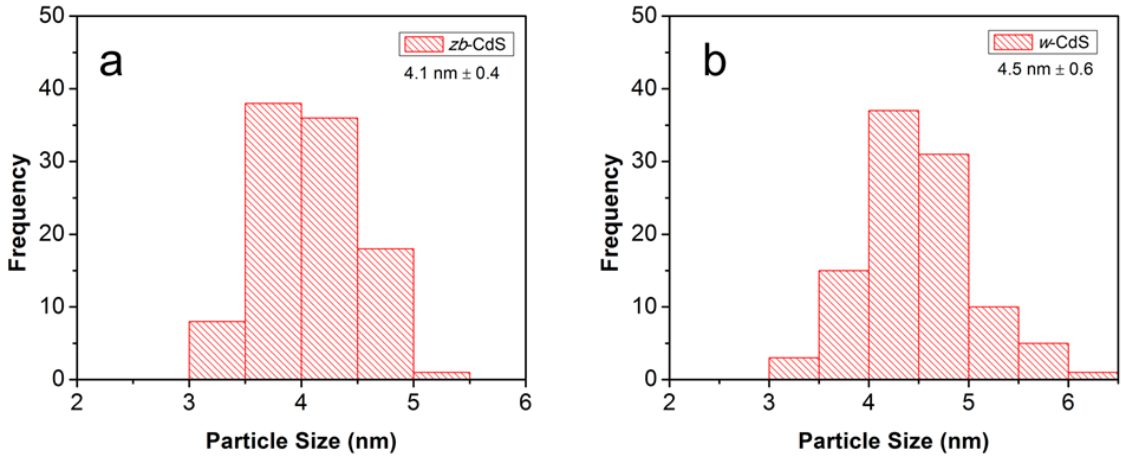

Figure 4.5. The particle size analysis for the a) *zb*-CdS NCs and b) *w*-CdS NCs, based on TEM images shown in Fig. 4.4.

To confirm structure, the PXRD data is shown for the 4-fluorothiophenolate-capped *w*- and *zb*-CdS NCs along with a line diagrams corresponding to the two phases. Formation of *w*-CdS is evidenced by peaks at 37 and 45° 2θ. Comparison of the UV-visible absorption spectra also reveals clear distinctions, with *zb*-CdS having a broad first exciton peak at 455 nm whereas *w*-CdS has a sharper excitonic feature at 415 nm (Figure 4.6 a-b).

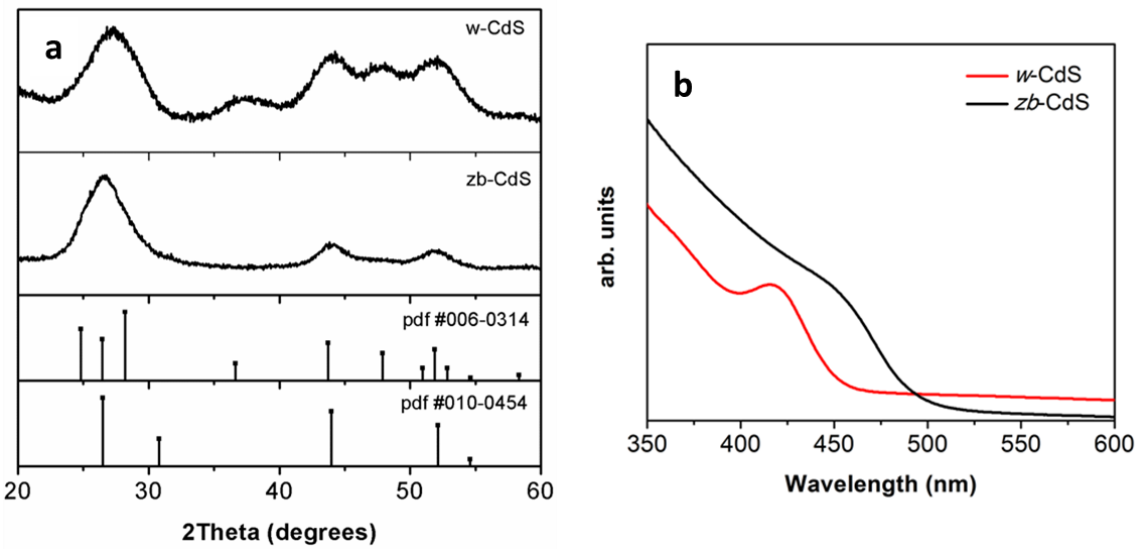

Figure 4.6. a) PXRD patterns comparing 4-fluorothiophenolate-capped *zb*- and *w*-CdS NCs along with pdf's corresponding to wurtzite (006-0314) and zinc blende (010-0454) and b) the UV-Vis spectra for the *zb*- and *w*-CdS NCs.

TR-DLS measurements were performed as described in 4.3.1 on the *w*- and *zb*-CdS sol. Figure 4.7 shows the aggregation kinetics of the *zb*- and *w*- CdS NCs over-time. It is clear that for *w*-CdS, the aggregation is so rapid it occurs within several minutes of introduction of the TNM oxidant. Conversely, the *zb*-CdS NCs have much slower aggregation kinetics, over several hours. Thus the thermodynamics of Q^{2-} oxidation are not sufficient to describe the reactivity; structure must be playing an important role. Given the similarity of the two structure types, we turned our attention to surface effects and considered whether the kinetics of ligand loss (oxidation), which precedes oxidative gelation, contributes to the rate of gelation.

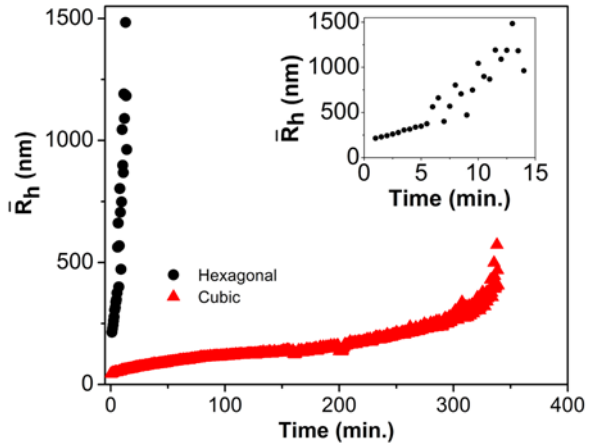

Figure 4.7. Time evolution of $\overline{R}_h$ as a function of crystal structure for *zb*-CdS and *w*-CdS. Inset: the $\overline{R}_h$ as a function of time for *w*-CdS NCs at short time intervals.

Since the *w*-CdS lattice lacks inversion symmetry about the c axis, the (0001) and $(000\bar{1})$ surfaces are crystallographically nonequivalent.[28, 33, 159-162] This difference results in a surface polarity, not present in *zb*-CdS NCs, which are otherwise structurally very similar.[163] It has been postulated that the surface coverage of the capping ligands occurs in islands, which reflect surface facets of the crystals.[164] Gacoin et al. employed the 4-fluorothiophenolate capping ligand to monitor the aggregation and gelation using ^{1}H and ^{19}F NMR spectroscopy.[51, 105] Assuming a two-step process for the colloidal aggregation starting with

1) oxidative loss of the surface thiolate capping agent followed by 2) formation of surface chalcogenide linkages between NCs, monitoring this process in-situ with ^{1}H and ^{19}F NMR would enable us to learn whether a contributing factor in the kinetics of colloidal aggregation was loss of surface thiolate ligand, possibly due to the differences in the surface facets between the two crystal structures.

The solvent volume in the NMR tubes was held constant (750 µl d_6-acetone), for each sample and 9 mg of solid NCs was dispersed. For mechanistic studies of the sol-gel process, 20 µl of a 10% oxidant (TNM) solution was injected into the NMR tubes. NMR spectroscopic studies were performed to probe the 4-fluorothiophenolate loss from *zb*- and *w*- CdS NCs and formation of oxidized products (primarily disulfide). Figure 4.8 shows the ^{19}F NMR spectra for the *w*-CdS NCs before and after the addition of the oxidizing agent, with a broad peak at -124 ppm indicative of the 4-fluorothiophenolate ligand on the surface of the CdS NC clearly evident before addition. There is also a peak corresponding to the disulfide that is centered at -115 ppm and already evident prior to the addition of the oxidant, which we ascribe to photooxidation of the 4-fluorothiophenolate ligand.[51, 105] Upon the addition of the TNM (oxidant) there is a decrease in the peak intensity located at -124 ppm which also shifts downfield and splits into two peaks, with a simultaneous increase in the disulfide peak at -115 ppm, this is indicative of the sol-gel process where surface thiolate ligand oxidation forms the disulfide by-product in solution by Scheme 4.1 and 4.2. The peak shifts for all the spectra that occur upon the addition of the oxidant are likely due to electrostatic charges at the surface of the particle and possibly the formation of the aggregates in solution.[142] During the aggregation and subsequent gelation from time t=0 h to t= 24 h, the NMR peaks corresponding to ligand on the surface of the particle decrease in intensity and broaden as the NCs undergo gelation.

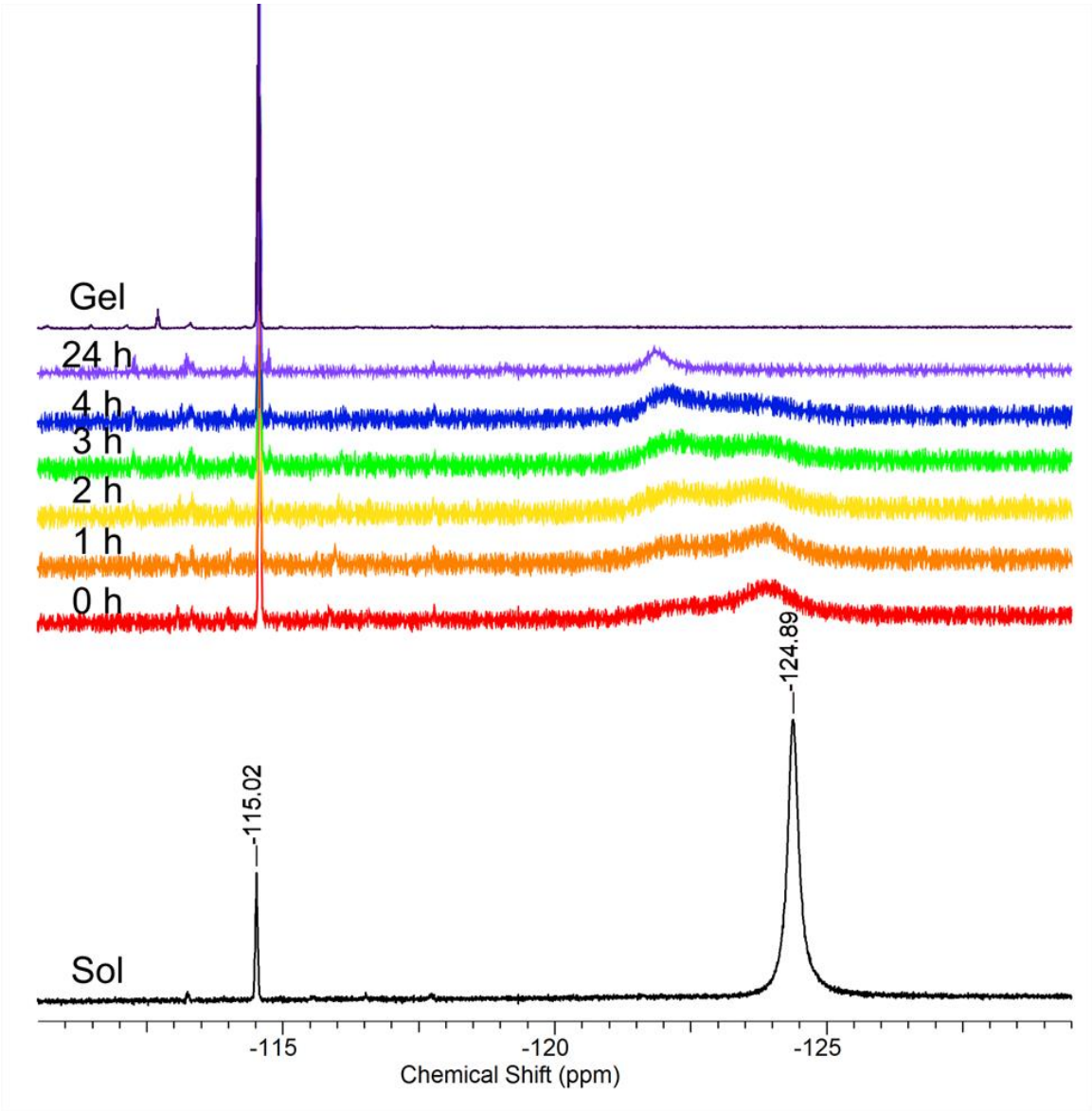

Figure 4.8. Time evolution of the ^{19}F NMR spectra for *w*-CdS NCs upon the addition of TNM (oxidant).

The formation of two peaks in the ^{19}F NMR spectrum at -122 and -124 ppm (at time t=0 h to t=24 h) has been attributed to two species on or near the surface of the NCs, the bridging and terminal thiolate ligand respectively (Figure 4.9).[165]

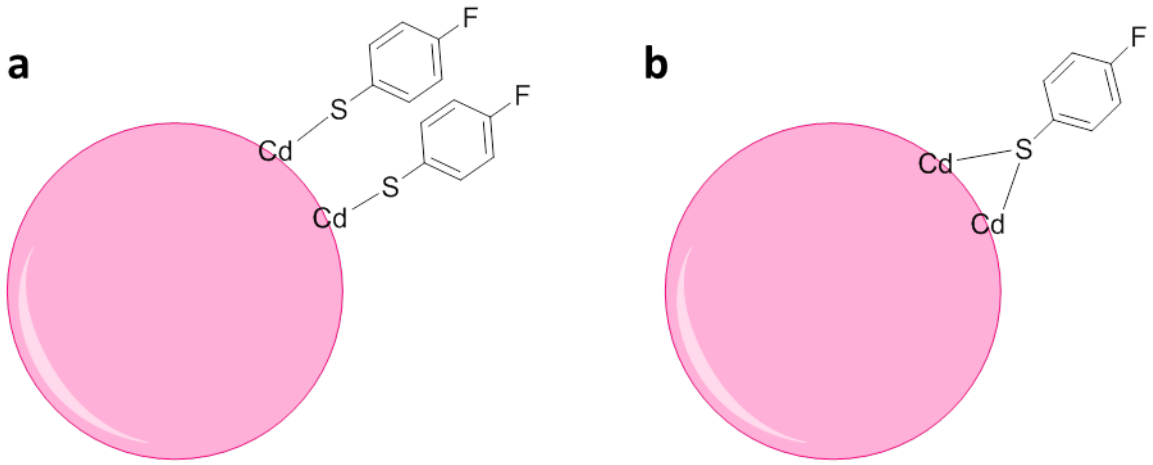

Figure 4.9. The two surface bonding types of the 4-fluorothiophenolate ligand on the CdS surface a) terminal species b) bridging species.

Initially there is a peak at -124 ppm visible prior to the addition of the oxidant. After addition, then a second peak grows in downfield, at the expense of the first, implying a transformation in the nature of the bound thiolate. This may be rationalized by the terminal thiolate species converting to bridging as surfaces are depopulated. Other smaller peaks between -110 ppm and -115 ppm, are likely due to the isomerization shown in Scheme 4.3, which leads to the sulfinate, sulfonate and sulfonic acid derivatives of the 4-fluorothiophenol.[166]

$$(CdS)_mCd(SR)_2 + C(NO_2)_4 \longrightarrow RSNO_2 + Cd(C(NO_2)_3)_2 \quad \text{(Scheme 4.1)}$$

$$RSNO_2 + (CdS)_mCd(SR)C(NO_2)_3 \text{ or } (CdS)_mCd_2(SR) \longrightarrow RSSR + Cd(NO_2)_2 \quad \text{(Scheme 4.2)}$$

$$RSNO_2 \longrightarrow RSONO \quad \text{(Scheme 4.3)}$$

At the gel stage, no peak due to bound 4-fluorothiophenolate is apparent, but it is not clear if it is all removed, or if the formation of the gel prevents tumbling and the peak broadened into the background. Similar chemical transformations are evident in the proton NMR spectra (Figure 4.10). Prior to the addition of the oxidant, peaks centered around 6.63 and 7.43 ppm can be identified for the ortho- and meta-protons of the 4-fluorothiophenolate-capping ligand on the NC surface, respectively. Following addition

of the oxidant, triplet peaks centered around 7.16 and 7.56 ppm, indicate the formation of the disulfide byproduct.

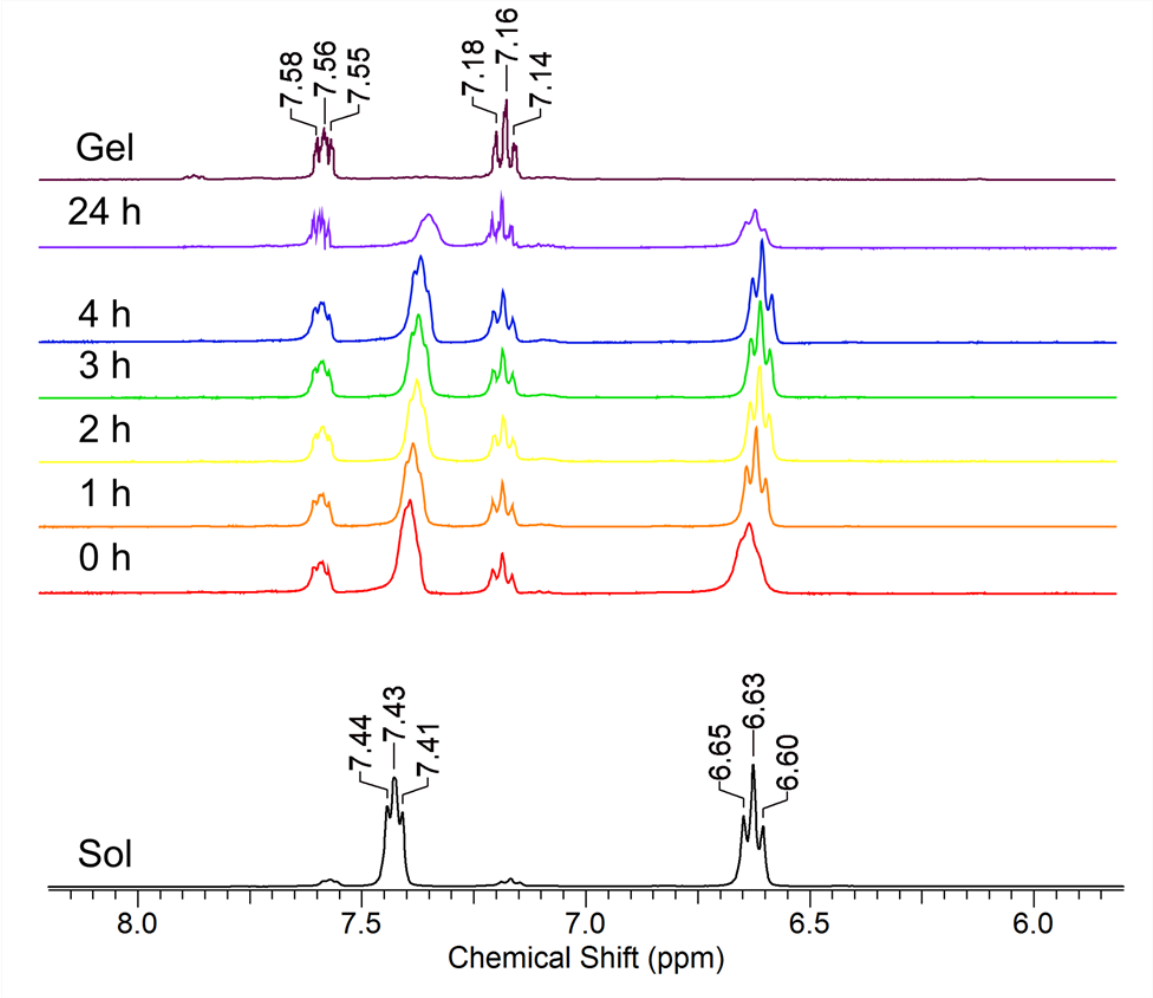

Figure 4.10. ^{1}H NMR spectra of *w*-CdS sols at different times after TNM (oxidant) addition.

Figure 4.11 shows the ^{19}F NMR spectra of the *zb*-CdS NCs sol and gel after the addition of the oxidizing agent, which also shows that while there is some disulfide formation with an indicative peak in the ^{19}F NMR spectra at -116 ppm, a large amount of 4-fluorothiophenolate ligand remains on the surface of the *zb*-CdS NCs post-gelation, manifesting as a broad peak at -123 ppm. Another peak at -112 ppm (which is also seen in the *w*-CdS) is attributed to the sulfonate species which is a by-product of the oxidation of the surface 4-fluorothiphenolate, which can form when the $RSNO_2$ species reaction with RSH is limited (Scheme 4.3), suggesting the concentration of available thiolate may be smaller in the *zb*-CdS samples

than in the *w*-CdS sample. The NMR studies seemed to indicate that the surface ligand loss for the *zb*-CdS NCs after the addition of the oxidant is slower than for the *w*-CdS, which correlates with the TR-DLS studies and may well indicate that one of the factors in the slower kinetics of aggregation with *zb*-CdS may be slower surface thiolate ligand loss.

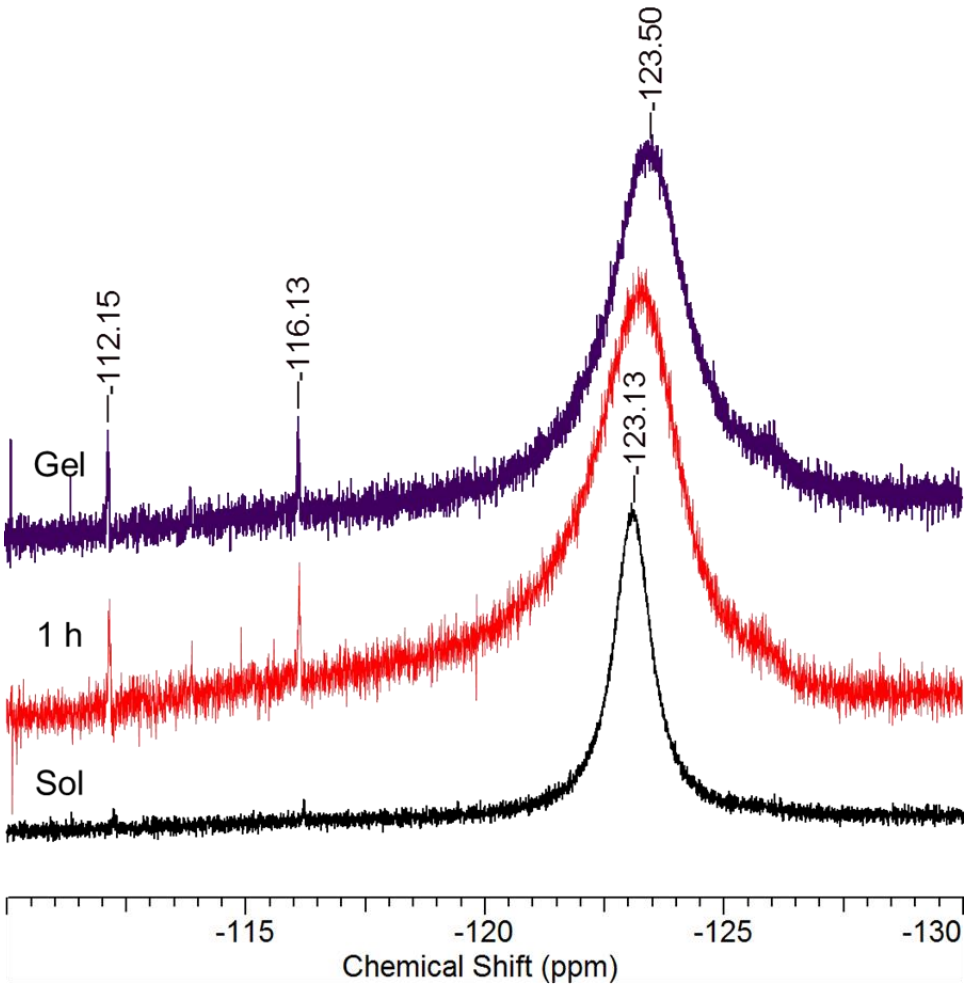

Figure 4.11. Time evolution of the ^{19}F NMR spectra for *zb*-CdS NCs upon the addition of TNM (oxidant).

Figure 4.12 is the ^{1}H NMR spectra of the *zb*-CdS NCs sol before addition of the TNM and after gelation, only one intermediate spectra was included as they showed little change over-time. The broad triplet centered at 6.8 ppm and 7.3 ppm corresponds to the thiolate capping on the surface of the particles, there is no evidence for the formation of disulfide.

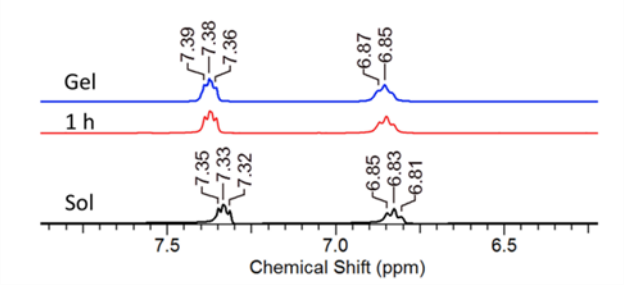

Figure 4.12. ^{1}H NMR spectra of *zb*-CdS sols for different times after TNM (oxidant) addition.

4.3.3 Surface Effects

A characteristic feature of the *zb*-CdS NMR spectra was the peak broadening, possibly indicative of a paramagnetic center in this sample. We considered whether this might have an effect on oxidative gelation. To verify the presence of a paramagnetic impurity, electron paramagnetic resonance spectroscopy (EPR) was performed on samples of "uncapped" *zb*-CdS, without the addition of the capping ligand (4-fluorothiophenolate) and samples of the *zb*-CdS synthesized with the 4-fluorothiophenolate capping ligand. Figure 4.13a shows the EPR spectrum of the uncapped (no addition of the 4-fluorothiolphenol ligand) *zb*-CdS NCs, which shows a clear EPR signal with a g value of 2.004 that matches with known values for anionic vacancies in similar *zb*-CdS NCs.[167] Figure 4.13b is the EPR spectrum for 4-fluorothiophenolate capped *zb*-CdS NCs, which showed the same g=2.004 signal, along with a new signal in the EPR spectrum that we could not identify, but which seems to be a product of the 4-fluorothiophenolate addition. In contrast, the EPR spectrum for the *w*-CdS showed no EPR signal (Figure 4.13c). Finally, Figure 4.13d shows the EPR spectrum for the *zb*-CdS upon gelation (following the addition of the oxidizing agent, TNM), which showed no peak in the EPR spectrum, indicating that paramagnetic centers are no longer present. We surmise that the oxidative gelation process eventually leads to passivation of these defects.

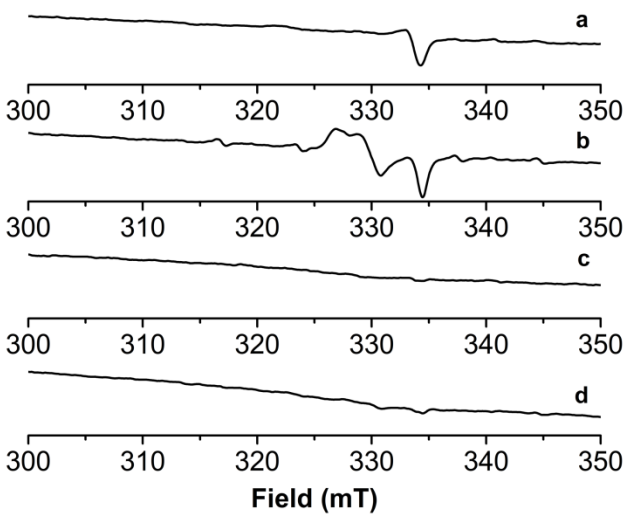

Figure 4.13. EPR Spectrum for the a) uncapped *zb*-CdS nanocrystals b) 4-fluorothiophenolate-capped *zb*-CdS nanocrystals c) *w*-CdS nanocrystals capped with 4-fluorothiophenolate ligand and d) the *zb*-CdS gels.

Table 4.1 gives the known literature g-values for vacancies in bulk and single-crystal CdS and ZnS. The specific anionic vacancy for CdS crystals behaves as a double donor, with a paramagnetic singly occupied state.[167-170]

Table 4.1. Parameters for Native Defect Centers in CdS and ZnS.

	Vacancy Type	**g-value**	**Ref.**
CdS	V_{Cd}	2.0018	[168]
ZnS	V_{Zn}	2.0019	[169]
ZnS	V_S	2.0034	[170]
CdS	V_S	2.004	[167]

If these are considered anionic vacancies at or near the surface of the *zb*-CdS nanocrystals, this could explain at least a trivial amount of the slower onset and kinetics of aggregation. If there was a decrease in surface chalcogenides then there would be a decrease in the sticking probability of these nanocrystals in solution.

Alternatively, we considered whether the surface is more oxidized in the *zb*-CdS. A recent paper by Thomas et al. discussed the role of the surface composition of CdSe QDs on the luminescence properties between *zb*-CdSe and *w*-CdSe, which indicated that *zb*-CdSe NCs with a surface layer of CdO showed improvement in the PL emission.[171] To determine if our *zb*-CdS QDs could also have an oxide layer, which could prevent the formation of dichalcogenide linkages and arrest the aggregation and gelation in solution, XPS studies were conducted. The binding energies of cadmium $3d_{5/2}$ and $3d_{3/2}$ electrons for CdS bulk are reported to be 405 and 412 eV respectively.[172] The Cd spectra for *zb*-CdS QDs is presented in Figure 4.14a, and the *w*-CdS QDs in Figure 4.14b. Following the Shirley background subtraction, the peaks were deconvoluted into Gaussian components, which offer insight into the structure of these CdS QDs. For both cases, the peaks for the Cd bound to sulfur for the Cd $3d_{5/2}$ and Cd $3d_{3/2}$, are seen at 405 and 412 eV in Figure 4.13. Both the spectra have peaks corresponding to the oxidized form of Cd for both the 3d3/2 and 3d5/2 signals, which are shifted 2 eV from the original Cd signal. However the XPS indicates that the *zb*-CdS NCs do not have a significant CdO layer when compared to the *w*-CdS, which would have affected the kinetics of aggregation of the nanocrystals in solution.

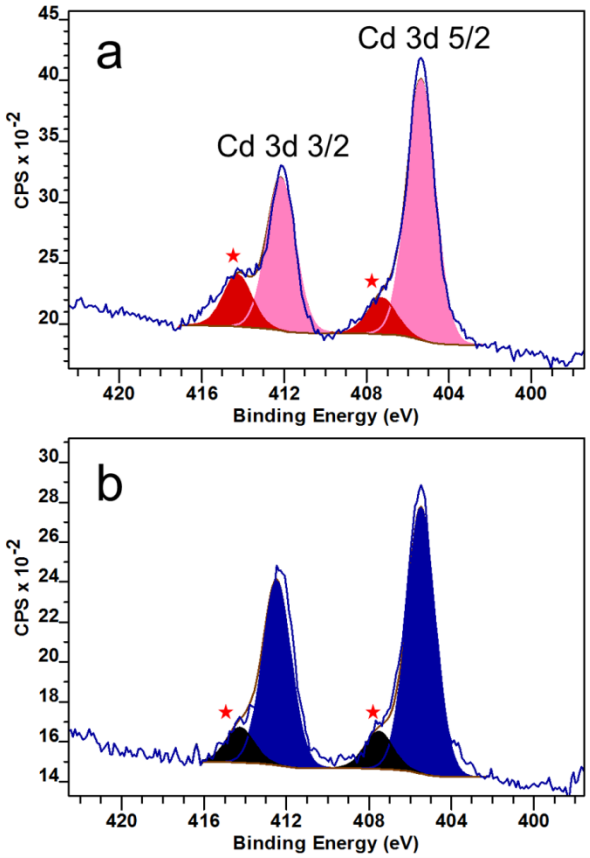

Figure 4.14. XPS elemental analysis of two CdS QD samples capped with 4-fluorothiophenolate ligand a) *zb*-CdS; the peak corresponding to the Cd atom bound to S is represented by the pink trace, while the peak bound to O is represented by the red trace. b) *w*-CdS; the peak corresponding to the Cd atoms bound to S is represented by the blue trace and the peak corresponding to the Cd bound to O is represented by the black trace. The red star indicates the oxidized Cd peaks, which are blue-shifted from the peaks seen for the CdS signals for both the $3d_{3/2}$ and the $3d_{5/2}$.

Finally, we considered whether the extent of surface capping might be playing a role in the kinetics; perhaps due to better passivation of *zb*-CdS. To determine the capping group concentration in each case, we removed all the organics by treatment with excess TNM and the concentration of disulfide was determined by ^{19}F NMR (Figure 4.15). Peaks corresponding to the organic 4-fluorothiophenolate capping ligand (-124 ppm) are absent after treatment with excessive TNM, indicating removal of surface ligands. A common standard for ^{19}F NMR spectroscopy, hexafluorobenzene, with a known concentration of 0.447 M was added to each test tube containing the CdS samples (*zb*- and *w*-) that had been over-oxidized using excess TNM oxidant to remove all the thiolates as disulfide from the NC surface. The concentration of

disulfide by-product was determined based on the standard hexafluorobenzene concentration; this did not include the other reaction by-products, which, due to noise, could not accurately be accounted for in the determination.

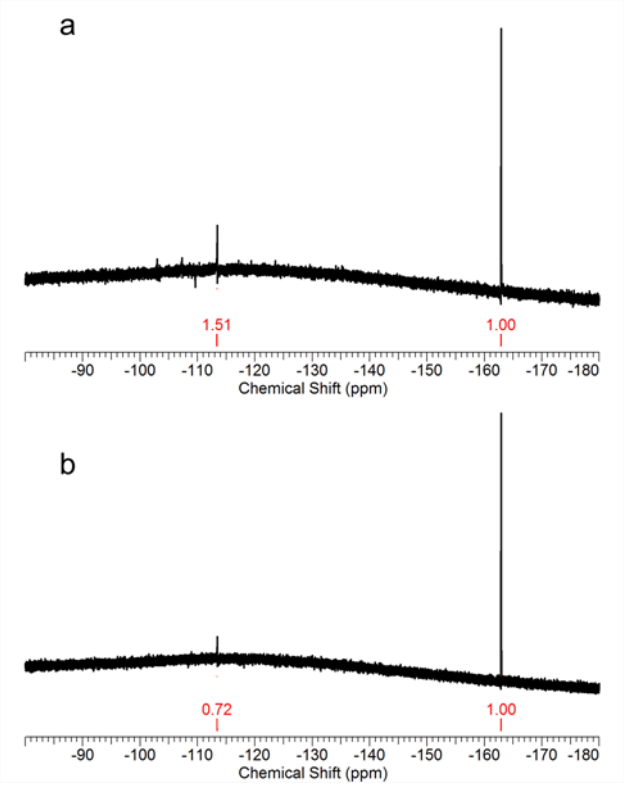

Figure 4.15. The ^{19}F NMR spectrum for the over-oxidized a) *w*-CdS NC sol and b) *zb*-CdS NC sol.

The IR spectra performed for the CdS NCs before and after treatment with TNM oxidizing agent, indicated the removal of a majority of the surface ligands (Figure 4.16). The peak at 1222 cm^{-1} for the C-F stretching vibration of the 4-fluorothiophenolate ligand on the NC surface is initially present but disappears, following the oxidative ligand removal and gelation.

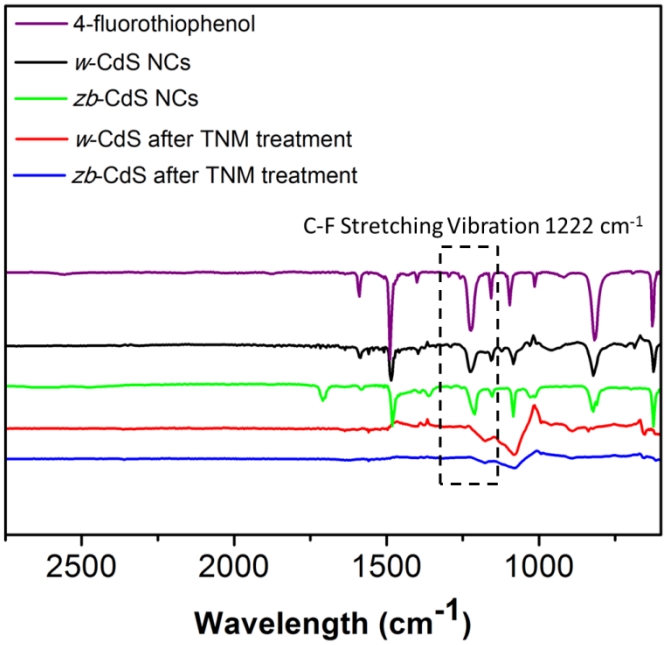

Figure 4.16. The IR spectrum for (*zb* and *w*) CdS NCs prior to, and following, treatment with TNM oxidant.

For the *zb*-CdS NCs there were an average of 75 4-fluorothiophenolate ligands per particle (5.68 ligands/nm^2); the *w*-CdS NCs had much higher surface ligand coverage with an average of 300 4-fluorothiophenolate ligands per particle (18.9 ligands/nm^2). It is known that ligand surface coverage can affect the assembly of NCs into heterostructures.[173] The more symmetric crystal structure of the *zb*-CdS NCs would a result in facets of similar surface energies, whereas in *w*-CdS, the (0001) surface facets have considerably higher surface energy requiring more ligands to achieve passivation.[164] Indeed catalytic H_2 evolution using CdS occurs at a greater rate for *w*- vs *zb*-CdS NCs. The reactivity of the *w*-CdS crystals is ascribed to the higher energy (0001) surface facets. Such higher energy surfaces could attract more of the capping 4-fluorothiophenolate ligand.[174] Another known feature of NCs having facets of different energies, such as occurs in the wurtzite crystal structure, is that they can undergo oriented attachment resulting in anisotropic structures. However, we do not see any evidence of oriented attachment in our gels.[175]

4.3.4 Effect of Q on Gelation Kinetics in *w*-CdQ NCs

In this dissertation research we have demonstrated that the crystal structure types for CdQ will have an effect on the kinetics of colloidal aggregation in solution. Accordingly, sols of *w*-CdS, CdSe and CdTe capped with 16-mercaptohexadecanoic acid (MHA) at a NC concentration of 3 x 10^{-7} M were evaluated to determine whether relative redox properties of Q would affect kinetics of aggregation as originally postulated when the structures are all the same. PXRD data and HRTEM images are shown in Figures 4.17 and 4.18, respectively, indicating the NCs are in the wurtzite crystal structure.

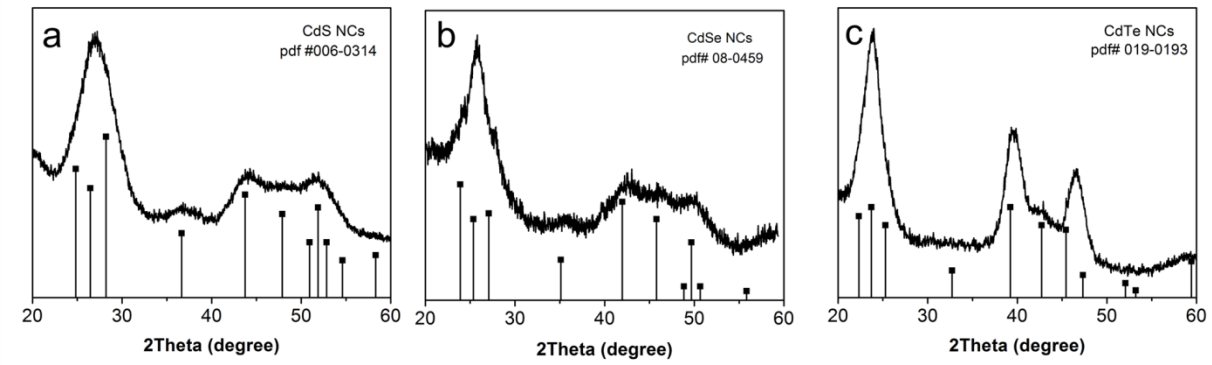

Figure 4.17. PXRD spectrum for TOPO-capped a) *w*-CdS b) *w*-CdSe and c) *w*-CdTe.

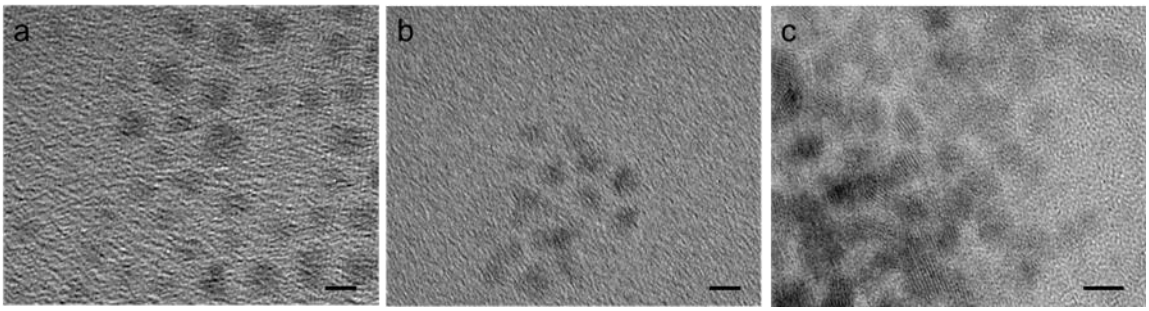

Figure 4.18. TEM micrographs for TOPO-capped a) CdS NCs b) CdSe NCs and c) CdTe NCs. The scale bar corresponds to 5 nm.

The average particle size for each CdQ NC was determined using HRTEM, the histograms and particle size analysis are shown in Figure 4.19, and indicate the NCs are similar in size.

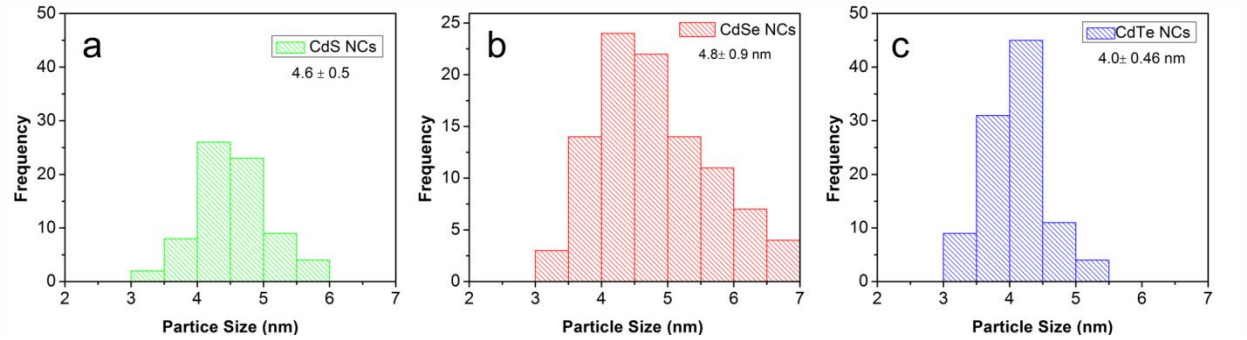

Figure 4.19. Particle size analysis of TOPO-capped a) CdS NCs b) CdSe NCs and c) CdTe NCs.

Figure 4.20 shows the change in hydrodynamic radius as a function of time in *w*-CdQ (Q= S, Se and Te) NCs, after the addition of 20 µl 3% TNM solution (oxidant). Once the crystal structure effects are accounted for, the onset of gelation follows the relative redox properties of the Cd-chalcogenides. Specifically *w*-CdTe has the fastest onset and aggregation kinetics in solution, followed by CdSe and finally CdS. Thus, correcting for the crystal structure effects, the relative redox properties do affect the kinetics of aggregation in solution.

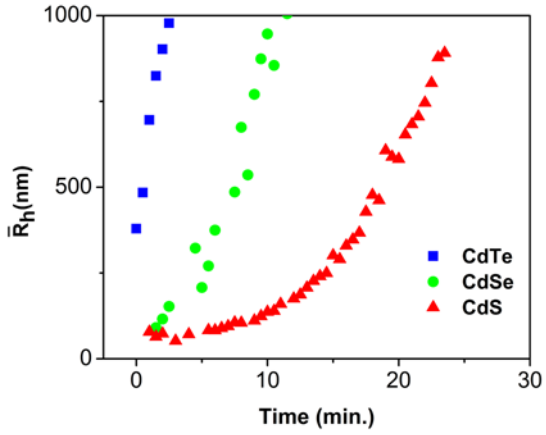

Figure 4.20. Time evolution as a function of chalcogenide, for $\bar{R}_h$ in *w*-CdQ NCs.

4.3.5 Bulkier Capping Ligands as a Control Lever over Kinetics of Colloidal Aggregation

The initial studies to test how the capping ligand would affect the kinetics of aggregation in solution were performed on the well-studied *w*-CdS NC system, due to the ease of synthesis and reproducibility of

these nanocrystals, as well as their relative stability in solution. The CdS nanocrystals were characterized using TEM to determine their particle size of 4.3 nm (Figure 4.21a), and PXRD to verify that they crystallized in the wurtzite (hexagonal) crystal structure (Figure 4.21b). In the PXRD pattern the peaks for the (100), (101) and the (102) reflections, indicative of the wurtzite crystal structure are visible.

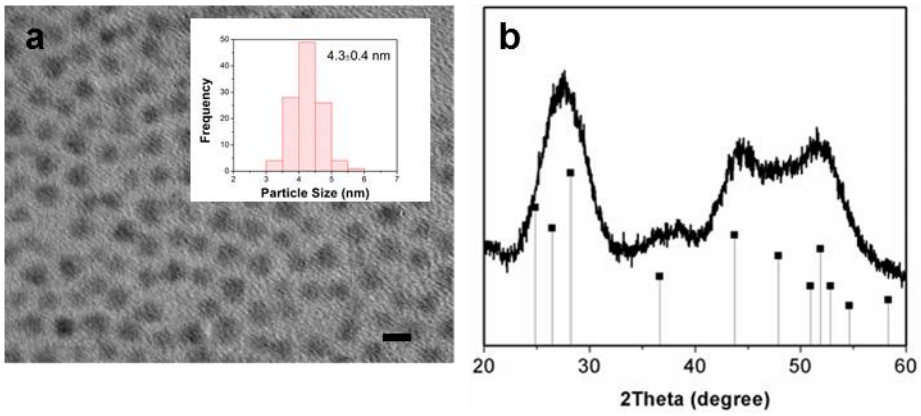

Figure 4.21. The a) TEM micrograph image for the TOPO-capped CdS NCs, with the inset for the particle size analysis (scale bar corresponds to 5 nm) and the b) PXRD pattern for the CdS NCs showing they crystallize in the wurtzite (hexagonal) crystal structure.

Once the nanocrystals were characterized, the TOPO-capping ligands were exchanged with either 16-mercaptohexadecanoic acid (MHA) or 11-mercaptoundecanoic acid (MUA) (Figure 4.22). As seen in the 3-D models of the two ligands, when comparing the 11-carbon chain MUA ligand to the 16-carbon chain MHA ligand, it is clear that the MHA is a longer ligand, making for a thicker barrier for the oxidant to get to the surface and initiate the ligand removal process.

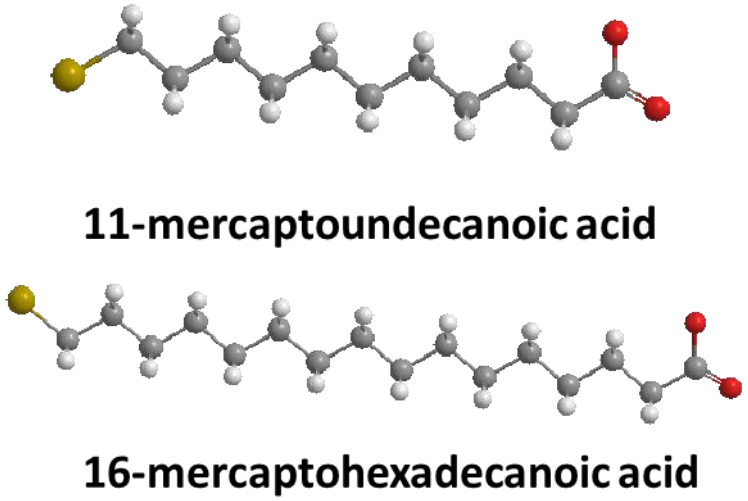

Figure 4.22. The 3D models of the chemical structure for the 11-mercaptoundecanoic acid capping ligand and the 16-mercaptohexadecanoic acid capping ligand.

Time resolved-dynamic light scattering was used to monitor the kinetics of aggregation in solution based on the capping ligand. In the graph of the hydrodynamic radius ($\overline{R}_h$) over-time for both the MUA (MHA) capped nanocrystals, the nanocrystals with the larger or more sterically bulky capping ligand (MHA) displayed the slowest kinetics of aggregation in solution (Figure 4.23).

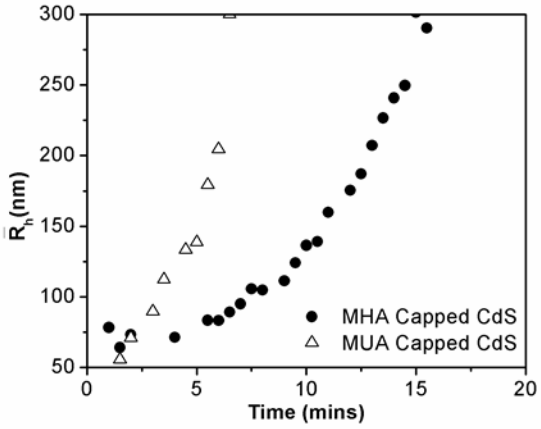

Figure 4.23. The graph of hydrodynamic radius ($\overline{R}_h$) over-time for *w*-CdS as a function of the capping ligand (MHA vs MUA).

4.4 Conclusion

Through TR-DLS studies, NMR spectroscopy and EPR spectroscopy, we show that the crystal structure and characteristics of Q in CdQ NCs both affect the kinetics of oxidative colloidal aggregation. Using NMR spectroscopy, the surface ligand loss differences between the *w*-CdS and the *zb*-CdS NCs has been identified as a possible reason for the extreme differences in the kinetics of colloidal aggregation, with the larger concentration of surface ligand coverage possibly reflecting the higher surface reactivity of the *w*-CdS. Our results suggest that the surfaces of the NCs, either surface structure of facets, surface ligand coverage and/or surface vacancies, will affect rate of gelation of CdQ NCs. For identical structures and sizes, the gelation kinetics followed the thermodynamic trend with respect to the redox properties of Q_2^{2-} for Q= S, Se and Te. The ability to tune the kinetics of colloidal aggregation through changing the crystal structure and surface ligand characteristics enabling development of heterostructured gels as described in the next chapter.

CHAPTER5: THE SOL-GEL SYNTHESIS OF MULTICOMPONENT MATERIALS WITH PROGRAMMABLE CONTROL OF HETEROGENEITY

5.1 Introduction

As discussed in Chapter 1, colloidal II-VI MQ (M=Cd and Zn, Q=S, Se and Te) quantum dots have been developed for use in practical solid-state applications including optoelectronic devices, lasers and LEDs.[81, 176-177] To improve photostability in these nanomaterials, and expand the device application properties, colloidal heterostructures have been developed. QD heterostructures include core-shell structures, gradient alloys, and heteronanocrystal composites, with the latter generally encompassing a combination of semiconducting NCs and noble metal nanoparticles.[67-69, 145-146, 178-180] These heterostructures are colloidal in nature, thus issues pertaining to charge transport in the solid state are unaddressed.[181]

In the dissertation research we once again utilize our sol-gel assembly process to provide an approach to linking nanocrystals into three-dimensional architectures (i.e., gels, xerogels, and aerogels) and thin films this time applying the method to a mixture of two different metal chalcogenide quantum dots.[38, 100, 102, 182]

Work in our group has shown that the kinetics of aggregation of II-VI type colloidal NCs is directly affected by the NC concentration, NC size, crystal structure, surface passivating ligand, oxidant concentration and the chalcogenide (Q) relative redox properties (see Chapter 4).[83] The redox properties of Q, have been shown to be an important lever for controlling the kinetics of aggregation, with tellurides gelling rapidly relative to sulfides.[57] All of these tools allow us to tailor the kinetics of aggregation in solution to favor heterobonding between dissimilar particles (Figure 5.1), leading to well-mixed composites or favor homobonding, leading to extensive phase-segregation.

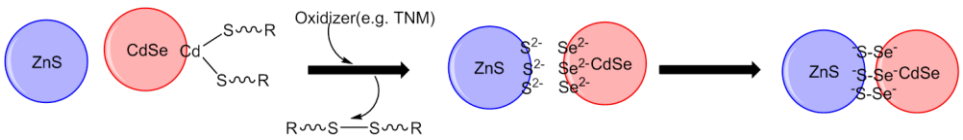

Figure 5.1. Scheme for colloidal sol-gel synthesis of mixed metal chalcogenide heterostructures (specifically CdSe/ZnS system).

Accordingly, the focus of Chapter 5 is on creating multicomponent nanoparticle systems, using CdSe and ZnS as a test case, and tuning the extant of hetero- and homobonding to control the nature of mixed systems (Figure 5.2).

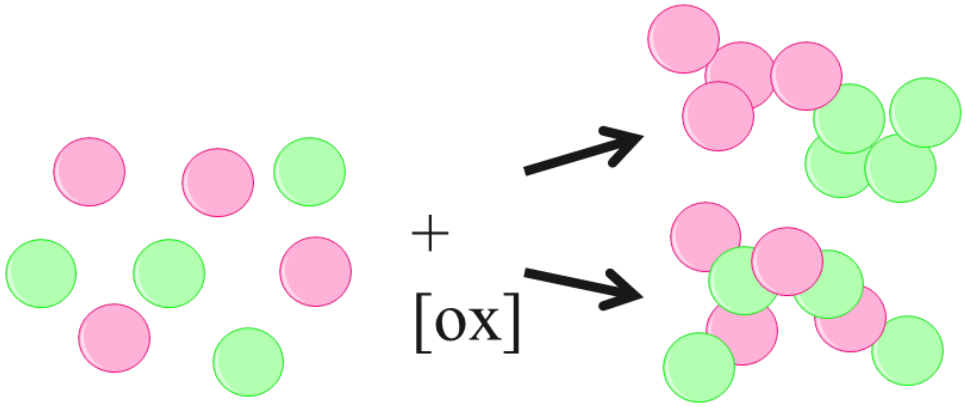

Figure 5.2. Types of hetero- or homogeneous systems that can be produced through tuning the kinetics of colloidal aggregation.

The intrinsic kinetics of colloidal aggregation governed by Q and the native structure will be changed by altering the sterics of the surface passivating ligand. By adjusting the assembly rate of the CdSe and ZnS NPs to be similar, intimately mixed composites will be formed, whereas if the rates are quite different, phase-segregated materials will be produced).

5.2 Experimental Section

All the materials and chemicals used in the syntheses defined in this chapter are described in Chapter 2. Transmission electron microscopy (TEM), inductively coupled plasma mass spectrometry (ICP-MS), UV-vis spectroscopy, powder X-ray diffraction (PXRD) and photoluminescence spectroscopy (PL) were utilized for characterization of materials. Time resolved-dynamic light scattering (TR-DLS) and studies of aggregation kinetics were performed as described in Chapter 2.

5.2.1 Synthesis of MQ (M= Cd and Zn, Q=S and Se) Quantum Dots

5.2.1.1 Synthesis of *zb*-ZnS NCs

The procedure for ZnS NC synthesis was performed on a Schlenk line under air free conditions. ZnS NCs were synthesized following literature procedures, with slight modification.[183] For a typical synthesis, 0.054 g (0.4 mmol) of $ZnCl_2$ was combined with 10 ml oleylamine and 3.75 g TOPO in a round-bottom flask under Ar. The mixture was heated to 170 °C and then the temperature was reduced to 150 °C. A solution containing 0.013 g (0.4mmol) S in 2.4 ml oleylamine was injected to the Zn solution, and the temperature was slowly increased to 320 °C for 10 mins. The sample was precipitated with ethanol once, to give solid *zb*-ZnS NCs.

5.2.1.2 Synthesis of *zb*-CdSe NCs

CdSe NCs were synthesized following literature procedures, with slight modification.[27, 33, 162, 184] In a typical synthesis, 0.05 g (0.4 mmol) of CdO were combined with 0.200 g TDPA and 4.0 g TOPO in a round-bottom flask under Ar using Schlenk line techniques. The mixture was heated to 320 °C until a clear solution was produced, and then the temperature was reduced to 150 °C. A solution containing 0.032 g (0.4mmol) Se in 2.4 ml TOP was injected to the Cd solution, and the temperature was slowly increased to 200 °C and held for 4 h at which point the solution turned a reddish-orange color. Finally the solution temperature was reduced to 75 °C and injected with 4 ml toluene was injected. *zb*-CdSe NCs were isolated by precipitation with ethanol.

5.2.1.3 Ligand Exchange (11-mercaptoundecanoic acid or 16-mercaptohexadecanoic acid)

A solution of MHA (MUA) and tetramethylammonium hydroxide in methanol was added to solid MQ NCs (metal:thiol ratio 1:4, based on original moles of Cd employed in the synthesis) and shaken vigorously. The resulting MHA (MUA) capped MQ NCs were precipitated once with ethyl acetate and finally dispersed in methanol as a nanocrystalline sol.

5.2.1.4 Wet Gel/Aerogel Synthesis

MQ NC sols were prepared in methanol with a concentration of 4.8 x 10^{-6} M (concentration for CdSe NCs was determined using the method developed by Yu et. al. and concentration for ZnS NCs was determined through ICP-MS). For each sample, a 2 ml aliquot of NC sol (1 ml CdSe and 1 ml ZnS) was used and 20 µl of 3% TNM solution was added, followed by shaking. Gels were allowed to age for 3-5 days during which time syneresis occurred, producing a yellow-colored liquid above the gel; the color is attributed to the by-products of TNM oxidation of surface thiolates. The liquid volume was exchanged with methanol until a clear solution above the gel was obtained. The gels were dried using supercritical CO_2 in a Tousimis Autosamdri-931 critical point dryer.

5.3 Results and Discussion

5.3.1 Co-gelation of CdSe and ZnS QDs

To probe whether the change in steric bulk of the capping ligand could be used to affect the degree of mixing in a macroscopic gel structure, CdSe and ZnS QDs were chosen for study based on the anticipated ease of characterization; specifically, as they have different metal cations and chalcogenides, and the optical properties are distinct. Additionally, the same zinc blende structure is targeted for each so that kinetics will depend only on Q and the ligand steric bulk. The starting *zb*-CdSe (ZnS) NCs were synthesized as described previously and characterized using TEM to determine the average particle size: 4.2±0.5 nm (4.0±0.6 nm) as shown in Figure 5.3 a,b (Figure 5.3 e,f). PXRD confirmed that both CdSe and ZnS crystallized in the zinc blende (cubic) form (Figure 5.3c and 5.3g). Single component gels were prepared by oxidative sol-gel synthesis and transformed to aerogels by supercritical CO_2 solvent removal. The diffuse-reflectance measurements for the resultant aerogels for CdSe NCs and ZnS NCs show an absorption onset of 2.3 eV and 3.5 eV, respectively (Figure 5.3d and 5.3h).

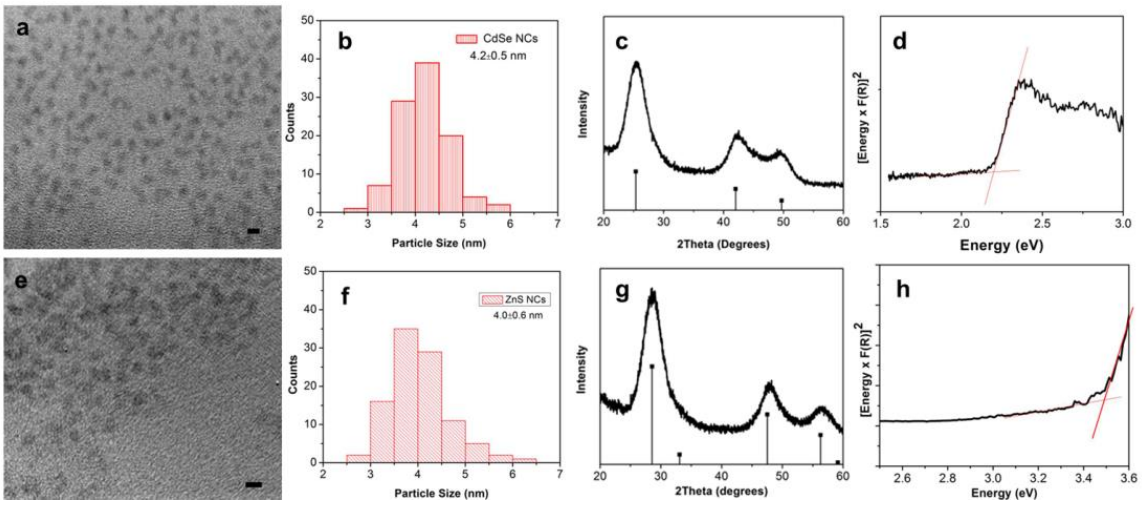

Figure 5.3. a) TEM micrograph of TOPO-capped CdSe NCs b) size distribution histogram c) PXRD pattern for the CdSe with the pdf line diagram corresponding to the zinc blende (cubic) CdSe d) diffuse-reflectance measurements of the resulting CdSe aerogel e) TEM micrograph corresponding to TOPO-capped ZnS NCs f) size distribution histogram g) PXRD pattern for ZnS NCs with the pdf line diagram corresponding to zinc blende (cubic) ZnS h) the diffuse-reflectance measurements of the resultant ZnS aerogel. The scale bar in a) and e) corresponds to 5 nm.

To monitor the kinetics of aggregation for the MUA (MHA) capped z*b*-CdSe and the MUA-capped *zb*-ZnS nanocrystals that will be used for these heterostructured materials, TR-DLS experiments were run for all three samples using a nanocrystal sol concentration of 3 x 10^{-7} M (ZnS concentration determined through ICP-MS). 3 ml of each sol was placed in a disposable cuvette and upon addition of 20 µl of 3% TNM (oxidant) solution the cuvette was shaken once and placed in the instrument. The MHA-capped CdSe NCs had slower kinetics of aggregation than the MUA-capped CdSe NCs (Figure 5.4), as expected. However, both of these samples showed faster kinetics of aggregation relative to the z*b*-ZnS. This is attributed to the relative redox properties of selenium (-0.92 V) as compared to sulfur (-0.48 V).[84]

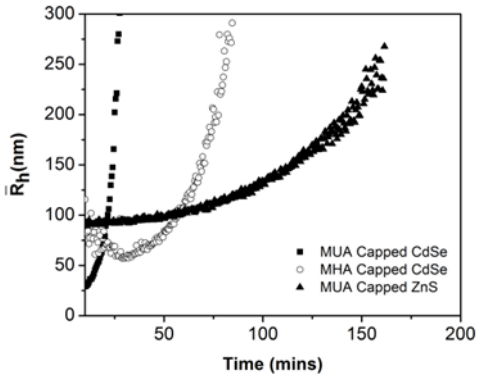

Figure 5.4. Time evolution as a function of metal and capping ligands, for $\overline{R}_h$ in *zb*-MQ NCs.

Having confirmed the ability to manipulate the kinetics of aggregation for CdSe NCs by changing the steric bulk of the ligand, the kinetic difference relative to MUA-capped ZnS can be exploited to synthesize co-gels with different degrees of mixing.

5.3.2 Phase-segregated Gels

Based on large kinetic differences between MUA-capped CdSe and ZnS we expect the resultant co-gels to exhibit a high degree of phase segregation. The concentration for each sample was determined to be 4.8 x 10^{-6} M, and 1 ml of MUA-capped CdSe and MUA-capped ZnS sols were combined in a glass vial. Following the combination of the two nanocrystalline sols, 20 µl of 3% TNM solution was added to the CdSe/ZnS sol and the sample was shaken. Due to the faster kinetics of aggregation in the MUA-capped CdSe sample, since both NCs have the same capping ligand, the relative redox properties of Q-Q bond formation is the driving factor for the sol-gel synthesis. As the CdSe NCs form oxidative linkages more rapidly between particles, the CdSe forms a gel faster than ZnS (Figure 5.5). This results in the final gel having a top layer of ZnS and a bottom layer of CdSe gel.

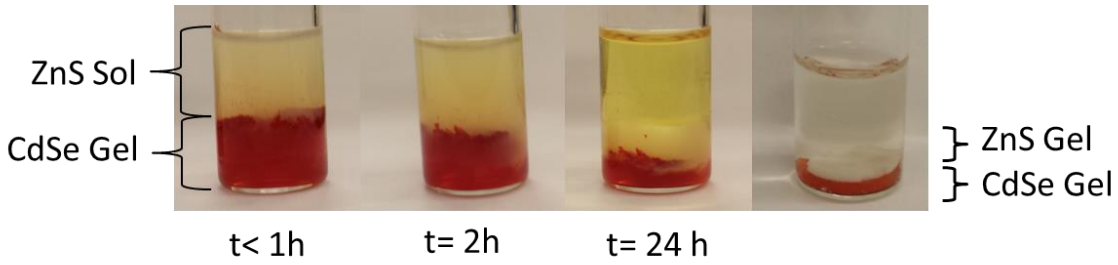

Figure 5.5. The sol-gel formation of the phase-segregated CdSe/ZnS co-gel over time, the yellow solution on top (most evident at t=24 h) is the by-product of the tetranitromethane oxidant. The final image follows the solvent-exchange to remove by-products.

Due to the two distinct aggregation events, it appears that as the CdSe gel settles out of solution, followed by the formation of the ZnS NC gel on top. The yellow supernatant is due to the nitroformate anion, a by-product of the oxidation of the surface thiolate ligand by the TNM.

Following the gelation process, the solvent was exchanged to remove the disulfide and oxidant by-products and the sample was dried using supercritical CO_2 extraction. Following the drying procedure PXRD was obtained (Figure 5.6), which showed the peaks for both *zb*-CdSe and *zb*-ZnS, confirming that the phase-segregated co-gel contains both of the constituent NC materials.

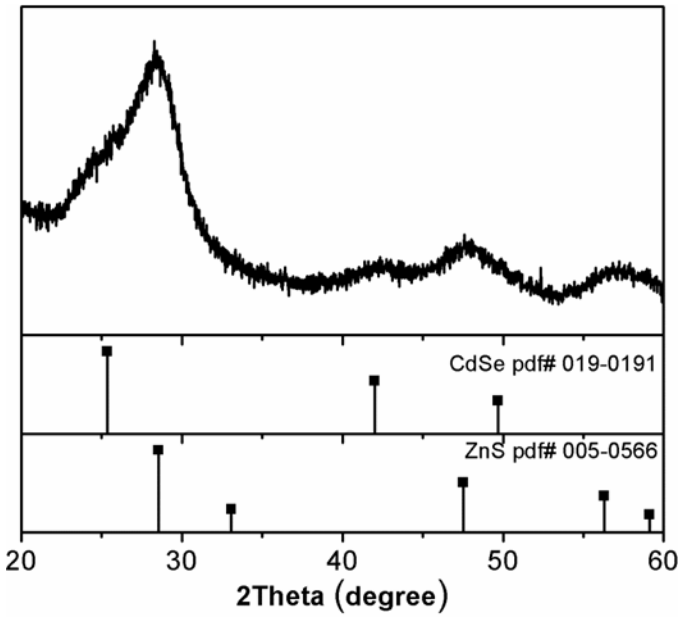

Figure 5.6. The PXRD spectrum for the phase-segregated co-gel with the pdf patterns for *zb*-CdSe and *zb*-ZnS shown below.

To further verify that this multicomponent phase-segregated co-gel was formed of two homogenous regions of metal chalcogenide materials, ICP-MS was performed on a large section of material, while EDAX from TEM was performed on several smaller sections of the sample (200-300 nm sections). Based on the ICP-MS data, the goal of a 1:1 mol ratio of Cd:Zn was achieved for the bulk sample, but on closer inspection of small areas using the TEM EDAX it becomes clear that the amounts of Cd and Zn vary wildly within the material (Table 5.1), as would be expected for a phase-segregated material.

Table 5.1. Atomic ratio of Cd:Zn using ICP-MS and small spot sizes (200-400 nm) in TEM EDAX analysis for the phase-segregated co-gel. Specimens for TEM were prepared by sonication of the bulk gel.

Gel Structure Type	**ICP-MS Atomic Ratio (Cd:Zn)**	**TEM EDS Spot 1 (Cd:Zn)**	**TEM EDS Spot 2 (Cd:Zn)**	**TEM EDS Spot 3 (Cd:Zn)**	**TEM EDS Spot 4 (Cd:Zn)**
Phase-Segregated Co-gel	1:1	0.2:1	0.8:1	1.4:1	0.7:1

The diffuse-reflectance measurements of the final aerogel powder were performed using a background of barium sulfate. The Kubelka-Munk approximation (Equation 2.32) for direct bandgap semiconductors was applied to give the onset of absorption for the material. As presented in Figure 5.7 the co-gel shows two distinct absorption onsets at 2.3 eV and 3.6 eV which are consistent with starting CdSe and ZnS NCs, meaning they maintained the quantum confinement affects in the resultant phase-segregated co-gels.

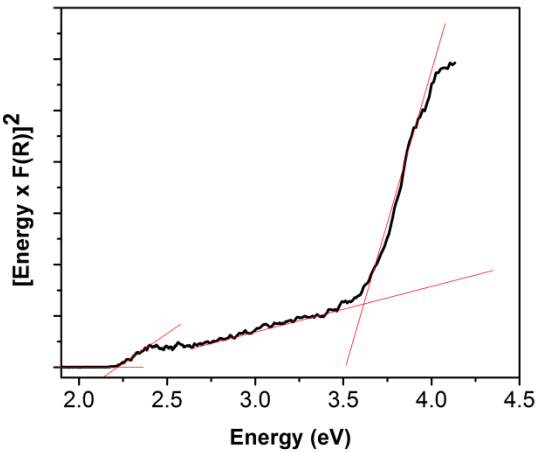

Figure 5.7. The diffuse-reflectance measurements of the phase-segregated CdSe/ZnS co-gel after the application of the Kubelka-Munk approximation for direct bandgap materials.

Finally the solution-phase emission data for the phase-segregated co-gels is shown in Figure 5.8. To prepare the sample, a suspension of the co-gel in methanol was sonicated for several minutes and placed in the photoluminescence spectrometer with an excitation wavelength of 300 nm. The emission for the phase-segregated co-gel shows two distinct peaks at 360 nm and 556 nm indicative of emission from the ZnS portion and the CdSe portion of the gel, respectively.

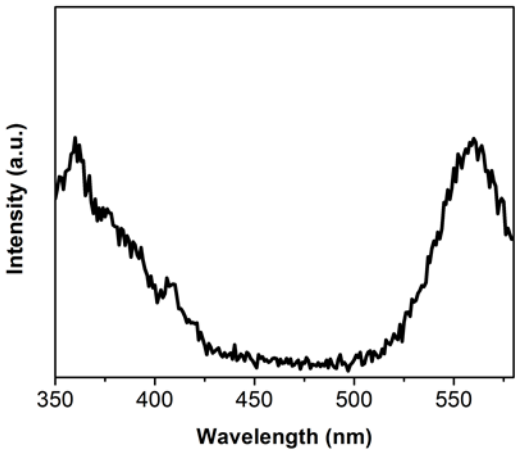

Figure 5.8. The PL emission data for the phase-segregated co-gel of CdSe/ZnS (λ_{exc}= 300 nm).

5.3.3 Intimately Mixed Gels

In an attempt to slow down the kinetics of aggregation for the CdSe NCs, to ensure they are on a similar time-scale of the MUA-capped ZnS NCs, the longer 16-mercaptohexadecanoic acid ligand was used to passivate the surface of the CdSe particles. Starting with a concentration for each nanocrystal sol (ZnS-MUA, CdSe-MHA) of 4.8 x 10^{-6} M, 1 ml of each sample was added to a glass vial, followed by the addition of 20 ul of 3% TNM (oxidant) solution. The final macroscopic gel (which forms within 4-5 hrs.) appears to be a well-mixed combination of the CdSe and ZnS nanocrystals (Figure 5.9). From the images of the final gel, there is no indication of phase-segregation.

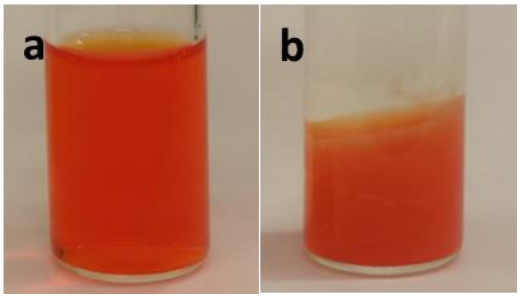

Figure 5.9. The sol-gel formation of the heterogeneous CdSe/ZnS co-gel over time a) 2 h and b) following the solvent exchange.

The color of the final wet gel (Figure 5.9), appears to be a mixture between the white-color seen in a ZnS wet gel (Figure 5.10a) and the darker-red color of the CdSe wet gel (Figure 5.10b), which is another indication of the good mixing in this multicomponent gel.

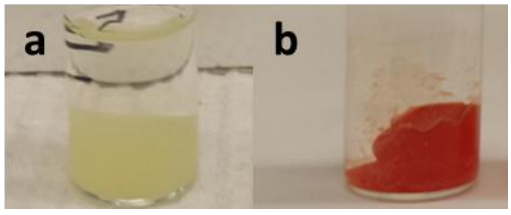

Figure 5.10. The wet gel for a) ZnS and b) CdSe.

The resultant composite gel was dried through supercritical CO_2 extraction to produce an aerogel. The aerogel sample was characterized by PXRD which indicated the peaks for both *zb*-CdSe and *zb*-ZnS were present in the gel (Figure 5.11).

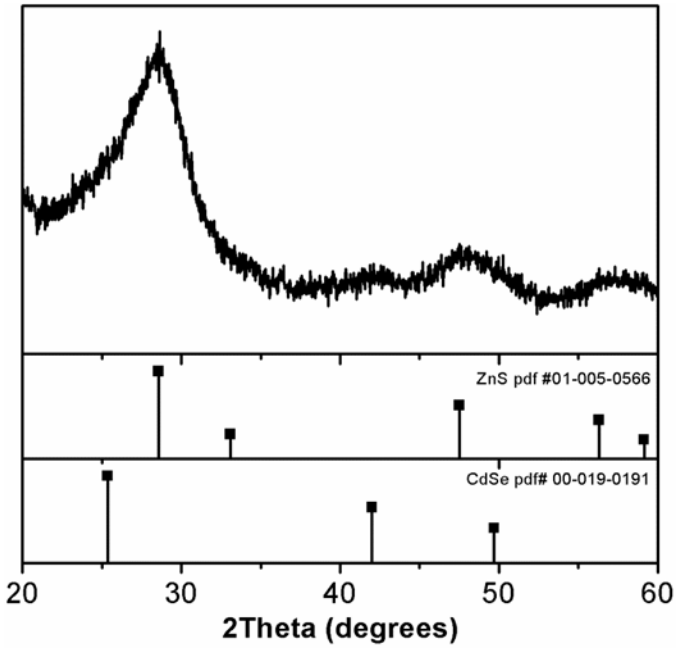

Figure 5.11. The PXRD spectrum for the intimately mixed co-gel with the pdf line diagrams for *zb*-CdSe and *zb*-ZnS shown below.

The diffuse-reflectance measurements for the intimately mixed co-gels show two peaks for absorption onset at 2.3 eV and 3.6 eV for the CdSe nanocrystal and the ZnS nanocrystal composites, respectively (Figure 5.12). This is similar to what was seen in the phase-segregated gels (Figure 5.7), indicating little change in the NCs after assembly into the intimately-mixed composite gel.

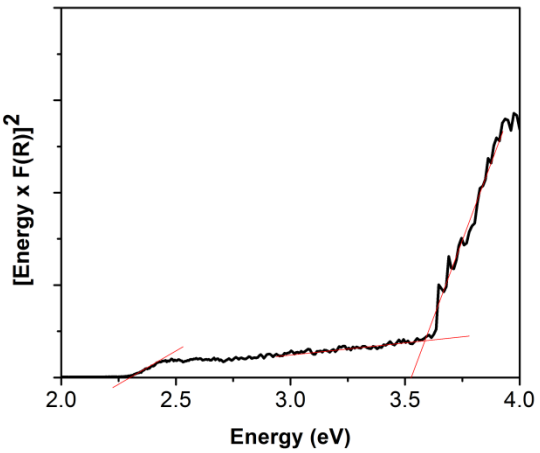

Figure 5.12. The diffuse-reflectance spectrum for the intimately mixed co-gels of CdSe/ZnS.

The solution-phase emission data for the intimately mixed co-gel was obtained as described for the phase-segregated sample. As shown in Figure 5.13 the emission for the intimately mixed co-gel shows two distinct peaks at 362 nm and 554 nm indicative of emission from the ZnS portion and the CdSe portion of the gel, respectively. Intriguingly, the emission from CdSe QDs appears to be quenched, the weak emission could be due to poor gel quality, an interaction between the components, or a combination of these two factors.

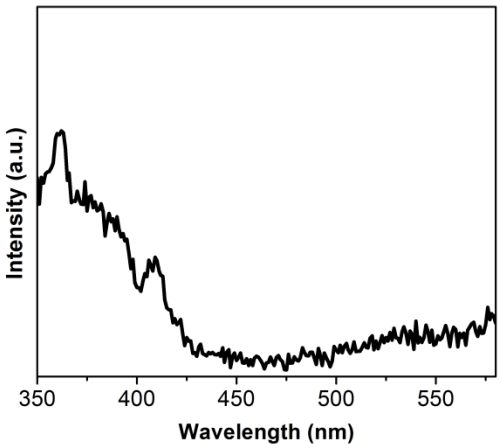

Figure 5.13. The photoluminescence emission data for the intimately mixed CdSe/ZnS co-gel composite (λ_{exc}=300 nm).

To verify that this multicomponent co-gel was a more intimately mixed composite of the CdSe and ZnS NCs, ICP-MS was performed on an entire gel section of material, while EDAX from TEM was performed on several small sections of the sample (Table 5.2), ICP-MS gave an overall ratio 1:1 Cd:Zn. The TEM/EDS mol ratio of Cd:Zn obtained in several areas of the sample was 1:1, as would be expected for a well-mixed system, although some regions did show unequal compositions (spot 2 Table 5.2). This is not surprising as there are kinetic distinctions between the two NCs, so perfect mixing is not expected (Figure 5.4).

Table 5.2. Atomic ratio of Cd:Zn using ICP-MS and small spot sizes (200-400 nm) in TEM EDAX analysis for the intimately mixed co-gel, specimen was prepared by sonication of the bulk gel.

Gel Structure Type	ICP-MS Atomic Ratio (Cd:Zn)	TEM EDS Spot 1 (Cd:Zn)	TEM EDS Spot 2 (Cd:Zn)	TEM EDS Spot 3 (Cd:Zn)	TEM EDS Spot 4 (Cd:Zn)
Intimately mixed Co-gel	1:1	1:1	0.7:1	1:1	1:1

5.4 Conclusion

An important concept in heterogeneous material design is the ability to control the spatial relationship between complimentary components in a solid state architecture using reliable synthetic methods, targeting precise compositions and controlling interfaces between the two-components in the hybrids. In our sol-gel synthesis, we have identified several levers to control the degree of mixing in composites, including oxidant concentration, crystal structure, chalcogenide redox properties and passivating ligand. Here we show that by adjusting the passivating ligand, the kinetics of aggregation can be tuned for dissimilar metal chalcogenides to synthesize a heterogeneous material that is either an intimate intermingling of the two components QD's or has significant phase-segregation.

CHAPTER 6: CONCLUSIONS AND PROSPECTUS

6.1 Conclusion

Metal chalcogenide nanocrystals are an important class of materials due to their interesting optical and electrical properties that can be controlled through particle size and shape, capping ligand, synthesis techniques and incorporation into heterostructures. The tunability of these materials, especially within the region of visible and near-IR energy, makes them important for electronic and optoelectronic applications such as field-effect transistors (FETs),[74-75]photodetectors,[76-77] light emitting diodes (LEDs),[78-79] photovoltaics[80-81] and radiation detectors.[20, 82] The incorporation of QDs into solid-state devices while enabling efficient carrier transport is a very important hurdle if MQ NCs are to be successfully used in the optoelectronics industry. Charge transport in thin films depends on the amount of electronic coupling between individual particles.[185] However, common synthetic techniques for producing high-quality NCs that are stable in solution usually employ long-chain passivating surface ligands, which increases the interparticle distances, decreasing the charge transport between neighboring particles.

Brock and co-workers have developed and utilized oxidative sol-gel methods to assemble metal chalcogenide NCs into gels, xerogels, aerogels and thin films.[38, 73, 101] NCs are connected through oxidation of the surface chalcogenide to form di- and/or polychalcogenide linkages, producing 2 and 3-D structures.[58]

This dissertation work is focused on achieving three main goals:

Aim I. Improve interfacial charge transport of a QD/porous silicon heterostructured device for radiation detection. The combination of metal chalcogenide QDs and pSi supports produces a potentially useful heteromaterial for radiation detection devices due to the large X-ray stopping power of PbS QDs combined with the charge transport potential of pSi.[20] Following the synthesis of anion-passivated PbS QDs and the exchange of the long chain oleic acid capping ligand with a shorter-chain 4-flurothiophenolate ligand, the QDs were spin-coated onto a pSi support that had been anodically etched to form pores with

a depth of 10 μm and diameter of 80-100 nm. To test whether the interface of anion-passivated PbS QDs and pSi would allow for charge transport in the device, an important factor in radiation detection, the heterostructured devices were first tested as photodiodes. I-V curves for the samples were measured with and without a light source. When comparing the samples with longer-chain passivating ligands on the PbS to the devices with the PbS QDs passivated with shorter-chain ligands, only the devices with short-chain passivating (4-fluorothiophenolate) ligands show any interaction with light. These results verify the importance of the interface between two materials in a heterostructured device, with the shorter-chain passivating ligand facilitating charge transport between the PbS QDs and the Si support. This suggests potential utility of these multicomponent devices in developing future direct conversion X-ray detection devices with a higher stopping power, allowing the patient X-ray dosage to be decreased.

Aim II. Develop synthetic levers for control over kinetics of aggregation for the oxidative gelation of MQ (M= Pb and Cd, Q= S, Se and Te) QDs. Due to the complexity of sustainable energy device production, it has become more important for multiple components to be integrated to work together synergistically. These multiple components must interact with each other, enabling charge transport properties in optoelectronic devices. Chapter 4 discusses an important step towards developing heterostructured metal chalcogenide gels by focusing on new synthetic levers for the control of the sol-gel synthesis process. CdQ NCs were synthesized using common high temperature arrested-precipitation techniques, to produce the wurtzite or zinc blende CdQ NCs. The NCs were then capped with a thiolate ligand. Using time resolved dynamic light scattering (TR-DLS) and nuclear magnetic spectroscopy (NMR), the kinetics of colloidal aggregation for the sol-gel synthesis of CdQ NCs were found to depend on the relative redox properties of Q (Q=S, Se and Te) and the structure (cubic vs. hexagonal). From TR-DLS studies, the increase in hydrodynamic radius as a function of time after the addition of oxidant (TNM) occurs in the order of the relative redox properties of the Q (S=0.48 V, Se=0.92 V and Te=1.14 V), with CdTe>CdSe>CdS. Interestingly, it appears that the native crystal structure of the QD (wurtzite vs. zinc blende) has a

considerable effect on the kinetics of the sol-gel synthesis with the zinc blende hydrodynamic radius growing slowly relative to wurtzite. The NMR studies following the addition of the oxidant (TNM), show the wurtzite CdS NCs lose the thiolate capping ligand faster than the *zb*-CdS, this can be seen by the rate of formation of the disulfide by-product in the NMR spectra. Further NMR studies showed that *zb*-CdS NCs have fewer passivating ligands/particle than the *w*-CdS NCs (*zb*-CdS NCs= 5.7 ligands/nm^2 and *w*-CdS NCs= 18.9 ligands/nm^2); this higher concentration of surface ligands can be attributed to higher surface facet energies on the *w*-CdS NCs, due to the polar nature of the crystal structure. Another feature of the *zb*-CdS NCs is possible surface anionic vacancies seen using electron paramagnetic resonance spectroscopy. Less surface chalcogenide sites to form polychalcogenide linkages between the particles could also explain the slower kinetics of aggregation for the *zb*-CdS NCs. These new tools, the relative redox properties of Q, and the crystal structure of the QDs, can be important levers in the toolbox of multicomponent nano-material design through sol-gel synthetic techniques.

Aim III. Synthesize multicomponent MQ materials of CdSe/ZnS with controlled phase segregation. The sol-gel synthetic technique can be used to make 2-and 3-D NC architectures, which would be a useful synthetic technique for incorporating two MQ QDs with complimentary functionalities into a heterostructured material. Several known synthetic levers can be used to control the kinetics of colloidal aggregation, including NC concentration, particle size, steric bulk of the passivating ligand, facet reactivity and the relative redox properties of the Q (Q=S, Se and Te).[54, 73, 83] One step in the sol-gel synthesis of these MQ particle constituents is the oxidation of the surface thiolate ligand. Using a bulkier ligand when incorporating two MQ NCs with differing Q (Q=S and Se), allows the tuning of the kinetics of colloidal aggregation. This gives a control lever that allows tailoring the final 3D structure of the co-gel.

6.2 Prospectus

This dissertation research has provided vital knowledge of the conditions and possible levers required to optimize the incorporation of NCs into multicomponent materials, either through sol-gel

synthesis or spin coating onto a support. Many optoelectronic, electronic and other device formats could be benefitted by the high surface area and unique quantum confinement affects inherent in these QDs if they can be combined in such a way as to enable facile charge transport. Furthermore this research has shown that relative redox properties of the anion (Q), the native crystal structure, and the sterics of the surface ligand can be utilized to affect the sol-gel synthesis for incorporation of different NC components into heterostructures.

Initial attempts to make radiation detection devices (Chapter 3) resulted in devices with poor performance due to the poor charge transport between the QDs in the devices. The synthesis methods required for these radiation detection devices meant that there was poor reproducibility between the samples. Therefore, a more reproducible synthetic techniques is required, possibly by switching from a porous Si support, to utilizing a thick film of PbS QDs, on-top of a Si wafer. However this dissertation work has introduced a successful strategy to improve charge transport properties between the QDs, by using short-chain thiolate ligands (4-fluorothiophenolate, solution-phase exchange) and anion-passivation on the NC surface, to make improved radiation detection devices. Further research should focus on surface-passivation of the PbS QDs, including monitoring device improvement with even shorter-chain passivating ligands, such as thioglycolic acid. Film improvement will reduce likely aggregated regions in the devices, which will allow improved interfacial contacts with the electrodes. A larger NC loading has also been shown to increase electron transport.[186]

The poor charge transport between QD NCs has led us to develop an oxidative sol-gel synthesis to incorporate particles into a 3D matrix.[38] To incorporate these NCs with complimentary functionalities it is important to study different possible levers for the control of the kinetics of aggregation. Now that these surface affects have been shown to have control of the kinetics it is important to the future research should focus on the effect of the cation (M) on the sol-gel synthesis. Since one of the important steps determined in the sol-gel synthesis is the solvation of the metal cation to expose chalcogenide surface

sites, it is likely that cation solvation affects may contribute to the kinetics of assembly.[58] Since particle shapes are driven by the differences in surface energies, which favor growth along specific facets, it will also be important to study if the kinetics of colloidal aggregation can be adjusted based on particle shape. These different NC shape effects on the kinetics of colloidal aggregation can be studied through TR-DLS.

The oxidative sol-gel synthesis strategy can be extended to other chalcogenide NC systems to develop multicomponent materials. Multicomponent materials are of particular interest because of their ability to combine several materials with complimentary functionalities (e.g. n-type and p-type constituent materials) into one device or thin film. It would make this synthetic technique desirable for developing solar energy devices. This research has highlighted the ability to tune macroscopic properties of the final gel, using our oxidative sol-gel synthesis, through synthetic levers such as concentration (oxidant and NC), sterics of the capping ligand, particle size and Q. Future studies can utilize these synthetic levers for thin film device formation. These early attempts to make multicomponent gels were performed in the solution phase, but for device incorporation it is important that future work focuses on thin film deposition techniques.

REFERENCES

1. Bawendi, M. G.; Steigerwald, M. L.; Brus, L. E., The quantum mechanics of larger semiconductor clusters. *Annual Review of Physical Chemistry* **1990,** *41* (1), 477-496.

2. Klimov, V. I., *Nanocrystal Quantum Dots*. CRC Press: Boca Raton, 2010.

3. Takagahara, T.; Takeda, K., Theory of the quantum confinement effect on excitons in quantum dots of indirect-gap materials. *Physical Review B* **1992,** *46* (23), 15578-15581.

4. Yarema, M.; Pichler, S.; Sytnyk, M.; Seyrkammer, R.; Lechner, R. T.; Fritz-Popovski, G.; Jarzab, D.; Szendrei, K.; Resel, R.; Korovyanko, O.; Loi, M. A.; Paris, O.; Hesser, G.; Heiss, W., Infrared emitting and photoconducting colloidal silver chalcogenide nanocrystal quantum dots from a silylamide-promoted synthesis. *ACS Nano* **2011,** *5* (5), 3758-65.

5. Xie, R.; Zhang, J.; Zhao, F.; Yang, W.; Peng, X., Synthesis of monodisperse, highly emissive, and size-tunable Cd_3P_2 nanocrystals. *Chemistry of Materials* **2010,** *22* (13), 3820-3822.

6. Harris, D. K.; Allen, P. M.; Han, H.-S.; Walker, B. J.; Lee, J.; Bawendi, M. G., Synthesis of cadmium arsenide quantum dots luminescent in the infrared. *Journal of the American Chemical Society* **2011,** *133* (13), 4676-4679.

7. Mahamuni, S.; Khosravi, A. A.; Kundu, M.; Kshirsagar, A.; Bedekar, A.; Avasare, D. B.; Singh, P.; Kulkarni, S. K., Thiophenol-capped ZnS quantum dots. *Journal of Applied Physics* **1993,** *73* (10), 5237-5240.

8. Jun, Y.-W.; Koo, J.-E.; Cheon, J., One-step synthesis of size tuned zinc selenide quantum dots a temperature controlled molecular precursor approach. *Chemical Communications* **2000,** (14), 1243-1244.

9. Jun, Y.-W.; Choi, C.-S.; Cheon, J., Size and shape controlled ZnTe nanocrystals with quantum confinement effect. *Chemical Communications* **2001,** (1), 101-102.

10. Murray, C. B.; Norris, D. J.; Bawendi, M. G., Synthesis and characterization of nearly monodisperse CdE (E = sulfur, selenium, tellurium) semiconductor nanocrystallites. *Journal of the American Chemical Society* **1993,** *115* (19), 8706-8715.

11. Beberwyck, B. J.; Alivisatos, A. P., Ion exchange synthesis of III-V nanocrystals. *Journal of the American Chemical Society* **2012,** *134* (49), 19977-80.

12. Battaglia, D.; Peng, X., Formation of high quality InP and InAs nanocrystals in a noncoordinating solvent. *Nano Letters* **2002,** *2* (9), 1027-1030.

13. Yarema, M.; Kovalenko, M. V., Colloidal synthesis of InSb nanocrystals with controlled polymorphism using indium and antimony amides. *Chemistry of Materials* **2013,** *25* (9), 1788-1792.

14. Hines, M. A.; Scholes, G. D., Colloidal PbS nanocrystals with size-tunable near-infrared emission: observation of post-synthesis self-narrowing of the particle size distribution. *Advanced Materials* **2003,** *15* (21), 1844-1849.

15. Talapin, D. V.; Murray, C. B., PbSe nanocrystal solids for n- and p-channel thin film field-effect transistors. *Science* **2005,** *310* (5745), 86-89.

16. Urban, J. J.; Talapin, D. V.; Shevchenko, E. V.; Murray, C. B., Self-assembly of PbTe quantum dots into nanocrystal superlattices and glassy films. *Journal of the American Chemical Society* **2006,** *128* (10), 3248-55.

17. Qian, L.; Zheng, Y.; Xue, J.; Holloway, P. H., Stable and efficient quantum-dot light-emitting diodes based on solution-processed multilayer structures. *Nature Photonic* **2011,** *5* (9), 543-548.

18. McDonald, S. A.; Konstantatos, G.; Zhang, S.; Cyr, P. W.; Klem, E. J. D.; Levina, L.; Sargent, E. H., Solution-processed PbS quantum dot infrared photodetectors and photovoltaics. *Nature Materials* **2005,** *4* (2), 138-142.

19. Ip, A. H.; Thon, S. M.; Hoogland, S.; Voznyy, O.; Zhitomirsky, D.; Debnath, R.; Levina, L.; Rollny, L. R.; Carey, G. H.; Fischer, A.; Kemp, K. W.; Kramer, I. J.; Ning, Z.; Labelle, A. J.; Chou, K. W.; Amassian, A.; Sargent, E. H., Hybrid passivated colloidal quantum dot solids. *Nature Nanomaterials* **2012,** *7* (9), 577-582.

20. Urdaneta, M.; Stepanov, P.; Weinberg, I. N.; Pala, I. R.; Brock, S., Porous silicon-based quantum dot broad spectrum radiation detector. *Journal of instrumentation* **2011,** *6*, C01027.

21. Alivisatos, A. P., Perspectives on the physical chemistry of semiconductor nanocrystals. *The Journal of Physical Chemistry* **1996,** *100* (31), 13226-13239.

22. Ashoori, R. C., Electrons in artificial atoms. *Nature* **1996,** *379* (6564), 413-419.

23. Reimann, S. M.; Manninen, M., Electronic structure of quantum dots. *Reviews of Modern Physics* **2002,** *74* (4), 1283-1342.

24. Zhang, J. Z., *Optical Properties and Spectroscopy of Nanomaterials*. WSPC: Singapore, US, 2009.

25. Philipp, H. R.; Ehrenreich, H., Optical properties of semiconductors. *Physical Review* **1963,** *129* (4), 1550-1560.

26. Murray, C. B.; Kagan, C. R.; Bawendi, M. G., Synthesis and characterization of monodisperse nanocrystals and close-packed nanocrystal assemblies. *Annual Review of Materials Science* **2000,** *30* (1), 545-610.

27. Qu, L.; Peng, Z. A.; Peng, X., Alternative routes toward high quality CdSe nanocrystals. *Nano Letters* **2001,** *1* (6), 333-337.

28. Yin, Y.; Alivisatos, A. P., Colloidal nanocrystal synthesis and the organic-inorganic interface. *Nature* **2005,** *437* (7059), 664-670.

29. LaMer, V. K.; Dinegar, R. H., Theory, production and mechanism of formation of monodispersed hydrosols. *Journal of the American Chemical Society* **1950,** *72* (11), 4847-4854.

30. Rahman, G. M. A.; Guldi, D. M.; Zambon, E.; Pasquato, L.; Tagmatarchis, N.; Prato, M., Dispersable carbon nanotube/gold nanohybrids: evidence for strong electronic interactions. *Small* **2005,** *1* (5), 527-530.

31. Peng, X., Mechanisms for the shape-control and shape-evolution of colloidal semiconductor nanocrystals. *Advanced Materials* **2003,** *15* (5), 459-463.

32. Murray, C. B.; Sun, S.; Gaschler, W.; Doyle, H.; Betley, T. A.; Kagan, C. R., Colloidal synthesis of nanocrystals and nanocrystal superlattices. *IBM Journal of Research and Development.* **2001,** *45* (1), 47-56.

33. Peng, X.; Manna, L.; Yang, W.; Wickham, J.; Scher, E.; Kadavanich, A.; Alivisatos, A. P., Shape control of CdSe nanocrystals. *Nature* **2000,** *404* (6773), 59-61.

34. Peng, X.; Wickham, J.; Alivisatos, A. P., Kinetics of II-VI and III-V colloidal semiconductor nanocrystal growth: "Focusing" of size distributions. *Journal of the American Chemical Society* **1998,** *120* (21), 5343-5344.

35. Li, L.; Qing-Sheng, W.; Ya-Ping, D.; Pei-Ming, W., Control synthesis of semiconductor ZnSe quasi-nanospheres by reverse micelles soft template. *Materials Letters* **2005,** *59* (13), 1623-1626.

36. Capek, I., Preparation of metal nanoparticles in water-in-oil (w/o) microemulsions. *Advances in Colloid and Interface Science* **2004,** *110* (1–2), 49-74.

37. Brinker, C. J.; Scherer, G. W., *Sol-Gel science: The physics and chemistry of sol-gel processing*. Elsevier Science: 2013.

38. Mohanan, J. L.; Arachchige, I. U.; Brock, S. L., Porous semiconductor chalcogenide aerogels. *Science* **2005,** *307* (5708), 397-400.

39. Meakin, P., Formation of fractal clusters and networks by irreversible diffusion-limited aggregation. *Physical Review Letters* **1983,** *51* (13), 1119-1122.

40. Witten, T. A.; Sander, L. M., Diffusion-limited aggregation, a kinetic critical phenomenon. *Physical Review Letters* **1981,** *47* (19), 1400-1403.

41. Lin, M. Y.; Lindsay, H. M.; Weitz, D. A.; Ball, R. C.; Klein, R.; Meakin, P., Universality in colloid aggregation. *Nature* **1989,** *339* (6223), 360-362.

42. Umbach, P.; Georgalis, Y.; Saenger, W., Time-resolved small-angle static light scattering on lysozyme during nucleation and growth. *Journal of the American Chemical Society* **1998,** *120* (10), 2382-2390.

43. Dongen, P. G. J. V.; Ernst, M. H., Cluster size distribution in irreversible aggregation at large times. *Journal of Physics A: Mathematical and General* **1985,** *18* (14), 2779.

44. Van Dongen, P. G. J.; Ernst, M. H., Dynamic scaling in the kinetics of clustering. *Physical Review Letters* **1985,** *54* (13), 1396-1399.

45. Smoluchowski, M., Drei Vortrage uber Diffusion, Brownsche Bewegung und Koagulation von Kolloidteilchen. *Physik. Zeit.* **1916,** *17*, 557-585.

46. Smoluchowski, M. V., Versuch einer mathematischen theorie der koagulationskinetik kolloider lösungen. *Zeitschrift fuer physikalische Chemie* **1917,** *92*, 129-168.

47. Yang, J.; Choi, M. K.; Kim, D.-H.; Hyeon, T., Designed assembly and integration of colloidal nanocrystals for device applications. *Advanced Materials* **2016,** *28* (6), 1176-1207.

48. Talapin, D. V.; Lee, J.-S.; Kovalenko, M. V.; Shevchenko, E. V., Prospects of colloidal nanocrystals for electronic and optoelectronic applications. *Chemical Reviews* **2010,** *110* (1), 389-458.

49. Kagan, C. R.; Lifshitz, E.; Sargent, E. H.; Talapin, D. V., Building devices from colloidal quantum dots. *Science* **2016,** *353* (6302).

50. Kagan, C. R.; Murray, C. B., Charge transport in strongly coupled quantum dot solids. *Nature Nanomaterials* **2015,** *10* (12), 1013-1026.

51. Gacoin, T.; Lahlil, K.; Larregaray, P.; Boilot, J. P., Transformation of CdS colloids: Sols, gels, and precipitates. *The Journal of Physical Chemistry B* **2001,** *105* (42), 10228-10235.

52. Arachchige, I. U.; Brock, S. L., Sol−Gel assembly of CdSe nanoparticles to form porous aerogel networks. *Journal of the American Chemical Society* **2006,** *128* (24), 7964-7971.

53. Yu, H.; Brock, S. L., Effects of nanoparticle shape on the morphology and properties of porous CdSe assemblies (aerogels). *ACS Nano* **2008,** *2* (8), 1563-1570.

54. Yao, Q.; Brock, S. L., Porous CdTe nanocrystal assemblies: ligation effects on the gelation process and the properties of resultant aerogels. *Inorganic Chemistry* **2011,** *50* (20), 9985-9992.

55. Kalebaila, K. K.; Brock, S. L., Lead selenide nanostructured aerogels and xerogels. *Zeitschrift für anorganische und allgemeine Chemie* **2012,** *638* (15), 2598-2603.

56. Ganguly, S.; Brock, S. L., Toward nanostructured thermoelectrics: synthesis and characterization of lead telluride gels and aerogels. *Journal of Materials Chemistry* **2011,** *21* (24), 8800-8806.

57. Ganguly, S.; Zhou, C.; Morelli, D.; Sakamoto, J.; Brock, S. L., Synthesis and characterization of telluride aerogels: effect of gelation on thermoelectric performance of Bi_2Te_3 and $Bi_{2-x}Sb_xTe_3$ nanostructures. *The Journal of Physical Chemistry C* **2012,** *116* (33), 17431-17439.

58. Pala, I. R.; Arachchige, I. U.; Georgiev, D. G.; Brock, S. L., Reversible gelation of II–VI nanocrystals: The nature of interparticle bonding and the origin of nanocrystal photochemical instability. *Angewandte Chemie International Edition* **2010,** *49* (21), 3661-3665.

59. Rakovich, Y. P.; Volkov, Y.; Sapra, S.; Susha, A. S.; Döblinger, M.; Donegan, J. F.; Rogach, A. L., CdTe nanowire networks: Fast self-assembly in solution, internal structure, and optical properties. *The Journal of Physical Chemistry C* **2007,** *111* (51), 18927-18931.

60. Zhong, X.; Han, M.; Dong, Z.; White, T. J.; Knoll, W., Composition-Tunable $Zn_xCd_{1-x}Se$ nanocrystals with high luminescence and stability. *Journal of the American Chemical Society* **2003,** *125* (28), 8589-8594.

61. Jang, E.; Jun, S.; Pu, L., High quality CdSeS nanocrystals synthesized by facile single injection process and their electroluminescence. *Chemical Communications* **2003,** (24), 2964-2965.

62. Micic, O. I.; Sprague, J. R.; Curtis, C. J.; Jones, K. M.; Machol, J. L.; Nozik, A. J.; Giessen, H.; Fluegel, B.; Mohs, G.; Peyghambarian, N., Synthesis and characterization of InP, GaP, and $GaInP_2$ quantum dots. *The Journal of Physical Chemistry* **1995,** *99* (19), 7754-7759.

63. Kortan, A. R.; Hull, R.; Opila, R. L.; Bawendi, M. G.; Steigerwald, M. L.; Carroll, P. J.; Brus, L. E., Nucleation and growth of cadmium selendie on zinc sulfide quantum crystallite seeds, and vice versa, in inverse micelle media. *Journal of the American Chemical Society* **1990,** *112* (4), 1327-1332.

64. Hoener, C. F.; Allan, K. A.; Bard, A. J.; Campion, A.; Fox, M. A.; Mallouk, T. E.; Webber, S. E.; White, J. M., Demonstration of a shell-core structure in layered cadmium selenide-zinc selenide small particles by x-ray photoelectron and Auger spectroscopies. *The Journal of Physical Chemistry* **1992,** *96* (9), 3812-3817.

65. Danek, M.; Jensen, K. F.; Murray, C. B.; Bawendi, M. G., Synthesis of luminescent thin-film CdSe/ZnSe quantum dot composites using CdSe quantum dots passivated with an overlayer of ZnSe. *Chemistry of Materials* **1996,** *8* (1), 173-180.

66. Pietryga, J. M.; Park, Y.-S.; Lim, J.; Fidler, A. F.; Bae, W. K.; Brovelli, S.; Klimov, V. I., Spectroscopic and device aspects of nanocrystal quantum dots. *Chemical Reviews* **2016,** *116* (18), 10513-10622.

67. Amirav, L.; Alivisatos, A. P., Photocatalytic hydrogen production with tunable nanorod heterostructures. *The Journal of Physical Chemistry Letters* **2010,** *1* (7), 1051-1054.

68. Berr, M. J.; Vaneski, A.; Mauser, C.; Fischbach, S.; Susha, A. S.; Rogach, A. L.; Jackel, F.; Feldmann, J., Delayed photoelectron transfer in Pt-decorated CdS nanorods under hydrogen generation conditions. *Small* **2012,** *8* (2), 291-7.

69. Wu, K.; Zhu, H.; Liu, Z.; Rodríguez-Córdoba, W.; Lian, T., Ultrafast charge separation and long-lived charge separated state in photocatalytic CdS–Pt nanorod heterostructures. *Journal of the American Chemical Society* **2012,** *134* (25), 10337-10340.

70. Bao, N.; Shen, L.; Takata, T.; Domen, K., Self-Templated synthesis of nanoporous CdS nanostructures for highly efficient photocatalytic hydrogen production under visible light. *Chemistry of Materials* **2008,** *20* (1), 110-117.

71. Zhu, H.; Song, N.; Lv, H.; Hill, C. L.; Lian, T., Near unity quantum yield of light-driven redox mediator reduction and efficient H_2 generation using colloidal nanorod heterostructures. *Journal of the American Chemical Society* **2012,** *134* (28), 11701-11708.

72. Razgoniaeva, N.; Moroz, P.; Lambright, S.; Zamkov, M., Photocatalytic applications of colloidal heterostructured nanocrystals: What's next? *The Journal of Physical Chemistry Letters* **2015,** *6* (21), 4352-4359.

73. Korala, L.; Wang, Z.; Liu, Y.; Maldonado, S.; Brock, S. L., Uniform thin films of CdSe and CdSe(ZnS) core(shell) quantum dots by sol–gel assembly: Enabling photoelectrochemical characterization and electronic applications. *ACS Nano* **2013,** *7* (2), 1215-1223.

74. Yu, D.; Wang, C.; Guyot-Sionnest, P., n-Type conducting CdSe nanocrystal solids. *Science* **2003,** *300* (5623), 1277-80.

75. Ridley, B. A.; Nivi, B.; Jacobson, J. M., All-Inorganic field effect transistors fabricated by printing. *Science* **1999,** *286* (5440), 746-749.

76. Oertel, D. C.; Bawendi, M. G.; Arango, A. C.; Bulović, V., Photodetectors based on treated CdSe quantum-dot films. *Applied Physics Letters* **2005,** *87* (21), 213505.

77. Konstantatos, G.; Howard, I.; Fischer, A.; Hoogland, S.; Clifford, J.; Klem, E.; Levina, L.; Sargent, E. H., Ultrasensitive solution-cast quantum dot photodetectors. *Nature* **2006,** *442* (7099), 180-183.

78. Colvin, V. L.; Schlamp, M. C.; Alivisatos, A. P., Light-emitting diodes made from cadmium selenide nanocrystals and a semiconducting polymer. *Nature* **1994,** *370* (6488), 354-357.

79. Coe, S.; Woo, W. K.; Bawendi, M.; Bulovic, V., Electroluminescence from single monolayers of nanocrystals in molecular organic devices. *Nature* **2002,** *420* (6917), 800-3.

80. Gur, I.; Fromer, N. A.; Geier, M. L.; Alivisatos, A. P., Air-Stable all-inorganic nanocrystal solar cells processed from solution. *Science* **2005,** *310* (5747), 462-465.

81. Huynh, W. U.; Dittmer, J. J.; Alivisatos, A. P., Hybrid nanorod-polymer solar cells. *Science* **2002,** *295* (5564), 2425-2427.

82. Urdaneta, M.; Stepanov, P.; Weinberg, I.; Pala, I.; Brock, S., *Quantum Dot Composite Radiation Detectors*. InTech: 2011.

83. Korala, L.; Brock, S. L., Aggregation kinetics of metal chalcogenide nanocrystals: generation of transparent CdSe (ZnS) core (shell) gels. *The Journal of Physical Chemistry C* **2012,** *116* (32), 17110-17117.

84. Bouroushian, M., *Electrochemistry of Metal Chalcogenides*. Springer Berlin Heidelberg: 2010.

85. Bornside, D. E.; Macosko, C. W.; Scriven, L. E., On the modeling of spin coating. *Journal of Imaging Technology* **1987,** *13* (4), 122-130.

86. Emslie, A. G.; Bonner, F. T.; Peck, L. G., Flow of a viscous liquid on a rotating disk. *Journal of Applied Physics* **1958,** *29* (5), 858-862.

87. Bornside, D. E.; Macosko, C. W.; Scriven, L. E., Spin coating of a PMMA/Chlorobenzene solution. *Journal of The Electrochemical Society* **1991,** *138* (1), 317-320.

88. Ohring, M., *Materials science of thin films*. Academic Press: 1992; p 974.

89. Föll, H.; Christophersen, M.; Carstensen, J.; Hasse, G., Formation and application of porous silicon. *Materials Science and Engineering: R: Reports* **2002,** *39* (4), 93-141.

90. Parkhutik, V., Porous silicon—mechanisms of growth and applications. *Solid-State Electronics* **1999,** *43* (6), 1121-1141.

91. Lehmann, V.; Stengl, R.; Luigart, A., On the morphology and the electrochemical formation mechanism of mesoporous silicon. *Materials Science and Engineering: B* **2000,** *69–70*, 11-22.

92. Bisi, O.; Ossicini, S.; Pavesi, L., Porous silicon: a quantum sponge structure for silicon based optoelectronics. *Surface Science Reports* **2000,** *38* (1–3), 1-126.

93. Richter, A.; Steiner, P.; Kozlowski, F.; Lang, W., Current-induced light emission from a porous silicon device. *IEEE Electron Device Letters* **1991,** *12* (12), 691-692.

94. Tsai, C.; Li, K. H.; Campbell, J. C.; Tasch, A., Photodetectors fabricated from rapid-thermal-oxidized porous Si. *Applied Physics Letters* **1993,** *62* (22), 2818-2820.

95. Yablonovitch, E., Inhibited spontaneous emission in solid-state physics and electronics. *Physical Review Letters* **1987,** *58* (20), 2059-2062.

96. Beale, M. I. J.; Benjamin, J. D.; Uren, M. J.; Chew, N. G.; Cullis, A. G., An experimental and theoretical study of the formation and microstructure of porous silicon. *Journal of Crystal Growth* **1985,** *73* (3), 622-636.

97. Lehmann, V.; Gösele, U., Porous silicon formation: A quantum wire effect. *Applied Physics Letters* **1991,** *58* (8), 856-858.

98. Pierre, A. C.; Pajonk, G. M., Chemistry of aerogels and their applications. *Chem Rev* **2002,** *102* (11), 4243-65.

99. Mohanan, J. L.; Brock, S. L., A new addition to the aerogel community: unsupported CdS aerogels with tunable optical properties. *Journal of Non-Crystalline Solids* **2004,** *350*, 1-8.

100. Arachchige, I. U.; Mohanan, J. L.; Brock, S. L., Sol−Gel processing of semiconducting metal chalcogenide xerogels: influence of dimensionality on quantum confinement effects in a nanoparticle network. *Chemistry of Materials* **2005,** *17* (26), 6644-6650.

101. Arachchige, I. U.; Brock, S. L., Sol–Gel methods for the assembly of metal chalcogenide quantum dots. *Accounts of Chemical Research* **2007,** *40* (9), 801-809.

102. Arachchige, I. U.; Brock, S. L., Highly luminescent quantum-dot monoliths. *Journal of the American Chemical Society* **2007,** *129* (7), 1840-1841.

103. Yu, H.; Bellair, R.; Kannan, R. M.; Brock, S. L., Engineering strength, porosity, and emission intensity of nanostructured CdSe networks by altering the building-block shape. *Journal of the American Chemical Society* **2008,** *130* (15), 5054-5055.

104. Yu, H.; Liu, Y.; Brock, S. L., Tuning the optical band gap of quantum dot assemblies by varying network density. *ACS Nano* **2009,** *3* (7), 2000-2006.

105. Malier, L.; Boilot, J. P.; Gacoin, T., Sulfide gels and films: Products of non-oxide gelation. *Journal of Sol-Gel Science and Technology* **1998,** *13* (1), 61-64.

106. Berne, B. J.; Pecora, R., *Dynamic Light Scattering: With Applications to Chemistry, Biology, and Physics*. Dover Publications: 2000.

107. Xu, R., *Particle Characterization: Light Scattering Methods*. Kluwer: New York, 2002.

108. Koppel, D. E., Analysis of Macromolecular Polydispersity in Intensity Correlation Spectroscopy: The Method of Cumulants. *The Journal of Chemical Physics* **1972,** *57* (11), 4814-4820.

109. Brown, W., *Dynamic Light Scattering: The Method and Some Applications*. Clarendon Press: Oxford, 1993.

110. Chu, B., Laser light scattering. *Annual Review of Physical Chemistry* **1970,** *21* (1), 145-174.

111. Pecharsky, V. K.; Zavalij, P. Y., *Fundamentals of Powder Diffraction and Structural Characterization of Materials*. Springer US: 2009.

112. Patterson, A. L., The Scherrer formula for x-ray particle size determination. *Physical Review* **1939,** *56* (10), 978-982.

113. Lambert, J. B.; Mazzola, E. P., *Nuclear Magnetic Resonance Spectroscopy: An Introduction to Principles, Applications and Experimental Methods*. Pearson Education Inc. : New Jersey, 2004.

114. Harris, R. K., *Nuclear magnetic resonance spectroscopy*. John Wiley and Sons Inc.,New York, NY; None: 1986; p Medium: X; Size: Pages: 272.

115. Schwalbe, H., Applied NMR spectroscopy for chemists and life scientists. *Angewandte Chemie International Edition* **2014,** *53* (49), 13324-13324.

116. Rieger, P. H., *Electron spin resonance: analysis and interpretation*. Royal Society of Chemistry: Cambridge, 2007.

117. Goodhew, P. J.; Humphreys, J.; Beanland, R., *Electron Microscopy and Analysis*. Taylor & Francis: London, 2001.

118. Brus, L., Electronic wave functions in semiconductor clusters: experiment and theory. *The Journal of Physical Chemistry* **1986,** *90* (12), 2555-2560.

119. Vargas, W. E.; Niklasson, G. A., Applicability conditions of the Kubelka–Munk theory. *Applied Optics* **1997,** *36* (22), 5580-5586.

120. Yang, L.; Kruse, B., Revised Kubelka–Munk theory. I. Theory and application. J*ournal of the Optical Society of America A* **2004,** *21* (10), 1933-1941.

121. Hunt, R. W. G.; Pointer, M. R., *Measuring Colour*. John Wiley and Sons, Ltd: 2011.

122. Nobbs, J. H., Kubelka—Munk theory and the prediction of reflectance. *Review of Progress in Coloration and Related Topics* **1985,** *15* (1), 66-75.

123. Stuart, B. H., *Infrared Spectroscopy: Fundamentals and Applications*. Wiley: Hoboken, 2004.

124. *Principles of Fluorescence Spectroscopy*. Springer US: New York, 2006.

125. Lim, J.; Bae, W. K.; Kwak, J.; Lee, S.; Lee, C.; Char, K., Perspective on synthesis, device structures, and printing processes for quantum dot displays. *Optical Materials Express* **2012,** *2* (5), 594-628.

126. Walls, J. M.; SMith, R., *Surface Science Techniques*. Elsevier: New York, 1994.

127. van der Heide, P., *X-ray Photoelectron Spectroscopy : An introduction to Principles and Practices (1)*. Wiley: Hoboken, US, 2011.

128. Kasap, S. O.; Rowlands, J. A., Direct-conversion flat-panel X-ray image detectors. *IEE Proceedings - Circuits, Devices and Systems* **2002,** *149* (2), 85-96.

129. Murty, R. C., Effective atomic numbers of heterogeneous materials. *Nature* **1965,** *207* (4995), 398-399.

130. Jackson, D. F.; Hawkes, D. J., X-ray attenuation coefficients of elements and mixtures. *Physics Reports* **1981,** *70* (3), 169-233.

131. Tang, J.; Kemp, K. W.; Hoogland, S.; Jeong, K. S.; Liu, H.; Levina, L.; Furukawa, M.; Wang, X.; Debnath, R.; Cha, D.; Chou, K. W.; Fischer, A.; Amassian, A.; Asbury, J. B.; Sargent, E. H., Colloidal-quantum-dot photovoltaics using atomic-ligand passivation. *Nature Materials* **2011,** *10* (10), 765-771.

132. Klem, E. J. D.; Shukla, H.; Hinds, S.; MacNeil, D. D.; Levina, L.; Sargent, E. H., Impact of dithiol treatment and air annealing on the conductivity, mobility, and hole density in PbS colloidal quantum dot solids. *Applied Physics Letters* **2008,** *92* (21), 212105.

133. Luther, J. M.; Law, M.; Beard, M. C.; Song, Q.; Reese, M. O.; Ellingson, R. J.; Nozik, A. J., Schottky solar cells based on colloidal nanocrystal films. *Nano Letters* **2008,** *8* (10), 3488-92.

134. Koleilat, G. I.; Levina, L.; Shukla, H.; Myrskog, S. H.; Hinds, S.; Pattantyus-Abraham, A. G.; Sargent, E. H., Efficient, stable infrared photovoltaics based on solution-cast colloidal quantum dots. *ACS Nano* **2008,** *2* (5), 833-40.

135. Pattantyus-Abraham, A. G.; Kramer, I. J.; Barkhouse, A. R.; Wang, X.; Konstantatos, G.; Debnath, R.; Levina, L.; Raabe, I.; Nazeeruddin, M. K.; Gratzel, M.; Sargent, E. H., Depleted-heterojunction colloidal quantum dot solar cells. *ACS Nano* **2010,** *4* (6), 3374-80.

136. Liu, Y.; Tolentino, J.; Gibbs, M.; Ihly, R.; Perkins, C. L.; Liu, Y.; Crawford, N.; Hemminger, J. C.; Law, M., PbSe Quantum dot field-effect transistors with air-stable electron mobilities above 7 $cm^2 V^{-1} s^{-1}$. *Nano Letters* **2013,** *13* (4), 1578-1587.

137. Mashford, B. S.; Stevenson, M.; Popovic, Z.; Hamilton, C.; Zhou, Z.; Breen, C.; Steckel, J.; Bulovic, V.; Bawendi, M.; Coe-Sullivan, S.; Kazlas, P. T., High-efficiency quantum-dot light-emitting devices with enhanced charge injection. *Nature Photonics* **2013,** *7* (5), 407-412.

138. Sun, Q.; Wang, Y. A.; Li, L. S.; Wang, D.; Zhu, T.; Xu, J.; Yang, C.; Li, Y., Bright, multicoloured light-emitting diodes based on quantum dots. *Nature Photonics* **2007,** *1* (12), 717-722.

139. Campbell, I. H.; Crone, B. K., Quantum-Dot/Organic semiconductor composites for radiation detection. *Advanced Materials* **2006,** *18* (1), 77-79.

140. Wang, R.; Shang, Y.; Kanjanaboos, P.; Zhou, W.; Ning, Z.; Sargent, E. H., Colloidal quantum dot ligand engineering for high performance solar cells. *Energy & Environmental Science* **2016,** *9* (4), 1130-1143.

141. Lan, X.; Voznyy, O.; Kiani, A.; García de Arquer, F. P.; Abbas, A. S.; Kim, G.-H.; Liu, M.; Yang, Z.; Walters, G.; Xu, J.; Yuan, M.; Ning, Z.; Fan, F.; Kanjanaboos, P.; Kramer, I.; Zhitomirsky, D.; Lee, P.; Perelgut, A.; Hoogland, S.; Sargent, E. H., Passivation using molecular halides increases quantum dot solar Ccell performance. *Advanced Materials* **2016,** *28* (2), 299-304.

142. Carey, G. H.; Yuan, M.; Comin, R.; Voznyy, O.; Sargent, E. H., Cleavable ligands enable uniform close packing in colloidal quantum dot solids. *ACS Applied Materials & Interfaces* **2015,** *7* (39), 21995-22000.

143. Kovalenko, M. V.; Scheele, M.; Talapin, D. V., Colloidal nanocrystals with molecular metal chalcogenide surface ligands. *Science* **2009,** *324* (5933), 1417-1420.

144. Ning, Z.; Ren, Y.; Hoogland, S.; Voznyy, O.; Levina, L.; Stadler, P.; Lan, X.; Zhitomirsky, D.; Sargent, E. H., All-Inorganic colloidal quantum dot photovoltaics employing solution-phase halide passivation. *Advanced Materials* **2012,** *24* (47), 6295-6299.

145. Dabbousi, B. O.; Rodriguez-Viejo, J.; Mikulec, F. V.; Heine, J. R.; Mattoussi, H.; Ober, R.; Jensen, K. F.; Bawendi, M. G., (CdSe)ZnS core−shell quantum dots: Synthesis and characterization of a size series of highly luminescent nanocrystallites. *The Journal of Physical Chemistry B* **1997,** *101* (46), 9463-9475.

146. Peng, X.; Schlamp, M. C.; Kadavanich, A. V.; Alivisatos, A. P., Epitaxial growth of highly luminescent CdSe/CdS core/shell nanocrystals with photostability and electronic accessibility. *Journal of the American Chemical Society* **1997,** *119* (30), 7019-7029.

147. Talapin, D. V.; Mekis, I.; Götzinger, S.; Kornowski, A.; Benson, O.; Weller, H., CdSe/CdS/ZnS and CdSe/ZnSe/ZnS Core−Shell−Shell nanocrystals. *The Journal of Physical Chemistry B* **2004,** *108* (49), 18826-18831.

148. Steckel, J. S.; Zimmer, J. P.; Coe-Sullivan, S.; Stott, N. E.; Bulović, V.; Bawendi, M. G., Blue luminescence from (CdS)ZnS core–shell nanocrystals. *Angewandte Chemie International Edition* **2004,** *43* (16), 2154-2158.

149. Talapin, D. V.; Koeppe, R.; Götzinger, S.; Kornowski, A.; Lupton, J. M.; Rogach, A. L.; Benson, O.; Feldmann, J.; Weller, H., Highly emissive colloidal CdSe/CdS heterostructures of mixed dimensionality. *Nano Letters* **2003,** *3* (12), 1677-1681.

150. Flanagan, J. C.; Shim, M., Enhanced air stability, charge separation, and photocurrent in CdSe/CdTe heterojunction nanorods by thiols. *The Journal of Physical Chemistry C* **2015,** *119* (34), 20162-20168.

151. Li, Y.; Wang, H.; Xie, L.; Liang, Y.; Hong, G.; Dai, H., MoS_2 nanoparticles grown on graphene: An advanced catalyst for the hydrogen evolution reaction. *Journal of the American Chemical Society* **2011,** *133* (19), 7296-7299.

152. Gaponik, N.; Herrmann, A.-K.; Eychmüller, A., Colloidal nanocrystal-based gels and aerogels: material aspects and application perspectives. *The Journal of Physical Chemistry Letters* **2012,** *3* (1), 8-17.

153. Wang, W.; Liu, Z.; Zheng, C.; Xu, C.; Liu, Y.; Wang, G., Synthesis of CdS nanoparticles by a novel and simple one-step, solid-state reaction in the presence of a nonionic surfactant. *Materials Letters* **2003,** *57* (18), 2755-2760.

154. Hines, M. A.; Guyot-Sionnest, P., Synthesis and characterization of strongly luminescing ZnS-capped CdSe nanocrystals. *The Journal of Physical Chemistry* **1996,** *100* (2), 468-471.

155. Qu, L.; Peng, X., Control of photoluminescence properties of CdSe nanocrystals in growth. *Journal of the American Chemical Society* **2002,** *124* (9), 2049-2055.

156. Carbone, L.; Nobile, C.; De Giorgi, M.; Sala, F. D.; Morello, G.; Pompa, P.; Hytch, M.; Snoeck, E.; Fiore, A.; Franchini, I. R.; Nadasan, M.; Silvestre, A. F.; Chiodo, L.; Kudera, S.; Cingolani, R.; Krahne, R.; Manna, L., Synthesis and micrometer-scale assembly of colloidal CdSe/CdS nanorods prepared by a seeded growth approach. *Nano Letters* **2007,** *7* (10), 2942-2950.

157. Yu, W. W.; Qu, L.; Guo, W.; Peng, X., Experimental determination of the extinction coefficient of CdTe, CdSe, and CdS nanocrystals. *Chemistry of Materials* **2003,** *15* (14), 2854-2860.

158. Tomonori, I., Simple criterion for wurtzite-zinc-blende polytypism in semiconductors. *Japanese Journal of Applied Physics* **1998,** *37* (10B), L1217.

159. Yeh, C.-Y.; Lu, Z. W.; Froyen, S.; Zunger, A., Zinc-blende/wurtzite polytypism in semiconductors. *Physical Review B* **1992,** *46* (16), 10086-10097.

160. Murayama, M.; Nakayama, T., Chemical trend of band offsets at wurtzite/zinc-blende heterocrystalline semiconductor interfaces. *Physical Review B* **1994,** *49* (7), 4710-4724.

161. Manna, L.; Wang, L.; Cingolani, R.; Alivisatos, A. P., First-principles modeling of unpassivated and surfactant-passivated bulk facets of wurtzite CdSe: A model system for studying the anisotropic growth of CdSe nanocrystals. *The Journal of Physical Chemistry B* **2005,** *109* (13), 6183-6192.

162. Manna, L.; Scher, E. C.; Alivisatos, A. P., Synthesis of soluble and processable rod-, arrow-, teardrop-, and tetrapod-shaped CdSe nanocrystals. *Journal of the American Chemical Society* **2000,** *122* (51), 12700-12706.

163. Shiang, J. J.; Kadavanich, A. V.; Grubbs, R. K.; Alivisatos, A. P., Symmetry of annealed wurtzite CdSe nanocrystals: Assignment to the C3v point group. *The Journal of Physical Chemistry* **1995,** *99* (48), 17417-17422.

164. Sachleben, J. R.; Wooten, E. W.; Emsley, L.; Pines, A.; Colvin, V. L.; Alivisatos, A. P., NMR studies of the surface structure and dynamics of semiconductor nanocrystals. *Chemical Physics Letters* **1992,** *198* (5), 431-436.

165. Dance, I. G.; Choy, A.; Scudder, M. L., Syntheses, properties, and molecular and crystal structures of $(Me_4N)_4[E_4M_{10}(SPh)_{16}]$ (E = sulfur or selenium; M = zinc or cadmium): molecular supertetrahedral fragments of the cubic metal chalcogenide lattice. *Journal of the American Chemical Society* **1984,** *106* (21), 6285-6295.

166. Evans, B. J.; Doi, J. T.; Musker, W. K., Fluorine-19 NMR study of the reaction of p-fluorobenzenethiol and disulfide with periodate and other selected oxidizing agents. *The Journal of Organic Chemistry* **1990,** *55* (8), 2337-2344.

167. Keeble, D. J.; Thomsen, E. A.; Stavrinadis, A.; Samuel, I. D. W.; Smith, J. M.; Watt, A. A. R., Paramagnetic point defects and charge carriers in PbS and CdS nanocrystal polymer composites. *The Journal of Physical Chemistry C* **2009,** *113* (40), 17306-17312.

168. Taylor, A. L.; Filipovich, G.; Lindeberg, G. K., Identification of Cd vacancies in neutron-irradiated CdS by electron paramagnetic resonance. *Solid State Communications* **1971,** *9* (13), 945-947.

169. Watkins, G. D., Intrinsic defects in II–VI semiconductors. *Journal of Crystal Growth* **1996,** *159* (1), 338-344.

170. Schneider, J.; Räuber, A., Electron spin resonance of the F-centre in ZnS. *Solid State Communications* **1967,** *5* (9), 779-781.

171. Subila, K. B.; Kishore Kumar, G.; Shivaprasad, S. M.; George Thomas, K., Luminescence properties of CdSe quantum dots: Role of crystal structure and surface somposition. *The Journal of Physical Chemistry Letters* **2013,** *4* (16), 2774-2779.

172. Nanda, J.; Kuruvilla, B. A.; Sarma, D. D., Photoelectron spectroscopic study of CdS nanocrystallites. *Physical Review B* **1999,** *59* (11), 7473-7479.

173. Choi, J. J.; Bealing, C. R.; Bian, K.; Hughes, K. J.; Zhang, W.; Smilgies, D.-M.; Hennig, R. G.; Engstrom, J. R.; Hanrath, T., Controlling nanocrystal superlattice symmetry and shape-anisotropic interactions through variable ligand surface coverage. *Journal of the American Chemical Society* **2011,** *133* (9), 3131-3138.

174. Lee, S. M.; Cho, S. N.; Cheon, J., Anisotropic shape control of colloidal inorganic nanocrystals. *Advanced Materials* **2003,** *15* (5), 441-444.

175. Glotzer, S. C.; Solomon, M. J., Anisotropy of building blocks and their assembly into complex structures. *Nature Materials* **2007,** *6* (7), 557-562.

176. Kazes, M.; Lewis, D. Y.; Ebenstein, Y.; Mokari, T.; Banin, U., Lasing from semiconductor quantum rods in a cylindrical microcavity. *Advanced Materials* **2002,** *14*, 317-321.

177. Michalet, X.; Pinaud, F. F.; Bentolila, L. A.; Tsay, J. M.; Doose, S.; Li, J. J.; Sundaresan, G.; Wu, A. M.; Gambhir, S. S.; Weiss, S., Quantum dots for live cells, in vivo imaging, and diagnostics. *Science (New York, N.Y.)* **2005,** *307* (5709), 538-544.

178. Bae, W. K.; Char, K.; Hur, H.; Lee, S., Single-step synthesis of quantum dots with chemical composition gradients. *Chemistry of Materials* **2008,** *20* (2), 531-539.

179. Cao; Banin, U., Growth and properties of semiconductor core/shell nanocrystals with InAs cores. *Journal of the American Chemical Society* **2000,** *122* (40), 9692-9702.

180. Kim, S.; Fisher, B.; Eisler, H.-J.; Bawendi, M., Type-II quantum dots: CdTe/CdSe(Core/Shell) and CdSe/ZnTe(Core/Shell) heterostructures. *Journal of the American Chemical Society* **2003,** *125* (38), 11466-11467.

181. C. P. Collier; T. Vossmeyer, A.; Heath, J. R., Nanocrystal superlattices. *Annual Review of Physical Chemistry* **1998,** *49* (1), 371-404.

182. Korala, L.; Li, L.; Brock, S. L., Transparent conducting films of CdSe(ZnS) core(shell) quantum dot xerogels. *Chemical Communications* **2012,** *48* (68), 8523-8525.

183. Joo, J.; Na, H. B.; Yu, T.; Yu, J. H.; Kim, Y. W.; Wu, F.; Zhang, J. Z.; Hyeon, T., Generalized and facile synthesis of semiconducting metal sulfide nanocrystals. *Journal of the American Chemical Society* **2003,** *125* (36), 11100-11105.

184. Peng, Z. A.; Peng, X., Formation of high-quality CdTe CdSe and CdS nanocrystals using CdO as precursor. *Journal of the American Chemical Society* **2000,** *123* (1), 183-184.

185. Vanmaekelbergh, D.; Liljeroth, P., Electron-conducting quantum dot solids: novel materials based on colloidal semiconductor nanocrystals. *Chemical Society Reviews* **2005,** *34* (4), 299-312.

186. McDonald, S. A., Cyr, P. W., Levina, L. & Sargent, E. H. Photoconductivity from PbS-nanocrystal/semiconducting polymer composites for solution-processible, quantum-size tunable infrared photodetectors. *Applied Physics Letters* **2004**, 85, 2089–2091.

ABSTRACT

CHALCOGENIDE NANOCRYSTAL ASSEMBLY: CONTROLLING HETEROGENEITY AND MODULATING HETEROINTERFACES

by

Jessica Davis

May 2017

Advisor: Dr. Stephanie L. Brock

Major: Chemistry (Inorganic)

Degree: Doctor of Philosophy

This dissertation work is focused on developing methods to facilitate charge transport in heterostructured materials that comprise nanoscale components. Multicomponent semiconductor materials were prepared by (1) spin coating of discrete nanomaterials onto porous silicon (pSi) or (2) self-assembly. Spin-coating of colloidal quantum dot (QD) PbS solutions was employed to create prototype PbS QD based radiation detection devices using porous silicon (pSi) as an n-type support and charge transport material. These devices were initially tested as a photodetector to ascertain the possibility of their use in high energy radiation detection. Short chain thiolate ligands (4-fluorothiophenolate) and anion passivation at the particle interface were evaluated to augment interparticle transport. However, the samples showed minimum interaction with the light source possibly due to poor infiltration of the PbS QDs into the pSi.

The second project was also driven by the potential synergistic properties that can be achieved in multicomponent metal chalcogenide nanostructures, potentially useful in optoelectronic devices. Working with well-established methods for single component metal chalcogenide (MQ) particle gels this dissertation research sought to develop practical methods for co-gelation of different component particles with complimentary functionalities. By monitoring the kinetics of aggregation using time

resolved dynamic light scattering and NMR spectroscopy the kinetics of aggregation of CdQ NCs adopting the two most common crystal structures was studied and it was determined that the hexagonal (wurtzite) crystal structure aggregated faster than the cubic (zinc blende) crystal structure. For gel coupling of nanoparticles with differing Q (Q=S, Se and Te), once we accounted for the crystal structure effects, it was determined that the relative redox characteristics of Q govern the reaction rate. This could be moderated by the sterics of the ligand.

The oxidative sol-gel assembly routes were also employed to fabricate metal chalcogenide NC gels with different NC components with control over the degree of mixing. In order to control the degree of mixing, the factors that underscore sol-gel oxidative assembly (structure, redox properties of Q and ligand sterics) were exploited. Two component gels of *zb*-Zns and *zb*-CdSe were prepared in which both were capped with 11-mercaptoundecanoic acid (MUA), leading to very different assembly rates due to the faster gelation of *zb*-CdSe and in which *zb*-ZnS was capped with MUA and *zb*-CdSe capped with the longer-chain 16-mercaptohexadecanoic acid (MHA) to slow down the rate for *zb*-CdSe. When the kinetics are similar, a uniformly mixed a gel is produced, when different, CdSe gels first giving a 2-layer macro gel.

AUTOBIOGRAPHICAL STATEMENT
Jessica Davis

Education

- 2011-2016 Ph.D. Inorganic Chemistry, Wayne State University, Detroit, MI

Dissertation: Chalcogenide Nanocrystal Assembly: Controlling Heterogeneity and Modulating Heterointerfaces
Advisor: Prof. Stephanie L. Brock

- 2002-2006 B.S. in Chemistry, University of Toledo, Toledo, OH

Research and Teaching Experience

- 2013-2016 Graduate Research Assistant, Department of Chemistry, Wayne State University, Detroit, MI
- 2011-2013 Graduate Teaching Assistant, Department of Chemistry, Wayne State University, Detroit, MI

Awards and Fellowships

- Teaching Award Department of Chemistry, Wayne State University, 2012
- Best Student Presentation Michigan Microscopy Society, 2014
- WSU Graduate School, Graduate Research Assistantship, 2015-2016